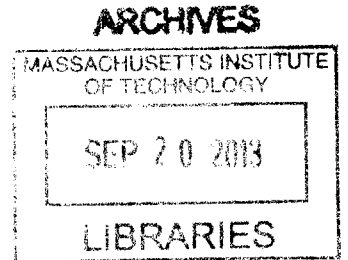


Development of Polymeric Nanoparticle Vaccines for Immunostimulation

by
Pamela A. Basto

B.S. Biomedical Engineering
The University of Texas at Austin, 2006



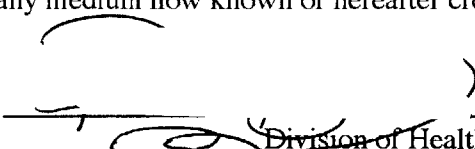
SUBMITTED TO THE DIVISION OF HEALTH SCIENCES & TECHNOLOGY IN
PARTIAL FULFILLMENT OF THE REQUIREMENTS FOR THE DEGREE OF
DOCTORATE IN PHILOSOPHY IN MEDICAL ENGINEERING MEDICAL PHYSICS
AT THE
MASSACHUSETTS INSTITUTE OF TECHNOLOGY
AUGUST 2013

©2013 Pamela A. Basto


All rights reserved.

The author hereby grants to MIT permission to reproduce
and to distribute publicly paper and electronic
copies of this thesis document in whole or in part
in any medium now known or hereafter created.

Signature of Author: _____


Division of Health Science & Technology
Institute of Medical Engineering & Science
August 28, 2013

Certified by: _____


Robert Langer, ScD
David H. Koch Institute Professor
Thesis Supervisor

Accepted by: _____

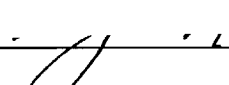

Emory Brown, MD, PhD
Director, Harvard-MIT Program in Health Sciences & Technology
Professor of Computational Neuroscience & Health Sciences & Technology

Table of Contents

List of Figures.....	5
List of Tables	10
Dedication	11
Acknowledgements	12
Abbreviations, Symbols & Definitions	14
Abstract.....	15
Chapter 1: Background.....	17
1.1 Introduction.....	17
1.1.1 Historical context of vaccines, burden of illness, and potential market	17
1.1.2 Definition of Vaccine	18
1.1.3 Current Approach for Vaccine Delivery & Limitations:	19
1.2 Fundamental Principles of the Immune Response	20
1.2.1 Innate Immune Response	21
1.2.2 Adaptive Immune Response	22
1.2.3 Cytokines are crucial mediators of immune response	24
1.2.4 Immunological differences between mice and humans	25
1.3 Toll-like receptor complexes, natural ligands, and synthetic adjuvants	27
1.3.1 Definition of Toll-like receptors	27
1.3.2 Necessity for Adjuvants in Vaccines:	27
1.3.3 Synergy of TLR for vaccine development.....	29
1.4 Polymeric Nanoparticles for Synthetic Vaccines	29
1.4.1 Potential Advantages of Polymeric Nanoparticles as a Vaccine Carrier:.....	29
Chapter 2: Development of a control releasing R848 nanoparticle vaccine platform	32
2.1 Introduction.....	32
2.2 Rationale	34
2.3 Methods	36
2.3.1 Materials:	36
2.3.2 Instrumentation:.....	36
2.3.3 Synthesis of R848-PLA Polymer Conjugate:	37

2.3.4 Synthesis of PLGA-AF647 and PLGA-AF488 Block Copolymer	38
2.3.5 Nanoparticle vaccine formation via double emulsion	38
2.3.6 Nanoparticle characterization.....	39
2.3.7 Histology	40
2.3.8 In Vitro DC stimulation and Co-culture Assays	40
2.3.9 C ¹⁴ Nanoparticle Biodistribution	41
2.3.10 <i>In vivo</i> Nanoparticle Cellular Uptake & Distribution.....	42
2.3.11 Mouse Fluorescence Imaging	42
2.3.12 In vivo antigen-specific T cell proliferation assay	42
2.3.13 Serum analysis of free R848	42
2.3.14 ELISAs	43
2.3.15 Statistical Analysis.....	43
2.4 Polymer Synthesis & Characterization	43
2.5 Vaccine Nanoparticle Synthesis & Characterization	45
2.6 Nanoparticles for Dendritic Cell Activation <i>In Vitro</i>	48
2.7 Nanoparticle vaccines stimulate DCs to activate CD8+ cells in vitro	50
2.8 Nanoparticle Vaccine Bio-distribution <i>In Vivo</i>	51
2.9 Nanoparticle Vaccine Induces Antigen-Specific Cell Proliferation <i>In Vivo</i>	52
2.10 R848-Nanoparticles Induce Humoral Response	56
2.11 Summary	57
Chapter 3. Development of a epitope specific vaccine platform applied for PCSK9 serum level reduction.....	59
3.1 Introduction.....	59
3.1.1. Background & Significance of Cardiovascular Disease in the US.....	59
3.1.2. Current clinical treatments for hypercholesterolemia	60
3.1.3. PCSK9 Regulates the LDL Receptor Recycling Pathway	61
3.1.3. Current Therapeutics to Inhibit PCSK9.....	63
3.2 Rationale	66
3.3 Methods	67
2.3.1 Materials:	67
2.3.2 Instrumentation:.....	68
2.3.4 Synthesis of PLGA-PEG-biotin Block Copolymer	68

2.3.2 Biotin-Streptavidin Nanoparticle Platform Formulation & Characterization:	
.....	68
2.3.3 Assay for determination of available active binding sites:	69
2.3.3 PCSK9 Nanoparticle Vaccination:	69
2.3.4 WT-PCSK9 & GOF-PCSK9 LDL-R Binding Assay:	70
2.3.5: Assays for mPCSK9, LDL-c/HDL-c, and anti-hPCSK9 antibodies:	70
3.3 PCSK9 Epitope Selection	70
3.4 Nanoparticle Synthesis & Characterization	72
3.5 In Vitro LDL-R knockdown with Sera from Immunized Mice	78
3.6 In Vivo mPCSK9 Reduction and α-hPCSK9 IgG Increase	80
3.7 Nanoparticle Vaccines have potential to Reduce LDL- Cholesterol <i>In Vivo</i>	82
3.5 Summary & Future Directions	85
Chapter 4. Future Directions	87
4.1 Summary	87
4.2 Next generation vaccines against infectious disease	88
4.2 Non-traditional epitopes for cancer vaccine development	89
Bibliography	93
Appendix	97
A1. PCSK9 Insert Sequences	97
A1.1 WT Sequence	97
A1.2 PCSK9 Mutated sequence	98
A2. HER-2-Targeted Nanoparticle–Affibody Bioconjugates for Cancer Therapy*	99
A2. Single-Step Assembly of Homogenous Lipid-Polymeric and Lipid-Quantum Dot Nanoparticles Enabled by Microfluidic Rapid Mixing**	107

List of Figures

Figure 1.1 Incentives for Vaccine Research: Strategic Plan 2010-2020. World Health Organization. Taken from 2002.	18
Figure 2.1 Selected TLR 7 agonists in order of immunostimulatory potency	33
Figure 2.1 Schematic of nanoparticle immune system activation.	36
Figure 2.3 (Top) Schematic of protection of R848 followed by lactide ring opening polymerization (Bottom) H¹ and C¹² NMR of polymer vs. free R848.	44
Figure 2.3 2D NMR Analysis of R848-PLA conjugate (Top) COSY (Bottom left) HMBC (Bottom right) HSQC	45
.....	46
Figure 2.4 Nanoparticle schematic demonstrates the integration of polymer conjugates. Representative nanoparticle size distribution measured by dynamic light scattering (n = 15 separate batches). Transmission electron microscopy of nanoparticles, scale bar is 200 nm. Nanoparticle stability demonstrated by size and charge in 7.4 pH H₂O measured by DLS. (n=5). Nanoparticle size stability after 3 hours in various physiological conditions (n=5).....	46
Figure 2.5 A) R848 encapsulation within nanoparticle vaccines as measured by HPLC. B) Drug release of R848 from nanoparticles formed by w/o/w as measured by HPLC (n=3). C) Protein gel of nanoparticles and 10 ug of DQ-OVA demonstrating encapsulation or surface conjugation of protein.....	47
Figure 2.6. A) Histogram of CD80+CD86+ and MHCI-SIINFEKL of 1 ug of R848 conjugated nanoparticles vs. 0.6 ng free R848 and 15 ng of OVA vs. PBS. B) % BMDC viability assessed by 7AAD at 24 hours after 2 hour incubation with nanoparticles or soluble factors. Viability is normalized against BMDCs without treatment. n=6. C) Percentage of CD86+ CD80+ Kb-SIINFEKL+ BMDCs and CD86+CD80+ BMDCs on day 3 with 2 hour incubation of nanoparticles, 0.6 ng R848, and 15 ng OVA. OVA and R848+OVA variables matched the equivalent of 1 ug of NP-R848[OVA] as highlighted by the green bar. n=9,10 of three experiments * p<0.05, *** p<0.001 (one way ANOVA with Bonferroni's post hoc test).....	49
Figure 2.7. Graphs represent mean total cell count +/- s.e.m. of quadruple culture of pooled lymph node cells from one out of 3 independent experiments. Supernatants were collected from each well of co-culture at day 3 and tested by ELISA for IFNg and TNFa concentrations. *p<0.05 by ANOVA with Tukey's post hoc test. Data shown is n=8 of combined three independent experiments.....	51
Figure 2.8 (Top) Injection of 0.06 uCi of nanoparticles through different routes of administration: intravenous, intraperitoneal, and subcutaneous. (Bottom) Popliteal lymph node at 1 hour after footpad injection with 100 ug of R848-NPs.	52
Figure 2.10 Functional proliferation of adoptively transferred CFSE-labelled Va2+ Vb5+ OTI and OTII cells on day 3 after injection on day 0. *p<0.05 ** p<0.01 by	

ANOVA with Tukey’s post hoc test. Data representative of 3 (OTI) and 2 (OTII) experiments..... 54

Figure 2.11 Luminex panel on 1:1 dilution of sera taken from mice injected intravenously with 300 ug of nanoparticles or 10 ng of R848 + OVA in soluble form at 2 and 24 hours *p<0.05 ** p<0.01 * p<0.001 by ANOVA with Tukey’s post hoc test. Data shown is pooled data of n=8 of three experiments..... 55**

Figure 2.13 Anti-OVA IgG concentration at day 21, day 35, and day 42 after 100 ug day 0 subcutaneous vaccination. **p<0.05 by ANOVA with Tukey’s post hoc test. Data shown is n=6,7 of two independent experiments..... 56

Figure 2.14 Anti-nicotine antibody concentrations of C57BL/6 mice injected with vaccine formulations at week 0, 2, 4, 8. n=4,5 of 1 experiment. Data by Matteo Iannacone, Frank Alexis, and Elena Tonti [34] 57

Figure 3.1 Schematic of PCSK9/LDL-R synthesis and degradation pathway 63

Figure 3.2 Three-dimensional ribbon diagrams illustrate the location of the predicted epitopes of all four candidates as recommended by Professor Timothy Springer. 72

Figure 3.3 A) Schematic of biotin-streptavidin-biotin-epitope nanoparticle formulation. B) Nanoparticle stability of OVA₃₂₃₋₃₃₉-biotin- NPs in physiological conditions. n=3 C) Size and charge of nanoparticle formulation using streptavidin and candidate epitopes in water, n=12 D) TEM of nanoparticle formulation of OVA₃₂₃₋₃₃₉-biotin- NPs, bar is 100 nm. 74

Figure 3.4 Assessment of available biotin binding sites on PLGA-PEG-biotin-streptavidin nanoparticles with fluorescein-biotin A) Free biotin was incubated with 100 ug of nanoparticles prior to fluorescein-biotin to find the lowest concentration for available binding site saturation, n=4 B) Amount of fluorescein-biotin binding after incubation with associated peptide candidates n=6..... 77

Figure 3.5 Vaccination timeline of CFSE labeled OTII cells after adoptive transfer on Day -1 and immunization with nanoparticles on Day 0; followed by histograms of CFSE labeled OTII cells on Day 3 with varying vaccination protocols..... 78

Figure 3.6 A) Histograms depicting LDL-R levels on the surface of non-transfected, WT-PCSK9, and GOF-PCSK9 HepG2 cell lines B) Day 38 sera on transfected HepG2 cell lines n=5, 2 experimental repeats. Data by Junghwan Sung 80

Figure 3.7 ELISA results for mouse PCSK9 levels and anti-hPCSK9 IgG levels in the serum at day 10 and day 38 after immunization on day 0 and day 28. A) Levels of mouse PCKS9 assessed by ELISA in 1:200 serum dilution at day 10 and day 38. ** p<0.01 by ANOVA with Tukey post test. B) Anti-human PCSK9 IgG levels demonstrate mice immunized with nanoparticle vaccines with candidate epitopes have increased levels of human PCSK9 specific antibodies. Data representative of two experimental cohorts. 82

Figure 3.8 Serum LDL/VLDL and HDL levels in vaccinated mice at day 10, 38, and 212. Day 10 and day 38 are representative of two cohorts, day 212 represents one cohort. n=4,5 84

Figure 4.1 A) Schematic of nanoparticle vaccine for Chlamydia trachomatis B) Chlamydia loads via qPCR of the uterus on day 6 after challenge after transcervical immunization 4 weeks prior. Data by Georg Stary and Aleksandar Radovic-Moreno. Reproduced from [58, 59] 89

Figure A1.1. Schematic diagram of the formation of drug encapsulated PLA-PEG-Mal nanoparticle-Affibody bioconjugates. Nanoparticle's size diameter (< 100 nm) and distribution was visualized by electron microscopy. The hydrophilic polyethyleneglycol (PEG) chains on the surface reduce the protein absorption on the hydrophobic polymeric surface to form “stealth” nanoparticles. Direct visualization of Affibody conjugation on the surface of the nanoparticle was carried out using fluorescent image of fluorescent Affibody (Alexa Fluor 532; red) conjugated to nanoparticles. After washing the nanoparticle-Affibody bioconjugates, the fluorescent signal increases with an increased amount of fluorescent Affibody (0-20 % Affibody/polymer molar ratio) on the nanoparticle surface confirming the chemical conjugation efficiency. B) 1H-NMR (proton nuclear magnetic resonance) spectrum represents the PLA-PEG-Affibody bioconjugates. The 1H-NMR spectrum shows the protons assigned to the polymer ($\delta = 1-6$ ppm) and the presence of Affibody polypeptide ($\delta = 7-8$ ppm) confirming the chemical conjugation of the Affibody on the polymeric nanoparticles..... 102

Figure A1.2 Fluorescent microscopy of nanoparticle-Affibody bioconjugates incubated with HER-2 positive cell lines. Capan-1 cells, SK-BR-3 cells and SK-OV-3 cells were grown on chamber slides and incubated in OptiMEM medium supplemented with 5 μ g of NBD fluorescent dye encapsulated into nanoparticles shown in green with (upper panel) or targeted nanoparticle-Affibody bioconjugates (lower panel) for 2 hours prior imaging using fluorescent microscopy at 60X magnification. The cell nuclei and the actin cytoskeleton are stained with blue (4',6-diamidino-2-phenylindole) and red (Alexa-Flour Phalloidin-488), respectively. The deconvoluted fluorescent images represent the mid-cross section of the cells after washing (3 times), permeabilizing and staining steps..... 103

Figure A1.3 Combined fluorescent images (60X magnification) of a single SK-BR-3 cell to reconstruct a three-dimensional image of the cell. A1-A4 (upper panel) images represent the mid-cross section images of the same SK-BR-3 cell being rotated at 30-degree intervals along the y- axis. A4 represents an image of SK-BR-3 rotated to 90-degree along the y-axis demonstrating particles shown in green (NBD fluorescent dye encapsulated into the nanoparticles) internalized inside the cell. The cell nuclei and the actin cytoskeleton are stained with blue (4',6-diamidino-2-phenylindole) and red (Alexa-Flour Phalloidin-488), respectively. B1-B4 (lower panel) represents fluorescent images of the same SK-BR-3 (shown in the upper panel) cell without the actin cytoskeleton staining confirming the internalization of the nanoparticle-Affibody bioconjugates inside the cell..... 103

Figure A1.4. Cell viability assay (MTS assay) to evaluate the differential toxicity of targeted (Np-Affb) and untargeted nanoparticles (Np) with and without encapsulated paclitaxel (Ptxl). In this assay, the nanoparticle formulations were incubated for 2 hours, cells were subsequently washed and incubated in cell growth media to allow the effect of the drug on the cell cycles before quantifying the nanoparticle formulations toxicities against two cancer cell lines expressing HER-2 (SK-BR-3 and SK-OV-3).ANOVA test “*” p<0.01; “” p<0.05. 105**

Figure A2.1 Nanoprecipitation of lipid-polymeric NPs. (a) A representative schematic of input and output streams within hybrid lipid-polymeric nanoparticle formation in microchannels with Tesla structures (b) Illustrative figure of microfluidic synthesized NP component layers (c) TEM image of uranyl acetate stained hybrid NPs after synthesis which highlights differences in density of the core versus near the surface of the NP potentially illustrating the lipid-PEG layer. Bar is labeled at 100 nm (d) Reproducible average size distribution of hybrid NPs generated through microfluidics. Average size is 40 nm. (e) Solvent mixing in the Tesla micromixing structures using fluorescent dye and water at 5 μ L/min and 50 μ L/min, respectively, shows complete mixing at the fourth turn in the channel (scale bar: 100 μ m). 111

Figure A2.2. Characterization of Lipid-PLGA structure (a) Comparison of average NP size from the product stream with aqueous : organic flow ratios of 10:1 and 5:1 respectively where the input organic stream is either PLGA, PLGA and lipid, or lipid alone. (b) Determination of lipid coverage of polymeric NPs. Zeta potential and size of NPs as the ratio of lipid to PLGA (w/w) is decreased. (c) Size distributions in water and PBS of NPs as the ratio of lipid to PLGA is changed. Complete lipid coverage of polymeric cores is observed at a ratio of lipid to PLGA ratio of 1:10. Above this ratio, the remaining lipid forms other nanostructures such as liposomes and below this ratio, NPs are not stable in PBS due to inadequate lipid coverage. 112

Figure A2.3 Control of NP’s physicochemical properties. (a) Control of surface charge and lipid coverage of the hybrid NPs is elucidated by changes in zeta potential of the NPs in PBS using DSPE-PEG with modified functional groups of carboxyl, methyl, and amine (b) Control of NP size by varying PLGA viscosity and concentration in the organic stream. Flow ratios of aqueous to organic streams and rate were kept constant at 10 : 1 at a total flow rate of 55 μ L/min. 113

Figure A2.4. Slow versus rapid mixing. Comparison of NP size distribution in water and PBS for rapid and slow mixing of lipid and PLGA solutions with lipid : PLGA ratios of 1:1 and 1:10. Under slow mixing conditions without the input of any form of energy, aggregation upon addition of PBS indicates the presence of heterogeneous NPs (*i.e.* polymeric, lipid, and lipid-polymeric). Under rapid mixing conditions, absence of aggregation upon addition of PBS indicates that only homogenous hybrid lipid-polymeric NPs are formed, except for the 1:1 ratio that results in homogeneous hybrid NPs and liposomes. 114

Figure A2.5 NP formation to elucidate stepwise formation of hybrid lipid-polymer NPs within microchannel (a) NP size distribution in water and PBS of particles formed in two-stage manner. PLGA NPs were prepared in the microfluidic mixer,

then washed and placed as an input along with lipid aqueous stream resulting in the generation of hybrid lipid-PLGA NPs. (b) NP size distribution in water and PBS formed through the current one-step microfluidic method. 116

Figure A2.6. Preparation of hybrid lipid-QD NPs. (a) Schematic of liposome formation in the Tesla mixer with quantum dots encapsulated within the core (b) NP distribution of quantum dot encapsulated liposomes formed through the Tesla mixer (c) TEM image of hybrid lipid-QD NPs stained with 1% phosphotungstic acid aqueous solution showing monodisperse particles with a Z-average size of 60nm. Bar is labeled at 100 nm. 118

List of Tables

Table 1. Cytokines and their function.....	24
Table 2. Comparison of Mouse and Human Immunology. Adapted from [8]	25
Table 3. Characterization of Nanoparticle Properties	48
Table 4. Stages of Development of PCSK9 Therapeutics (Adapted from Do et al. [52]).....	65
Table 5. PCSK9 epitope candidates for nanoparticle B antigen	71
Table 6. Comparison of available Thermo Scientific Biotin-Binding Proteins.....	75
Table 7. Clinically available or ongoing clinical trials of cancer vaccine candidates	90

Dedication

To my family for their love and support.

Acknowledgements

Completion of my thesis has been a key accomplishment in my life and I am in deep gratitude of several:

Thesis Committee Members: I thank my committee to provide mentorship and for inspiring me to work harder in order to help people in need throughout the rest of my career. My advisor, Professor Langer, whose wisdom, perseverance, support, and outlook on life, I will always carry with me. Bob, thank you for always managing to say the right thing at the right time. Professor Farokhzad has provided years of support and the generation of a supportive learning environment, I feel privileged to have been able to watch you successfully maneuver the clinical translation of your work. I am in gratitude for Professor von Andrian to open his lab in order to gain perspective of a tiny fraction of the immensely large field of immunology. Professor Bhatia has always supported me through HST and serves as a role model on multiple levels. I have had the unique experience of knowing most of my committee's lab members on a personal level and I am fortunate to have had them influence my personal and professional life in addition to science.

In addition to my committee mentors, I wish to specifically note remarkable educators throughout my lifetime that I am honoured with the opportunity to have met: Professor Wolfgang Frey, Professor Rebecca Richards-Kortum, Dr. Michele Follen, Dr. Valerie Pronio-Stelluto, Professor Jeff Drazen, Professor Judah Folkman, Professor Norman Letvin, David Journey, Ed Davis, Dr. Joel Morrisett, Professor Al Grodzinsky, Professor Rohit Karnik, and Anjali Sastry.

My friends in lab: the nicest window (Ana Jaklenec, Chris Alabi, Abigail Lytton-Jean, Arturo Vegas, Leon Bellan, Janet Zoldan). And notably the women behind the man: Connie Beal, Ilda Thompson, Bethany Day, Tiffany Greeves, and Tuli Saha. Dr. Frank Alexis and Dr. Aleks Radovic-Moreno have provided their support, expertise, and friendship through the years, I have been fortunate to collaborate with friends in the lab. I am indebted to collaborators who I have been able to work with: Dr. Matteo Iannacone, Dr. Ashley Moseman, and Dr. Elena Tonti for the R848-PLA work, Dr. Junghwan Sung, who was my mentor on the PCSK9 project and Dr. Georg Stary, who headed the chlamydia vaccine project. Notably, Rohit Karnik, Archana Swami and Armon Sharei, whom I've been fortunate to work with on other projects outside of this thesis work. All of the members in von Andrian lab have, in some way or another, provided advice and have been a great resource, notably Scott Loughhead, David Alvarez, Michael Flynn, and Carolina Perdomo. MTL, Koch Core, Glenn Paradis, Stuart Levine, Eliza Vasile, Scott Malstrom, all members of these MIT facilities have provided remarkable support and expertise.

This work could not have been completed without a cohort of talented undergraduates that I've had the fortune of mentoring through my time here: Zoe Moyer, Jennifer Chu, Claudia Tenen, Nebiyat Tsegaye, Emma Broderick, and Camille Sullivan, all who I look forward to watching their careers unfold.

HST gave me the invitation to an amazing education and the opportunity to be immersed in the academic/medical epicenter of Boston and has directed my commitment to returning this education, knowledge, and responsibility in hopes of benefitting the

health of others. My friends here at MIT and back home have served as a priceless support system through the inevitable highs and lows of the PhD process. Your friendships have deeply enriched this chapter of my life. I cannot possibly list all the friendships that I have gained through my time here, but you all know who you are. My friends from Texas, thank you for helping me remember my beginnings and that the things I do, those invisible to the CV, matters. Officer Sean Collier, I, and the MIT community, owe sincere gratitude to your service and efforts for your years here at MIT. I would also like to thank friendship and remember Ms. Salee Aparece. Thank you x 10^6 .

Lastly, but most importantly, my family has been my greatest support throughout my life and I wouldn't have been able to be here without them. Both of my parents, coming from humble beginnings, opened many doors without being traditionally demanding and impressively without knowing how. My sister has always been a motivation to be a role model and I am thrilled that our careers have surprisingly aligned. Lastly, Nathan Reticker-Flynn, has been the continuous source of scientific & emotional support, endless bouts of laughter, and has served as a role model citizen and scientist.

Financial support for this work came from the National Science Foundation Graduate Fellowship, Center for Cancer Nanotechnology Excellence, the Koch Institute, the National Institute of Health, the Prostate Cancer Foundation Grant, and the Harvard-MIT Division of Health Science & Technology. Special thank you to David Koch, who gave our lab resources and a world-renowned facility.

Abbreviations, Symbols & Definitions

APCs- Antigen Presenting Cells
BSA- Bovine serum albumin
CTL- Cytotoxic T lymphocyte
DCs- Dendritic Cells
DLS- Dynamic light scattering
FACS- Flow cytometry
HIV- human immunodeficiency virus
IFNg- Interferon gamma
LDL-c- low density lipoprotein cholesterol
LDL-R - low density lipoprotein receptor
LPS- Lipopolysaccharide
MHC I/II- Major histocompatibility complex
NP- nanoparticle
o/w- oil-in-water
OVA- ovalbumin
PCSK9- Proprotein convertase subtilisin/kexin type 9
PEG- poly(ethylene glycol)
PLA- poly(lactic acid)
PLGA- poly(lactic co-glycolic acid)
ssRNA- single stranded RNA
TEM- transmission electron microscopy
Th- T helper
TLR - Toll Like Receptor
TNFa- tumor necrosis factor alpha

Abstract

Vaccines have revolutionized medicine by increasing the life expectancy of children and substantially decreasing the morbidity of multiple infectious diseases worldwide. Over several decades, we have acquired significant gains in the understanding of the underlying mechanisms involved in developing protective immunity, yet vaccine development has progressed comparatively slowly. This thesis serves to explore two polymeric nanoparticle platforms to demonstrate the therapeutic potential of synthetic nanocarriers as vaccines with the aim of 1) providing greater spatiotemporal release of small molecule adjuvant to secondary lymphoid sites and 2) providing a tunable surface for loading B cell antigen epitopes in a specific conformation to drive epitope-specific antibody response.

In recent decades, TLR mechanisms have been elucidated and novel agonists have been developed, yet our generation still has not seen paramount progress in the clinical translation of these agonists due to risks of systemic toxicity and off target effects. In the first section, we synthesized 223±18 nm poly(lactic-co-glycolic acid)- poly(ethylene glycol)/ poly(lactic acid)-R848 (PLGA-PEG/PLA-R848) nanoparticle vaccine that is designed to deliver a combination of antigen and control release of a small molecule adjuvant R848 ($t_{1/2}$ = 42 hours) to drive a potent antigen-specific immune response. Using ovalbumin as a model protein, this vaccine is able to enhance antigen presentation and co-stimulatory molecules on dendritic cells and subsequently enhanced proliferation of antigen-specific naïve CD8+ cells *in vitro*. Upon vaccination, our delivery system is able to increase cell-mediated and humoral response in comparison to its soluble form, thereby illustrating the potential to bring novel small molecule adjuvants to the clinics.

In the second section, we developed a nanoparticle vaccine platform that allows selective orientation of peptide epitopes to enhance B cell response in an application that has therapeutic potential for treatment for cardiovascular disease (CVD). Utilizing epitopes discovered through *in silico* modeling for human PCSK9, a plasma protein that plays an important role in LDL cholesterol (LDL-c) levels in the blood, our nanoparticle allows selective orientation through biotin-streptavidin conjugation. Upon vaccination with CPG, selected synthetic epitopes conjugated to polymeric nanoparticles trended to reduce serum LDL-c and serum PCSK9 in murine models. Additionally, antibodies in the serum showed promise to increase LDL-receptor levels in HepG2 cells transfected in with WT-hPCSK9 and GOF-hPCSK9 separately suggesting that this vaccine has the potential to reduce risks of CVD.

These studies demonstrate that designing polymeric nanoparticles for applications to stimulate the immune system can help define new, cost-effective treatment options in applications for prophylaxis against infectious diseases that are unresponsive to traditional routes of vaccination or for immunotherapy against cardiovascular disease and cancer.

Thesis Supervisor:

Robert Langer, Sc.D.

Title: David H. Koch Institute Professor, Massachusetts Institute of Technology

Thesis Readers:

Omid Farokhzad, M.D.

Title: Associate Professor of Anesthesia, Brigham & Women's Hospital

Ulrich von Andrian, M.D., Ph.D.

Title: Mallinckrodt Professor of Immunopathology, Harvard Medical School

Thesis Committee Chair:

Sangeeta Bhatia, M.D., Ph.D.

Title: John J. and Dorothy Wilson Professor of Health Sciences & Technology and EECS, Massachusetts Institute of Technology

Chapter 1: Background

1.1 Introduction

1.1.1 Historical context of vaccines, burden of illness, and potential market

Vaccines have revolutionized the field of medicine and significantly decreased worldwide childhood mortality rate from their first discovery with inoculation of cowpox to small pox in 1770 to Louis Pasteur's rabies vaccine, Jonas Salk's polio vaccine in 1950s, and Maurice Hilleman's influenza vaccines. The World Health Organization estimates that vaccination, both active and passive, assists in the prevention of three million deaths in children annually and protects another quarter-million from permanent disability [1]. Even with the significant impact that vaccines have had on human health, vaccine development has been slow to there are several infectious diseases that have been proven elusive to protection by vaccines, such as malaria and HIV, as well as chronic diseases with an underlying immunological basis, i.e. cancer and autoimmune disease. Advancements in the understanding of novel biological mechanisms and development of targeted nanoparticle delivery carriers capitalizing on these findings can help introduce more efficient vaccines for prophylaxis and treatment [2].

According to the CDC, malaria had caused 216 million episodes and 655,000 deaths and direct cost of 12 billion. Approximately one third of the world's population is infected with tuberculosis. In 2011, nearly 9 million people reported infected with tuberculosis. Even though society has curbed the overall morbidity and eradicated several infectious diseases, there are still voids in available prophylaxis and compliance for patients in many developing countries, which can be addressed with utilizing relatively recently discovered immunological mechanisms to advance vaccine development.

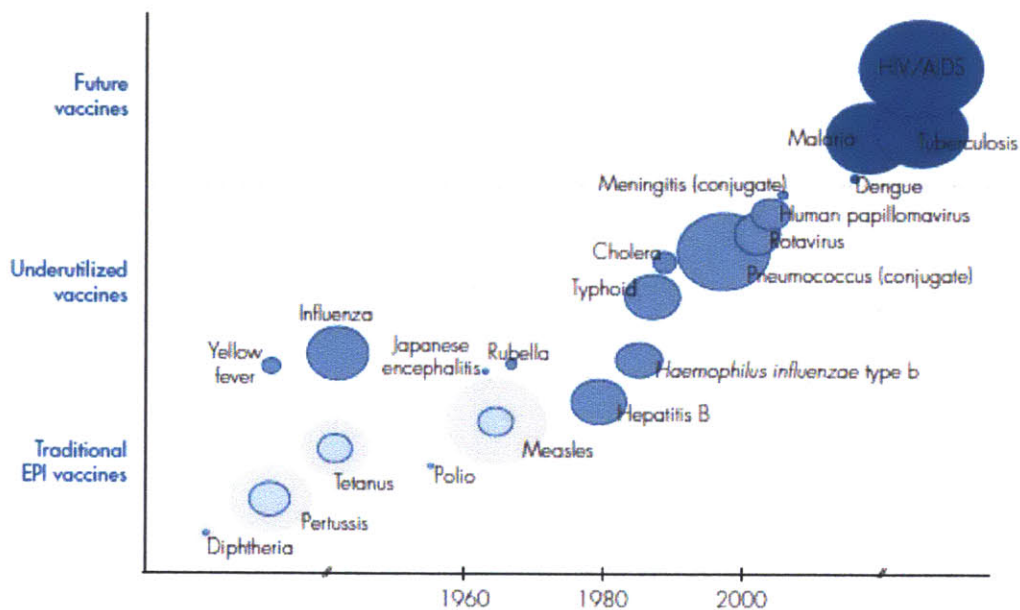


Figure 1.1 Incentives for Vaccine Research: Strategic Plan 2010-2020. World Health Organization.

1.1.2 Definition of Vaccine

A vaccine is defined as a biological preparation that can improve immunity to a particular disease. They can be prophylactic, to curb the risk of future infection by a pathogen of interest, or therapeutic, such as in the case of cancer vaccines. The term vaccine stems from the usage of cow pox in 1796 by Edward Jenner to inoculate patients in order to prevent smallpox infection, Latin *vaccina* adapted from Latin term *vaccin-us*, from *vacca* cow. With the exception of water sanitation, the utilization of vaccines in medicine has been heralded as the key turning point in medicine and has reduced mortality and increased population growth.

Vaccines typically are composed of the antigen of interest combined with an immunologic adjuvant to stimulate and increase the immune responses to the vaccine

without having a specific antigenic effect. The addition of adjuvant allows a reduction of the amount of antigen needed for memory and allows for the reduction in repeat vaccinations. The word adjuvant derives from the Latin word *adjuvare*, meaning to help or aid. An immunologic adjuvant is defined as any substance that acts to accelerate, prolong, or enhance an antigen-specific immune response when utilized with specific targeted antigens.

1.1.3 Current Approach for Vaccine Delivery & Limitations:

Some commercially available vaccines utilize purified components of pathogen lysates, such as surface carbohydrates or recombinant pathogen-derived proteins that are sometimes fused to other molecules, particularly proteins that can confer adjuvant activity. Experimental vaccines undergoing clinical trials and development include: dendritic cell (DC) vaccines, recombinant vectors, DNA vaccines, T-cell receptor peptides, and synthetic vaccines.

Another method of vaccination, largely at the clinical trial stage, is the injection of antigen-carrying cells, such as DCs or other leukocytes or modified patient-derived tumor cells [3]. Numerous clinical trials using such approaches have been published or are currently ongoing, particularly for immunotherapy against a variety of cancers due to the genetic and phenotypic heterogeneity [4]. To date, most clinical results with DC-based vaccines have shown only marginal therapeutic benefits. Moreover, DC-based vaccines are typically aimed at eliciting cell-based (cytotoxic) immunity and may be less suitable for the induction of high titers of neutralizing antibodies [5].

Vaccine approaches currently used in the clinics are separated into these types: attenuated, killed, toxoid, subunit, conjugate. Vaccines that utilize live attenuated or

inactivated pathogens typically yield a vigorous immune response, but their use has limitations. For example, live vaccine strains can sometimes cause infectious pathologies, especially when administered to immune-compromised recipients. Moreover, many pathogens, particularly viruses, undergo continuous rapid mutations in their genome, which allow them to escape immune responses to anti-genically distinct vaccine strains [6]. However, most or all pathogens are thought to possess certain antigenic determinants that are not easily mutated because they are associated with essential functions. Antibodies directed against these conserved epitopes, rather than more variable, non-essential epitopes can protect against highly mutable viruses, such as HIV-1 [7]. Killed vaccines utilize micro-organisms that have been inactivated via chemicals, heat, or radiation. Vaccines based on live or killed intact pathogens do not necessarily promote the recognition of these critical epitopes, but may essentially “distract” the immune system to focus its assault on highly variable determinants. In theory, a synthetically engineered vaccine that mimics the highly immunogenic particulate nature of viral particles, but presents selectively essential, immutable epitopes could yield more potent neutralizing antibody and effector T responses than intact micro-organisms.

There are numerous factors that may affect vaccine efficacy between patients such as: 1) disease, 2) strain, 3) vaccination schedule, 4) individual non responder, 5) ethnicity/ age/ genetics of the patient.

1.2 Fundamental Principals of the Immune Response

To understand the basics of the cells mentioned in this thesis, a brief overview of basic immunological principals serves as a foundation. Higher order organisms possess

multiple layers of defense against foreign pathogen invasion including surface barriers (physical, chemical, and biological), the innate and adaptive immune systems.

1.2.1 Innate Immune Response

Innate response is considered as the first order of defense from pathogens and is the dominant system of host defense for most organisms. This response characterized as non-specific and does not render long-lasting immunity against a particular pathogen. The response is usually triggered when microbes are recognized by pattern recognition receptors and commonly involves inflammation for leukocyte recruitment as well as the complement system activation. In regards to cellular barriers of the innate immune response, innate leukocytes include phagocytes (macrophages, neutrophils, dendritic cells), mast cells, eosinophils, basophils, and natural killer cells. Phagocytes engulf pathogens to clear invading pathogens and activate the adaptive immune response. Neutrophils are the most abundant type and migrate via chemotaxis to the site of infection. Macrophages act as scavengers for worn cells and antigen presenting cells. Dendritic cells (DC) are notably in tissues that remain in contact with the external environment such as the skin, nose, lungs, stomach, and intestines and are rightfully termed as “professional antigen-presenting” cells. Mast cells, located in connective tissues and mucous membranes, assists in regulating the inflammatory response and is commonly associated with allergy and anaphylaxis. Natural killer (NK) cells destroy host cells that have been compromised such as tumor cells and virus infecting cells by identification of cells with low levels of cell-surface marker MHCI, which can be a result of viral infections. Normal host cells typically have enough MHCI to be recognized by killer cell immunoglobulin receptors (KIR) that turns off the response of NK cells.

1.2.2 Adaptive Immune Response

The adaptive immune response evolved in higher order vertebrates to allow for a stronger immunoprotective response and immunological memory against a specific antigen in a process involving recognition of specific non-self antigens called antigen presentation. The cells of the adaptive immune system are special types of leukocytes, named lymphocytes. The major group of lymphocytes are B cells and T cells, derived from hematopoietic stem cells in the bone marrow. B cells are involved in the humoral immune response and the generation of antibodies. T cells are associated with the cell-mediated response. Both B and T cells carry receptor molecules that can recognize specific targets, T cells recognizing a “non-self” target.

B cells and T cells are the major types of lymphocytes and can recognize specific targets. T cells recognize pathogens after small fragments have been processed and presented on MHC molecules located on antigen presenting cells, the cells that process the antigen.

There are two major subtypes, CD8+ killer T cells, and CD4+ helper T cells. CD8+ cells recognize antigen peptides, typically 8 amino acids long, coupled to MHC I and CD4+ cells recognize those that are coupled to MHC II, typically peptide chains ranging from 10-12. A third subtype are $\gamma\delta$ T cells which can recognize intact antigens that are not bound on MHC receptors. CD8+ killer T cells are a subtype of T cells that targets cells infected with viruses for elimination. These cells are activated by recognition of a MHC:antigen complex combined with the co-receptor CD8. Activated CD8+ cells release cytotoxins such as perforin and granulysin both leading towards apoptosis. Helper T cells indirectly control the innate and adaptive immune response by directing other cells to kill or clear pathogens. CD4+ cells express T cell receptors that recognize antigen

bound to MHCII along with the CD4+ coreceptor. Although CD8+ cells can be activated by one MHC-peptide complex, CD4+ T cell activation is weaker and needs 200-300 receptors bound by MHC antigen. Cytokine signals from CD4+ T cell activation can enhance microbicidal function of macrophages, killing function of CD8+ cells, and upregulation of CD40L (CD154) which provides the extra-stimulatory signals required to activate antibody-producing B cells.

B cells are the cell types involved with humoral protection. They have antibodies on the surface that bind to a specific foreign antigen. This antigen/antibody complex is taken up by the B cell and processed and subsequently presented on MHCII molecules for assistance in activation by a matching helper T cell which releases lymphokines (IL-2, IL-3, IL-4, IL-5, IL-6, GM-CSF, and IFN γ) that activates the B cell to divide into plasma cells which secrete several antigen-specific antibodies. The antibodies circulate in the blood/ lymph to bind specifically to pathogens expressing the antigen and mark them for destruction by complement activation. Antibodies can neutralize these challenges through binding to bacterial toxins and/or interfere with the pathogen surface molecule used to help infect cells. Typically antibodies interact with only a small region of the antigen, for a peptide typically 5-12 amino acids.

It is known that B and T cells are initially localized in distinct anatomic regions, the superficially located B follicles and the surrounding paracortex and deep cortex. Upon challenge, antigen-specific B cells in follicles as well as CD4 T cells in the T cell area become activated and then migrate toward the border zone between the two compartments. B cells that have phagocytosed lymph-borne antigens process the acquired material and begin to present antigenic peptides in MHC class-II surface molecules that

are then recognized by the activated CD4⁺ T cells (the T_{FH} cells). Antigen-recognition allows the T_{FH} cells to provide help to B cells, which constitutes a potent survival signal and triggers the formation of germinal centers (GCs) within B follicles. The GC reaction promotes class-switch recombination, affinity maturation of antigen-specific antibodies and the formation of memory B cells and long-lived plasma cells that can produce large amounts of high-affinity antibodies for extended periods of time. Therefore, an ideal vaccine must have several key components that allow antigenic material to be efficiently recognized by both B and T cells and induce vigorous GC reactions.

1.2.3 Cytokines are crucial mediators of immune response

Cytokines are small signaling molecules released by cells and are typically immunomodulatory in nature. The table below summarizes molecules of interest used in our studies.

Table 1. Cytokines and their function

Cytokines	Function	Producing Cell	Recipient Cell	Clinical Significance
IL-2	growth, proliferation, and differentiation of cells towards effector T cells	activated T cells	CD8+, CD4+, (Treg)	combinatorial therapy for cancers and as adjuvants, HIV
IL-4	Th0-> Th2, B cell and T cell proliferation, differentiation of B cells into plasma cells; decreases the production of Th1 cells, Mp, Ifng and DC IL-12	unknown (perhaps basophil)	T cell, B cell	wound repair/ fibrosis in M2 macrophages
IL-5	activates eosinophils, stimulates B cell growth and Ig secretion	Th2 and mast cells	B cell, eosinophils	allergies, allergic rhinitis, asthma
IL-6	production of neutrophils, mediators of the acute phase response (temperature) inhibitory effects on TNFa, IL-1, IL-1ra, IL-10	T cells, macrophages, muscle, osteoblasts, SMCs, adipocytes	cells with iL-6Ra and gp130, B cells	depression, diabetes, atherosclerosis, Alzheimer's, rheumatoid arthritis, SLE, metastatic cancer

IL-10	anti-inflammatory cytokine, downregulation of Th1 cytokines, MHCII, and costimulatory molecules on Mp, increases B cell survival, proliferation, and Ig production, suppression of antigen presentation on APCs, inhibits NK cells	monocytes, lymphocytes (Th2, Tregs, subset of activated T and B cells) mast cells	stimulatory: mast cells, Th2, B cells; suppressive: Mp, Tregs, APCs, NK cells	depression, Crohn's disease
IL-12	Th1 differentiation, stimulates Ifg and TNFa from T and NK cells, block formation of new blood vessels	dendritic cell, Mp	NK cells, T cells	Autoimmune disease
IL-15	maintaining memory T cells, NK cell development, T activation and proliferation	mononuclear phagocytes	NK cells	IL-15 Suppression may improve celiac disease
IL-17a	production of many cytokines, chemokines, and prostaglandins	Th cells (induced by IL-23)	fibroblasts, endothelial cells, epithelial cells, keratinocytes, \	allergies and autoimmune disease (rheumatoid arthritis, asthma, lupus, graft rejection, psoriasis)
IFNg	activator of Mp	NK and NKT cells, Th1, and activated CD8 cells	Mp	autoimmune disease
TNFa	inflammation & acute phas reaction	Mp, CD4+, NK cells, neurons, endothelial cells, myocytes, adipocytes, fibroblasts	neutrophils, endothelial cells macrophages - phagocytosis	IBD, Alzheimer's, depression.
TGFb	proliferation, differentiation, antiproliferative for epithelial cells	cancer cells, Mp	epitelial cells,	cancer, heart disease, marfan's, loeys-dietz

1.2.4 Immunological differences between mice and humans

Although murine models have pervasive use to study immune reactions, there are some noted differences between mouse and human that play a role in clinical translation of immunotherapies. Human blood have a neutrophil:lymphocyte composition of 50-70% neutrophils: 30-50% lymphocytes versus mice blood composition of 10-25% neutrophils to 75-90% lymphocytes [8].

Table 2. Comparison of Mouse and Human Immunology. Adapted from [9]

	Mouse	Human
Neutrophils in blood	10–25%	50–70%
Lymphocytes in blood	75–90%	30–50%

TLR2 expression on PBL	Low (induced on many cells including T cells)	Constitutive (but not on T cells)
TLR3	Expressed on DC, Mac. Induced by LPS	Expressed by DC. No LPS induction
TLR9	Expressed on all myeloid cells, plasmacytoid DC and B cells	Expressed only on B cells, plasmacytoid DC and N
TLR10	Pseudogene	Widely expressed
Sialic acid Neu5GC expression	Widespread	Absent
CD4 on macrophages	Absent	Present
Predominant T cells in skin and mucosa	γ/δ TCR (dendritic epidermal T cells— DETC)	α/β TCR
γ/δ T cells respond to phospho-antigens	No	Yes
CD1 genes	CD1d	CD1a,b,c,d
FcαRI	Absent	Present
FcγRIIA, C	Absent	Present
Serum IgA	Mostly polymeric	Mostly monomeric
Ig classes	IgA, IgD, IgE, IgG1, IgG2a*, IgG2b, IgG3, IgM * absent in C57BL/6, /10, SJL and NOD mice, which have IgG2c	IgA1, IgA2, IgD, IgE, IgG1, IgG2, IgG3, IgG4, IgM
Ig CDR-H3 region	Shorter, less diverse	Longer, more diverse
IFN-α promotes Th1 differentiation	No	Yes
Th expression of IL-10	Th2	Th1 and Th2
IL-4 and IFN-γ expression by cultured Th	Either/or	Sometimes both
CD28 expression on T cells	On 100% of CD4+ and CD8+	On 80% of CD4+, 50% of CD8+
B7-H3 effects on T cells	Inhibits activation	Promotes activation
P-selectin promoter	Activated by TNF and LPS	Unresponsive to inflammation
MHC II expression on T cells	Absent	Present
MUC1 on T cells	Absent	Present
Granulysin	Absent	Present
CXCR1	Absent	Present
IL-8, NAP-2, ITAC, MCP-4, HCC-1, HCC-2, MPIF-1, PARC, eotaxin-2/3	Absent	Present
DTH lesions	Neutrophil-rich	Lymphocyte-rich
Constitutive MHC II on EC	Absent	Present
EC present Ag to CD4+ T	No	Yes
CD40 on EC	Absent	Present

1.3 Toll-like receptor complexes, natural ligands, and synthetic adjuvants

1.3.1 Definition of Toll-like receptors

Toll like receptors (TLRs) are a class of proteins that play an important role in the innate immune and digestive system. TLRs are defined as a single, membrane-spanning, non-catalytic pattern recognition receptor, usually expressed in sentinel cells such as macrophages and dendritic cells, that recognize TLR have been the important link between the innate and adaptive immune responses via dendritic cells. TLR 3 and 4, present on the surface of monocyte derived dendritic cells, utilize the MyD88 –dependent pathway to produce IL-12, IL-18 for the maturation into type 1 helper T cells and the TRIF pathway to simultaneously up-regulate co-stimulatory molecules for T cell differentiation[10].

The activation of specific pattern recognition receptors, Toll-like receptors (TLR), recognize conserved structures with very diverse pathogens such as dsRNA (TLR3), lipopolysachharide of bacterial cell walls (TLR4), and flagella (TLR5). TLR 7-9 comprises a closely related genetic sub-family whose expression is species dependent, cell type specific, is functionally compartmentalized to the endosome. TLR9 recognizes CpG in unmethylated bacterial or viral DNA and synthetic CpG oligonucleotides [11]. Recent studies utilizing Toll-like receptor ligands have shown that antigens associated with these ligands can produce exceptionally high antibody titers and rapid immune responses [12-14].

1.3.2 Necessity for Adjuvants in Vaccines:

Resting dendritic cells typically reside in many different tissue types, including lymph nodes in an immature tolerogenic state. These immature DCs present intermediate to

high-levels of peptide-MHC complexes, but without cytokines or costimulatory molecules that help differentiate T cells into effectors. T cells presented a specific antigen by immature DCs will begin to proliferate but then die by apoptosis or become unresponsive to additional activation. Comparatively when DCs acquire antigens when exposed to maturation stimuli, these cells can up-regulate MHC and costimulatory molecules and secrete cytokines. This maturation signal can be triggered via adjuvants. Vaccines used for intramuscular injections are typically administered with an adjuvant carrier, most frequently alum (aluminium potassium sulphate), that is thought to establish a depot for prolonged release of antigenic material, but also exerts immunomodulatory activities, such as skewing toward Th2 responses by mechanisms that are incompletely understood since immunization activates a complex cascade of responses [15, 16]. Recent efforts are focused on utilizing DNA and subunit/ conjugate vaccines where a weak antigen is linked to a stronger immunogens [17, 18]. Most cases, the antigen itself is only very weakly immunogenic, therefore an adjuvant is needed to create a more intense immune response [17]. Adjuvants are typically added to vaccine formulations to enhance the host memory response against a particular antigen [18]. Specific adjuvants can cater the type of immune response generated and therefore one can potentially design the immune response due to selecting the specific combination of immunomodulating materials to be delivered.

There are several companies that have partnered with large pharmaceuticals to advance their discovery in small molecule agonists against toll like receptors such as Idera with Merck utilizing TLR agonists targeted to TLR7, 8, 9. Approvals have been made in Europ for MF59, an adjuvant for flue vaccine in elderly (Fluad, Novartis), and

AS04, a combination of alum and MPL (GSK) as an adjuvant for viral vaccines such as hepatitis B and HPV.

Adjuvants that are currently in development and use are: Mineral salts - e.g., aluminium hydroxide ("alum"), aluminium phosphate, calcium phosphate; Oil emulsions – MF59, a detergent-stabilized oil-in-water emulsion; Particulate adjuvants - virosomes, ISCOMS (structured complex of saponins and lipids); Microbial derivatives - MPL^(TM) (monophosphoryl lipid A), CpG motifs, modified toxins; Plant derivatives - saponins (QS-21); Endogenous immunostimulatory adjuvants - cytokines.

1.3.3 Synergy of TLR for vaccine development

As foreign pathogens, ie bacteria and viruses, have various components that would activate TLRs simultaneously, there have been many studies on optimal TLR agonist combinations in order to drive synergistic cell mediated and humoral protection. The synergistic stimulation of TLR 2/6 with TLR 9 enabled for improved protection against influenza in mice [19]. Investigations on TLR7 (R837) combined with TLR 4 (MPL) within one PLGA particle and co-injected with PLGA encapsulated HA protein demonstrated synergistic responses in H5N1 influenza and showed significance when used synergistically compared to individual TLR.

1.4 Polymeric Nanoparticles for Synthetic Vaccines

1.4.1 Potential Advantages of Polymeric Nanoparticles as a Vaccine Carrier:

Polymeric nanoparticles have been widely explored and translated for a variety of medical applications for protein and small molecule delivery including vaccine development [5]. A synthetic nanocarrier-based vaccine delivery system provides a versatile platform for vaccine delivery not only to stimulate immune responses, but also

as a means for tolerization [20, 21]. In design considerations, polymeric nanoparticles have the advantage of being able to directly control the physicochemical properties: size, shape, surface charge, hydrophobicity, and release properties. The drug delivery carrier can accommodate more than one protein simultaneously, i.e. a mixture of purified antigenic proteins from an infectious pathogen or a heterogeneous tumor antigens lysate purified from a patient's malignancy [22] where the precise sequence and composition of these proteins is not known. Inclusion of agents that induce DC activation, such as cytokines or ligands for CD40 or TLRs serves as a means to administer potent adjuvants [23].

The use of polymeric nanoparticles for vaccine delivery has been investigated due to the same properties discovered in their design for drug delivery: biodegradability, higher surface area for adsorption, controlled and enhanced immunogenicity due to size [13, 21, 24-26]. Tetanus toxin and CpG (adjuvant for TLR 9) were co-encapsulated in PLGA nanoparticles (300 nm) which resulted in the induction of an enhanced antigen-specific T-cell proliferative response and very strong serum IgG in comparison with soluble antigen with CpG [27-30]. These studies also support the use of polymeric nanoparticles as adjuvants themselves: *in vitro* release studies showed that antigen release from antigen-adsorbed nanoparticles arrived at the lymph node site with more rapid kinetics than antigen-encapsulated nanoparticles. Additionally, higher antibody response was observed with antigen-encapsulated than free antigen and adsorbed antigen- nanoparticles [21]. Size is an important factor affecting the immunogenicity of nanoparticles, as discovered particles below 100 nm and greater than 1µm were less efficient than nanoparticles within that range [25, 26]. Modification of the surface properties of these

particles also indicated preferential targeting of immune cells as positively charged poly-L-lysine particles showed higher phagocytosis in DCs as compared with negatively charged particles [30].

The concept of using polymeric controlled-release technology for vaccine improvement started in 1979 with the encapsulation of bovine serum albumin in ethylene vinyl acetate. Gupta et al. indicated that a controlled release microparticle platform for tetanus toxoid indicated the beginning of controlled release of antigen via polymeric particle systems for vaccine development thereby offering the combination of spatial and temporal control of these systems [31-33]. The advantages of a particulate system is that one can directly package and direct antigens to APCs, co-encapsulation of multiple antigenic epitopes, and packaging both antigen and adjuvant into one carrier [34].

Chapter 2: Development of a control releasing R848 nanoparticle vaccine platform

2.1 Introduction

Development of novel effective targeted vaccines enable localization to crucial regions of the immune system and provide a prolonged boost has the potential to elicit rapid and effective protection, increase patient compliance, and reduce costs for viral and parasitic infections, such as hepatitis, HIV, malaria, cancer, etc [20]. A new method for selective and versatile targeting of antigenic material to antigen-presenting cells (APCs) in lymphoid tissues is desired to increase efficacy of the vaccine. The approach involves a targeting moiety conjugated to a carrier, such as nanoparticles, that will be loaded with one or more molecules that are recognized as antigens by B cells or T cells, or both. These adjuvants boost immune responses by activating APCs to enhance their immunostimulatory capacity, by amplifying lymphocyte responses to specific antigens and by inducing the local release of mediators, such as cytokines from a variety of cell types.

We hypothesize that engineering vaccines to emulate viruses and specifically target important immune cells in combination will provide enhanced protection against viral infection. Development of novel vaccines requires amplification of antigen specific signal through various branches of the immune system. Effective adaptive immune response requires recruitment of T cell response by activating APCs and successfully

priming B cells. In designing this system, polymeric nanoparticles are attractive vehicles for vaccine development due to key characteristics of size, controlled release and stability. Prior literature has shown that cells have a maximal nanoparticle uptake, therefore packaging an antigen and adjuvant within a single particle mimicking a viral particle will induce an immune response [35]. We have engineered and synthesized a nanoparticle delivery system that can efficiently prime B cells and produce potent T cell response through a single packaged dose with immunomodulatory components within and on the surface of the particle. We have shown that these next generation vaccines are able to induce a functional cell mediated response in vitro and in vivo, which can be utilized to drive an immune response against any antigen of interest.

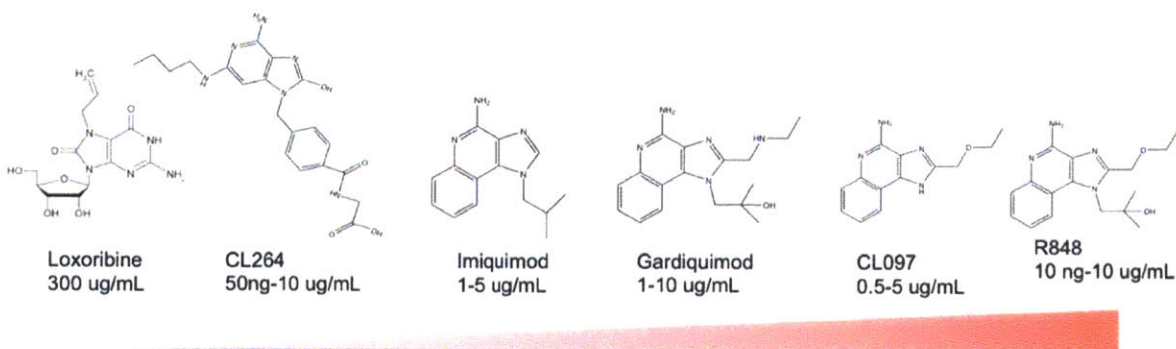


Figure 2.1 Selected TLR 7 agonists in order of immunostimulatory potency

TLR7 is predominantly expressed in lung, placenta, and spleen, while TLR8 is expressed in lung and peripheral blood leukocytes. TLR7 and TLR8 agonists have different select target cells and subsequent cytokine profiles. TLR7 agonists activate plasmacytoid DCs (pDCs) and B cells to induce IFN regulated cytokines. Contrastingly, TLR8 agonists activate myeloid DCs, monocytes, and monocyte derived DCs leading towards pro-inflammatory cytokines and chemokines: TNF- α , IL-12, MIP-1a [36]. While

mouse TLR8 is non responsive to agonists R848 and R837 (imiquimod), human TLR8 recognizes only R848 but not R837. Literature has shown that guanosine analogs activate through TLR7 and not TLR8. Natural ligands of TLR7 and 8 have been shown to be single stranded RNA (ssRNA) particularly ssRNAs with poly(U) or GU-rich sequences. Yet, certain siRNA motifs can stimulate with absence of GU content, which suggests existence of other specific sequences [37]. Microbial RNA has low nucleoside modification and has been shown to activate DCs through TLR 3, 7, 8 in comparison to mammalian RNA, which have a higher amount of modified nucleosides [38]. Due to its high potency and short half-life in circulation, R848 has not been actively clinically translated [39-41].

2.2 Rationale

In recent years, TLR mechanisms have been elucidated and novel agonists have been developed, yet our generation still has not seen paramount progress in the clinical translation of these agonists due to risks of systemic toxicity and off target effects when injected in soluble form. We hypothesize that engineering polymeric vaccines to emulate a virus particle with a payload of controlled releasing adjuvant in combination with spatially arranged surface antigen will provide enhanced protection against viral infection and has the potential to serve as an advancement in VLP design. Borrowing concepts from targeted nanoparticles for chemotherapeutic delivery [42], we have engineered nanoparticles to deliver a payload of potent R848 adjuvant in combination with antigen to secondary lymphoid organs of interest to increase immunogenicity of the antigen, increase the therapeutic window of R848, and bypass toxic systemic effects. In designing this system, polymeric PLA-PEG nanoparticles are attractive vehicles for vaccine

development due to key characteristics of size, biodegradability, biocompatibility, ability of controlled release, and stability. Conjugation of R848 to the polymer allows for high reproducibility, controlled and local release into the endosome where TLR7/8 receptors are located, as well as the potential to load higher levels of adjuvant than when attempted to encapsulate in soluble form. Additionally, combination delivery of antigen and adjuvant provides the potential of enhanced APC response[43]. As B cells are better activated via polyvalent antigens presented via a fixed surface, as in a virus-like particle, over soluble form. Thereby vaccine carriers that are able to mimic viral particles by presenting polyvalent conformationally intact antigens on their surface are predicted to stimulate a similarly strong B cell response. The T cell antigen can be derived from the same pathogen against which vaccination is intended. Additionally, the antigen may be taken from an unrelated source, such as an infectious agent to which wide-spread immunity already exists (e.g. tetanus toxoid or a common component of influenza virus, such as hemagglutinin). This method utilizes the presence of memory T cells that have arisen in response to prior infections or vaccinations. These memory cells in general react more rapidly and vigorously to antigen re-challenge and therefore may provide a source of help to B cells.

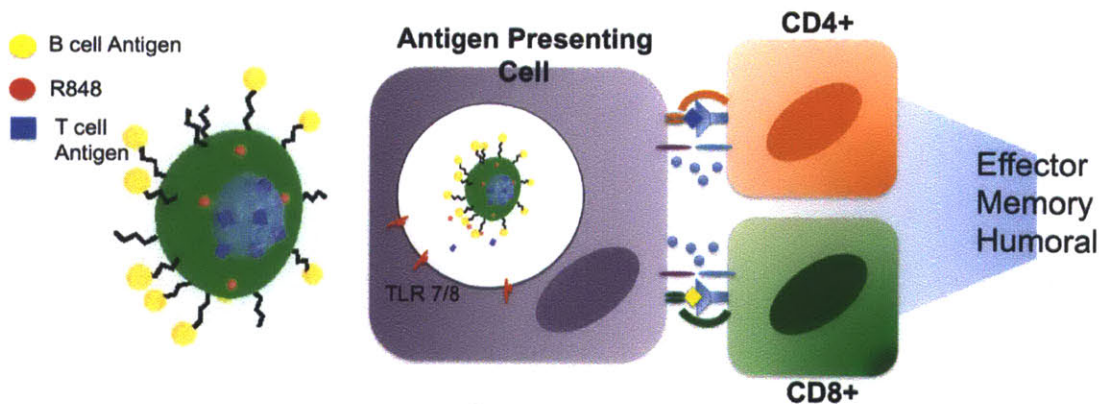


Figure 2.1 Schematic of nanoparticle immune system activation.

2.3 Methods

2.3.1 Materials:

Poly(ethylene glycol)-maleimide (Mal-PEG-NH₂-3500) was purchased from JenKem (A5006), poly(DL-lactide-co-glycolide) was purchased from Boehringer Ingelheim (i.v. 0.45), D-L lactide (Purasorb DL) purchased from Purac, C¹⁴ labeled PLGA was custom made from Moravek Biochemicals. R848, (Invivogen). Imject Alum (77161), N-hydroxysuccinimide (24500), 1-Ethyl-3-(3-dimethylaminopropyl) carbodiimide hydrochloride (77149) was purchased from Thermo Scientific/ Pierce. Benzyl chloroformate, Polyvinol Alcohol, and all organic solvents (Sigma Aldrich). DQ-Ovalbumin, Cell Trace CFSE Cell Proliferation Kit, AlexaFluor647 (Life Technologies D12053, C34554, A30679). MACs kits for mouse CD11c+, CD8a+ T cell isolation kit II, CD4+ T cell isolation kit II (Miltenyi 130-052-001, 130-095-236, 130-095-248).

2.3.2 Instrumentation:

HPLC experiment was conducted using reverse-phase C18 column (Supelco) with the mobile phase velocity of 1mL/min with the detection wavelength at 320 nm. The mobile phase consists of 0.1% TFA/water and 0.1%TFA/ACN/water (60:40). Injection volume is 100uL. ¹H & ¹²C NMR was performed on a Bruker Avance-600 spectrometer. TEM was performed using JEOL JEM200CX operated at a voltage of 200 kV. For sample prep, a droplet at 1 mg/mL was placed onto a carbon-copper TEM grid combined with 3% uranyl acetate for negative staining. Particle size (diameter, nm) and surface charge (zeta potential) measurements were made using a Malvern Nano ZS with ZetaSizer Software 6.32. Experiments were performed in DNase free water unless noted and viscosity and

refraction indices were set to those equal to water. Average electrophoretic mobilities were measured at 25°C using Malvern data analysis software and the Smoluchowsky model for aqueous solutions. Size (nm) and zeta potential (mV) is expressed as an average of 3 measurements of 10 runs +/- standard deviation. HPLC measurements utilized Agilent 1100 with Chemstation A.10.01.165. GPC measurements used Viscotek 5200 with OmniSec 4.51.554 software. Gels were run in BioradMiniProtean Gel box. Luminex assays were run using Bioplex 200 with Bioplex Manager 6.1. BD LSR II and Fortessa was used for flow cytometry and analysis was conducted via FlowJo. Tecan M1000 plate reader and SpectraMax Plus 384 were used for fluorescence/ absorbance measurements.

2.3.3 Synthesis of R848-PLA Polymer Conjugate:

R848 is reacted with benzyl chloroformate (CBZ) (2 mol eq) in a 0.75 mL EtOAc: 0.25 THF: 0.75 mL NaHCO₃ reaction for 12 hour at 4°C. The reaction was diluted with 5 mL of EtOAc and subsequently extracted with brine. The organic layer was removed and dried over MgSO₄. To a two necked round bottom flask equipped with a stir bar and condenser was added the imidazoquinoline resiquimod (R-848-CBZ, 100 mg, 3.18 X 10⁻⁴ moles), D/L lactide (5.6 gm, 3.89 X 10⁻² moles) and anhydrous sodium sulfate (4.0 gm). The flask and contents were dried under vacuum at 50°C for 8 hours. The flask was then flushed with argon and toluene (100 mL) was added. The reaction was stirred in an oil bath set at 120°C heated to reflux until all of the lactide had dissolved and then tin ethylhexanoate (75 mg, 60 μL) was added via pipette. Heating was then continued under argon for 16 hours. After cooling, water (20 mL) was added and stirring was continued for 30 minutes. The reaction was diluted with additional toluene (200 mL) and

was then washed with water (200 mL). The toluene solution was then washed in turn with 10% sodium chloride solution containing 5% concentrated hydrochloric acid (200 mL) followed by saturated sodium bicarbonate (200 mL). The solution was dried over magnesium sulfate, filtered and evaporated under vacuum to give 3.59 grams of polylactic acid-R-848 conjugate. CBZ was removed via 10% Pd/C in EtOAc under hydrogenation. TLC (silica, 10% methanol in methylene chloride) showed that the solution contained no free R-848. A portion of the polymer was hydrolyzed in base and examined by HPLC for R-848 content. By comparison to a standard curve of R-848 concentration vs HPLC response, it was determined that the polymer contained 4.51 mg of R-848 per gram of polymer. $M_n = 28189$ (THF GPC). Resulting polymer was analyzed at ^1H (600 MHz, d-Chloroform). PLA-PEG was synthesized using ring opening polymerization and characterized in the same manner. $M_n = 15260$ (THF GPC).

2.3.4 Synthesis of PLGA-AF647 and PLGA-AF488 Block Copolymer

AF647-PLGA was synthesized via EDC/NHS conjugation. 1 gram of vacuum-dried PLGA in 4 mL of chloroform mixed with 50 ug (0.250 mmol, 5 mol eq) of EDC and 28 ug of NHS (0.250 mmol, 5 mol eq) for 15 minutes. 1 gram of AF-647 dissolved in 1 mL of chloroform was added for an overnight conjugation reaction. PLGA-AF647 was precipitated in 50:50 ice cold ether:methanol solution and centrifuged at 4000 rpm for 10 minutes and subsequently dissolved in acetonitrile and washed in methanol twice. The resulting block co-polymer was characterized by GPC and NMR. AF647-PLGA block co-polymer was analogously synthesized. $M_n = 15260$ (THF GPC).

2.3.5 Nanoparticle vaccine formation via double emulsion

225 μ L of PLA-PEG-MAL solution (13.2 mg/ml in DCM) was added to 25 μ L PLA-R848 (13.2 mg/mL in DCM) and brought to a final volume of 1 mL. 500 μ L of EndoFit OVA (1 mg/mL) sonicate (15sec, 50 Amplitude), add 2 mL of 1% w/v aqueous polyvinyl alcohol solution, sonicate (15sec, 50W) and drop the solution into 40ml of water to stir for 1.5 hours. Nanoparticles were subsequently washed 3 times with water using a 100k Amicon (Millipore). EndoFit OVA functionalized with 2-iminothiolane was then subsequently conjugated for 8 hours under shaking at 4°C. Nanoparticles were washed using a 10^6 MWCO dialysis membrane (SpectraPor) for 1 hour. Encapsulated and conjugated protein levels were measured using dichloromethane solvent extraction and quantified using low BCA kit (Lambda G1003). Nanoparticles were 0.2 μ m sterile filtered prior to injection.

2.3.6 Nanoparticle characterization

Protein encapsulation and conjugation was quantified using Lambda Biotech Low Protein BCA Assay and confirmed using a Nanodrop at 280 nm absorbance. R848 release experiment was conducted in 10 mL PBS buffer at 37 °C. 3 mg NP solution with encapsulated R848 and quantified, which was immersed in the PBS solution 10ml. Each time point, 0.5 ml of solution is collected, centrifuged (8 min, 13 rpm), the supernatant is collected and the centrifuged nanoparticles for R848 quantification by HPLC. OVA encapsulation and endotoxin were assayed using low protein BCA assay and LAL assay respectively. Nanoparticle surface functionalizable maleimide groups were quantified via thiol and sulfide quantitation kit (Molecular Probes T-6060). DQ-OVA was either encapsulated within the nanoparticle or conjugated onto the surface with the methods aforementioned. 10 μ g of DQ-OVA (free and nanoparticle) were run on 4-20% TGX gels

(Biorad, 456-1094) for 45 minutes. At the end of the run, the gel was removed and imaged on the GE ImageQuant LAS 4000 utilizing the SYBR-green filter. 10 ug of nanoparticles were used in the QCL-100 LAL assay to determine endotoxin level (QCL-1000TM LAL, LONZA technologies).

2.3.7 Histology

Draining, non draining lymph nodes, and spleens were harvested and fixed in 4% PVA with an overnight sucrose gradient then sectioned in OCT at 10 um. Antibodies used in staining are as follows: Fc block (BD Pharmingen, 553141, 1:500) CD45R/B220-biotin (BD Pharmingen, 553085, 1:500), streptavidin-AF568 (Invitrogen, S-11226, 1:100), CD11c (eBiosciences, 57-0114, 1:100). LNs were isolated 10d after injection of 1µg of HA in combination with the control adjuvants. LN sections were stained for B cells (B220, green) and IgD (blue) and GL7 (Red) as markers of germinal center activity and imaged by confocal microscopy at 20x magnification. Histology on lymph nodes examining the germinal centers used the following antibodies: GL7 (BD 562080, 1:100), B220/CD45R (Biolegend, 103203, 1:100), streptavidin-AF568 (Invitrogen, S-11226, 1:100), and aCD3 (Biolegend 100203, 1:200). Germinal centers were counted in a blinded manner to obstruct bias.

2.3.8 In Vitro DC stimulation and Co-culture Assays

BMDCs were generated using a standard protocol [44] harvested from C57BL/6 mice and conditioned with RPMI 1640 media supplemented with 10% serum, Pen/strep, L-glutamine, sodium pyruvate, and 3% of GM-CSF conditioned media. BMDC were selected on day 6 and CD11c+ MACs sorted to utilize for BMDC assay. The BMDC were then resuspended to a concentration of 3×10^6 cells/ mL and subsequently 1 mL

was stimulated with a titration of nanoparticles and soluble reagents (equivalent of the dose of 1 ug of nanoparticles) incubated for 2 hours. The BMDC were then subsequently washed and resuspended with fresh media and then plated on 96 well plates (Corning, CLS3799) in triplicates. After 72 hr culture, cells were stained and assayed for FACs analysis. Antibodies used were CD80 (Biolegend 104721, 1:300), CD86 (Biolegend, 105007, 1:300), SIINFEKL-H2Kb (eBioscience 17-5743-82, 1:300), 7-AAD (Biolegend 420404) and CD11c (Biolegend, 117329, 1:300). Co-cultures used splenic cells harvested from C57BL/6 female mice (Jackson Labs) after perfusion using liberase (Roche, 05401119001) and positive selection using CD11c+ MACs. CD11c+ cells were incubated with nanoparticles and soluble factors for 2 hours, subsequently washed and plated with CD8a+ cells at 3×10^4 cells/well. Spleens and lymph nodes (inguinal, popliteal, brachial, axillary, cervical) were harvested from B6.129S6-*Rag2^{tm1Fwa}* Tg(TcraTcrb)1100Mjb (Taconic 2334-F) mice, negatively selected with CD8a+ MACs isolation kit, CFSE-labeled and plated at 3×10^5 cells/well. Co-cultures were kept at 37C at 5% CO₂ and then assayed on FACs on day 3 and day 5. Supernatants were then saved for ELISA assays on day 3 and day 5.

2.3.9 C¹⁴ Nanoparticle Biodistribution

Balb/c female mice were purchased from Jackson Laboratories at 6 weeks. 3 mg of nanoparticles were synthesized with utilizing 1 uCi (125 ug) of C¹⁴ PLGA polymer. 0.08 uCi of nanoparticles/mouse were administered via noted routes: subcutaneous, intravenous, and intraperitoneal. Mice were euthanized at time points of 2 hr and 24 hours and organs were harvested and weighed prior to digestion with Solvable (Perkin

Elmer 6NE9100) at 60C for 12 hours. Organs were mixed with Fluor and measured using Perkin Elmer TriCarb2810 TR liquid scintillation counter.

2.3.10 *In vivo* Nanoparticle Cellular Uptake & Distribution

C57BL/6 female mice were injected subcutaneously in the footpad with 100 ug of AF647-labeled nanoparticles. Popliteal lymph nodes were then harvested at 24 hours for histology (right) and flow cytometry (left). Right axillary lymph node and spleen were taken for flow cytometry.

2.3.11 Mouse Fluorescence Imaging

Female athymic hairless mice were injected via the tail vein. Excitation and emission wavelengths were used for AF647 imaging at 675nm and 720 nm respectively and subsequently analyzed via Living Image 4.2.

2.3.12 *In vivo* antigen-specific T cell proliferation assay

B6.129S7-Rag1tm1Mom Tg(TcraTcrb)1100Mjb N9+N1 (Taconic 2334-F) mice, negatively selected with CD8a+ MACs isolation kit and CFSE-labeled. 1×10^6 CD8a+ cells per mouse were adoptively transferred i.v. on day -1. 100 ug of nanoparticles were injected into both footpads at Day 0. Spleen, draining lymph nodes (inguinal and popliteal), and non-draining lymph nodes (axillary and brachial) were harvested and analyzed via flow cytometry. B6.129S7-Rag1tm1Mom Tg(TcraTcrb)425Cbn (Taconic 4234-F) were adoptively transferred after negative selection via CD4+ MACs isolation kit and CFSE-labeled in the exact same manner. Va2+ Vb5+ cell populations were subsequently gated for CFSE^{lo} Ifng^{hi} populations.

2.3.13 Serum analysis of free R848

Animals were cared for following NIH, state, and local guidelines. For the cytokine release study, 300 ug of nanoparticles were injected s.c. and its equivalent in soluble form (10 ng R848) and blood was drawn via cardiac puncture at 2 hours and 24 hours. Serum was tested via Luminex for cytokine profiles. Memory cells were examined via FACs using CD62L (Biolegend, 104435, 1:300), CD44 (Biolegend, 103006, 1:300), IgG1 (BD, 550083, 1:1), H2Kb:Ig (BD, 550750), CD8a (Biolegend,), IFNg (Biolegend).

2.3.14 ELISAs

ELISAs for determination of the supernatants from the BMDC: CD8a+ co-cultures were assayed using TNFa and IFNg were conducted using eBioscience Kits (88-7314, 88-7324). *In vivo* assessment of cytokine panels were using Millipore Luminex beads: IL-2, IFNg, IL-10, TNFa, IL-17a, IL-4, IL-5, IL-6. Mouse serum Anti-OVA IgG, IgG1, and IgE kits were purchased from Chondrex, Inc. (3011, 3013, 3010).

2.3.15 Statistical Analysis

Statistical analysis was conducted using Graphpad Prism 5. Data sets were analyzed using two-way ANOVA, followed by Bonferri test. P-values less than 0.05 were considered statistically significant. All values are reported as mean \pm s.e.m.

2.4 Polymer Synthesis & Characterization

To generate these nanoparticle vaccines, two sets of polymers were synthesized through ring opening polymerization: PLA-R848 and PLA-PEG-maleimide. As seen in Figure 2.2, the tertiary amine group was first protected prior to ring opening polymerization to ensure directed chain growth since amines and hydroxyls can both be sites of growth. PLA-PEG was synthesized using similar ring opening polymerization technique with a commercially available OH-PEG-maleimide. To verify successful

conjugation and determine if any free R848 remained in the final product, the polymer-bioconjugate was subsequently characterized by NMR and HPLC as seen in Figure 2.3 and 2.4. Free R848 was not seen in the biopolymer conjugate product in HPLC unless the polymer was hydrolyzed in base or acid. GPC detected a final molecular weight of $M_n = 28189$ Da for R848-PLA and $M_n = 15260$ for PEG-PLA.

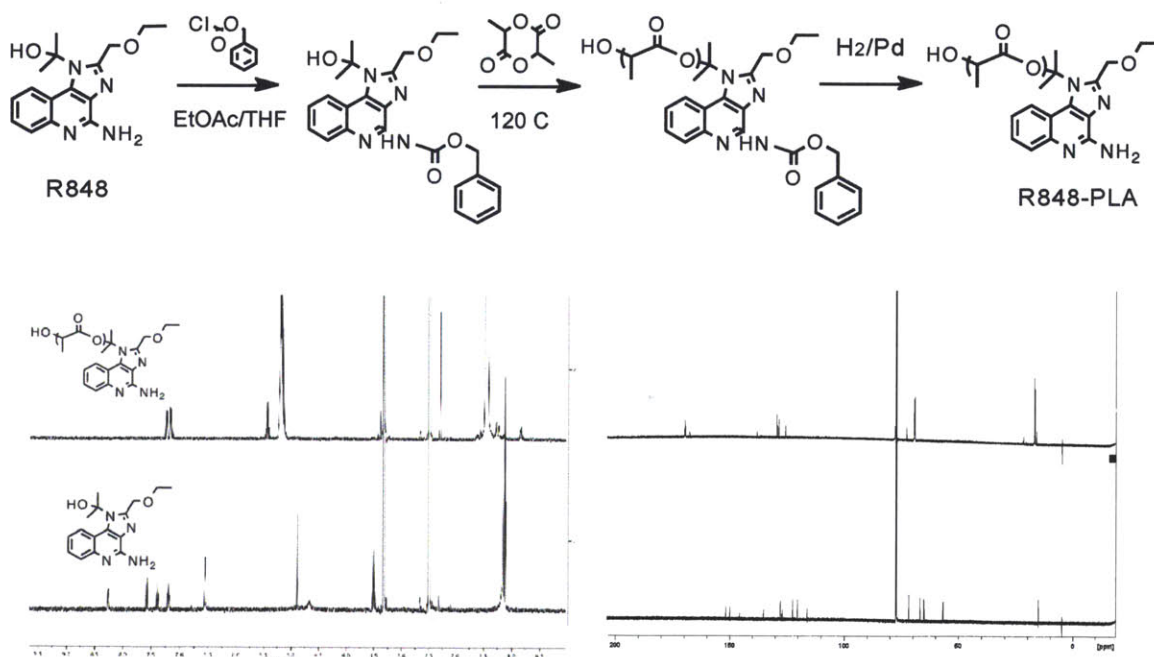
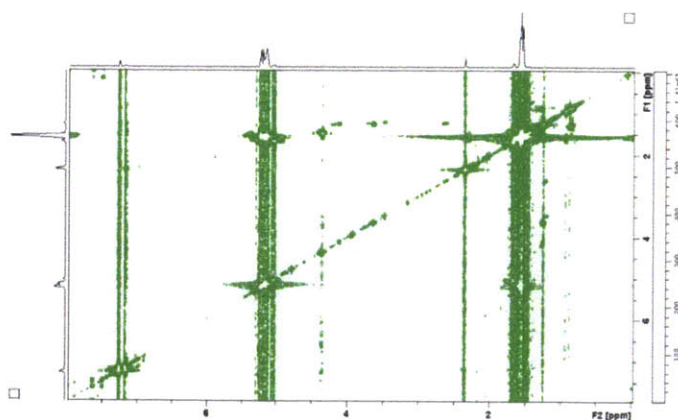


Figure 2.3 (Top) Schematic of protection of R848 followed by lactide ring opening polymerization (Bottom) ¹H and ¹³C NMR of polymer vs. free R848.



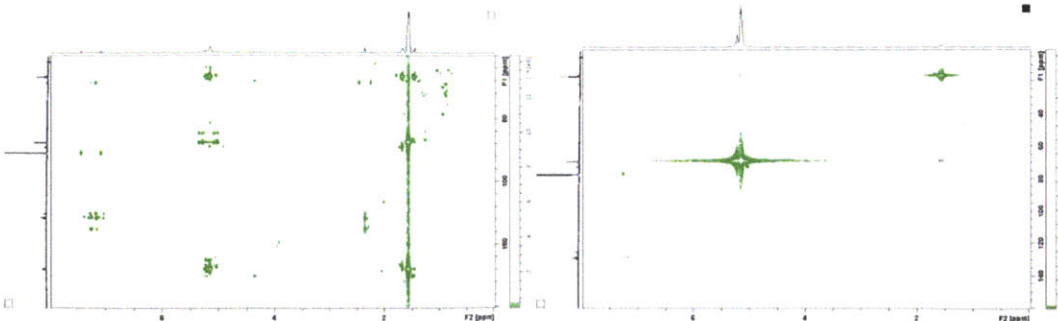


Figure 2.3 2D NMR Analysis of R848-PLA conjugate (Top) COSY (Bottom left) HMBC (Bottom right) HSQC

2.5 Vaccine Nanoparticle Synthesis & Characterization

Polymers were subsequently blended at a 1:9 of PLA-R848: PLA-PEG respectively and synthesized via w/o/w emulsion in order to encapsulate a model antigen of interest, ovalbumin (OVA), and OVA was additionally subsequently conjugated on the surface of the nanoparticle as seen in Figure 2.4. As seen in Figure 2.4, nanoparticle vaccines were synthesized and shown to be stable via dynamic light scattering at size 223 ± 18 nm in physiological conditions with the ability to retain size without aggregation after lyophilization in 10% sucrose, which is an important consideration in shelf life longevity when translating vaccines to the clinics. Nanoparticles were shown to be slightly negative in charge at -16 ± 3 mV, which may provide slight advantage in macrophage uptake and presentation, in comparison the goals of nanoparticles for the delivery of chemotherapeutic agents. Through TEM, one can see that there is a heterogenous population of nanoparticles that remain under 500 nm without aggregates. This meets the design criteria of <400 nm nanoparticles to enter secondary lymphoid organs to deliver the adjuvant and antigen payload.

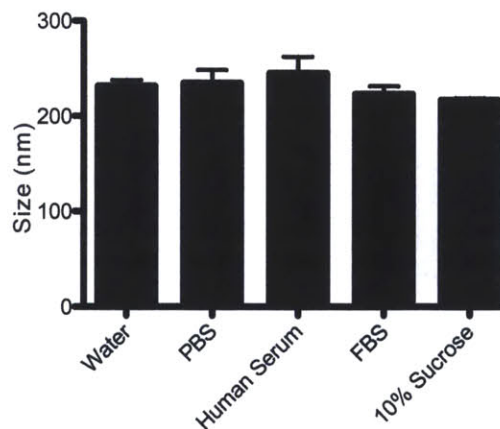
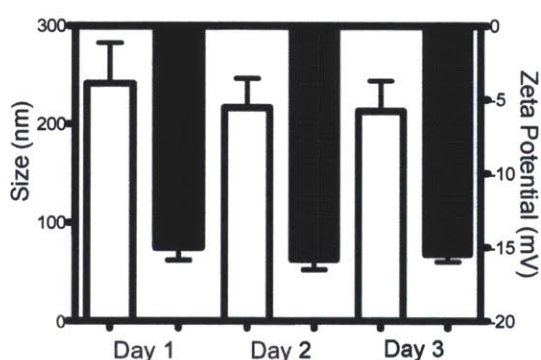
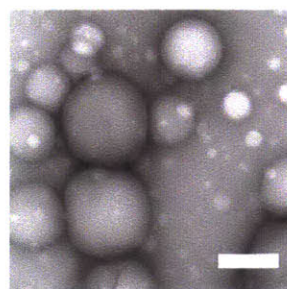
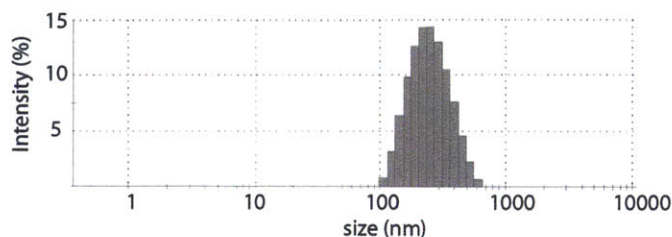
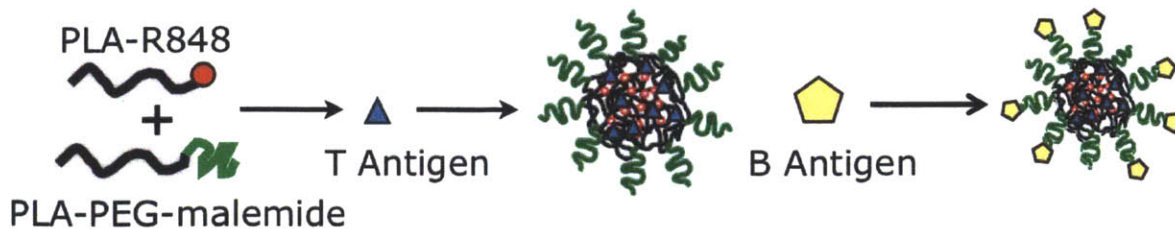


Figure 2.4 Nanoparticle schematic demonstrates the integration of polymer conjugates. Representative nanoparticle size distribution measured by dynamic light scattering (n = 15 separate batches). Transmission electron microscopy of nanoparticles, scale bar is 200 nm. Nanoparticle stability demonstrated by size and charge in 7.4 pH H₂O measured by DLS. (n=5). Nanoparticle size stability after 3 hours in various physiological conditions (n=5).

R848 was shown to be fully encapsulated within the nanoparticle and able to be released upon acid or basic degradation into soluble form (Figure 2.5 A). R848-PLA was shown to display control release kinetics, in comparison to burst release, over time with 50% of the R848 being released at approximately 42 hours, thereby giving opportunity

for the nanoparticle carrier to reach SLOs without risk of systemic release of R848. OVA was shown to be able to be encapsulated within the nanoparticle and conjugated to the surface of the nanoparticle in comparison to non-specific binding of protein to the surface. It is important to note that nanoparticle formulations were assessed for endotoxin levels and were found to have 0.4 EU/10 ug, which by pharmaceutical standards is not ideal thereby adding a confounding variable to our studies using nanoparticles without R848 as a control. LPS has been found as a common byproduct in polymer synthesis and known to be difficult to remove from polymers. All nanoparticle formulations were sterile filtered prior to in vitro and in vivo testing to ensure no further contamination.

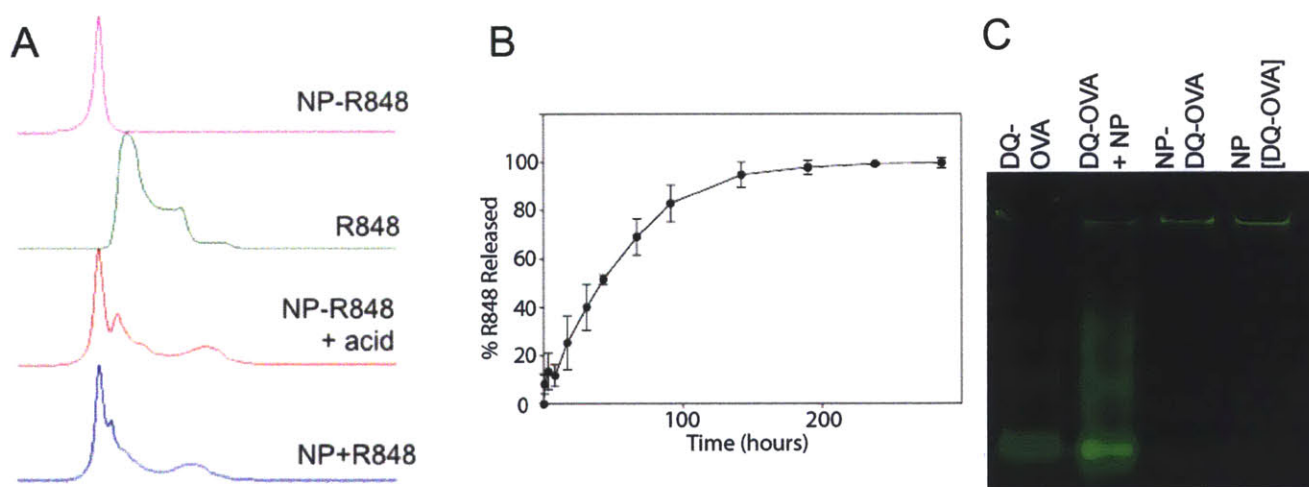


Figure 2.5 A) R848 encapsulation within nanoparticle vaccines as measured by HPLC. B) Drug release of R848 from nanoparticles formed by w/o/w as measured by HPLC (n=3). C) Protein gel of nanoparticles and 10 ug of DQ-OVA demonstrating encapsulation or surface conjugation of protein.

Table 3. Characterization of Nanoparticle Properties

Variable	Value
Internal Antigen Loading (ug/ mg polymer)	14.9 +/- 0.3
External Antigen Loading (ug/mg polymer)	4.1 +/- 0.7
R848 Loading (ng/ mg NPs)	616 +/- 35
Size (nm)	223 +/- 18
Zeta Potential (mV)	-16 +/- 3
Endotoxin Level (EU/10 ug)	<0.4

2.6 Nanoparticles for Dendritic Cell Activation *In Vitro*

R848-containing nanoparticles were then assessed for their ability to activate dendritic cells *in vitro*. CD11c+ cells were sorted from BMDC cultures and assessed for co-stimulatory markers of CD80+ and CD86+ in combination with MHCI-SIINFEKL presentation after culture with R848 delivered either in nanoparticle encapsulated or soluble form. BMDCs were chosen to demonstrate co-stimulatory function over primary CD11c+ cells harvested from splenocytes since the latter demonstrated signs of activation regardless of input. Cell viability was also investigated to determine whether nanoparticles were toxic to cells of interest. Nanoparticles were determined to be non-toxic to BMDCs as shown in Figure 2.6 B. To demonstrate the potential for activation of DCs, nanoparticles were incubated in titration. Although there was no significant difference in % CD80+ CD86+ cells, the percentage of CD80+CD86+MHCI-SIINFEKL+ cells showed increased presentation as a result of increased payload being delivered. Upon examination of the equal amount of OVA and R848 delivered to BMDCs both in soluble vs. nanoparticle form (red vs. green bars respectively), R848-nanoparticles showed significant increase in presentation of antigen ($p < 0.01$). The

increased ability to present antigen along with co-stimulatory markers further demonstrates the potential for R848-PLA nanoparticles to mount an immune response.

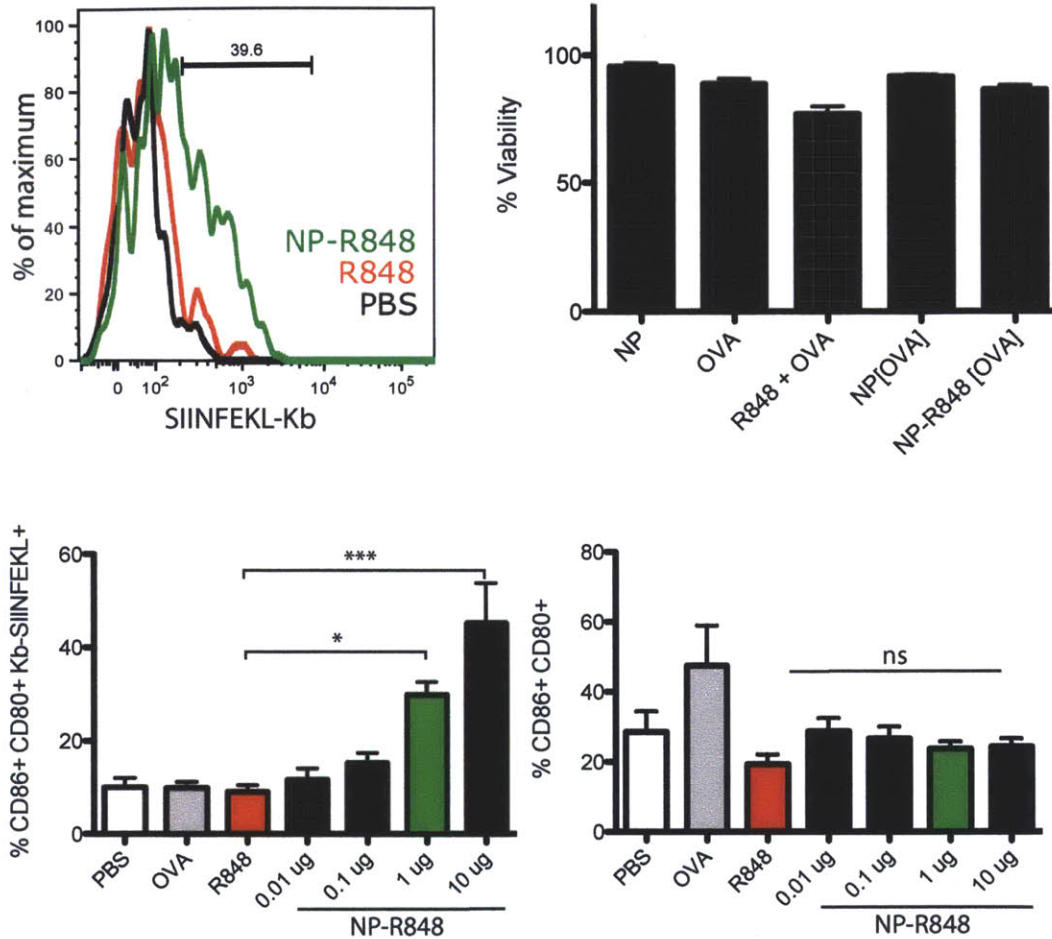
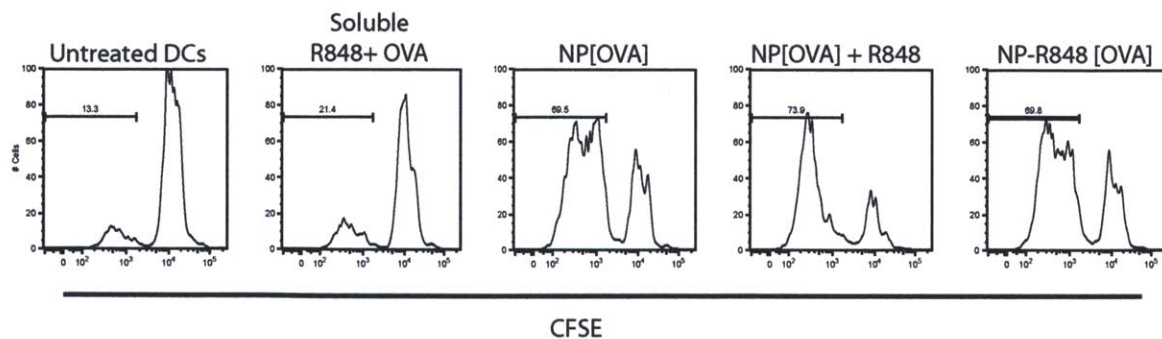


Figure 2.6. A) Histogram of CD80+CD86+ and MHCII-SIINFEKL of 1 ug of R848 conjugated nanoparticles vs. 0.6 ng free R848 and 15 ng of OVA vs. PBS. B) % BMDC viability assessed by 7AAD at 24 hours after 2 hour incubation with nanoparticles or soluble factors. Viability is normalized against BMDCs without treatment. n=6. C) Percentage of CD86+ CD80+ Kb-SIINFEKL+ BMDCs and CD86+CD80+ BMDCs on day 3 with 2 hour incubation of nanoparticles, 0.6 ng R848, and 15 ng OVA. OVA and R848+OVA variables matched the equivalent of 1 ug of NP-R848[OVA] as highlighted by the green bar. n=9,10 of three experiments * p<0.05, * p<0.001 (one way ANOVA with Bonferroni's post hoc test).**

2.7 Nanoparticle vaccines stimulate DCs to activate CD8+ cells in vitro

After demonstrating that R848-encapsulated nanoparticles can activate CD11c+ BMDCs in vitro, it was necessary to determine if activated DCs were able to mount a cell mediated response. To address this question, primary CD11c+ cells harvested from the spleen were co-cultured with CFSE-labeled negatively sorted CD8+ cells from OTI mice after the CD11c+ were incubated for 2 hours with variables and subsequently washed. On day 3, proliferation was assayed and it was shown that there was no significant difference between R848 when delivered in soluble or encapsulated within nanoparticle. Both aforementioned formulations showed increased proliferation over soluble R848 and LPS. Upon examination of the supernatant harvested from the co-cultures, both IFN γ and TNF α levels were higher for R848 delivered with or within nanoparticles than in soluble form alone. The presence of nanoparticles may help with increased endocytosis of R848 as opposed to free OVA. Interestingly, there was not a significant difference between encapsulated R848 and free R848 when delivered with nanoparticles for CD8+ proliferation.



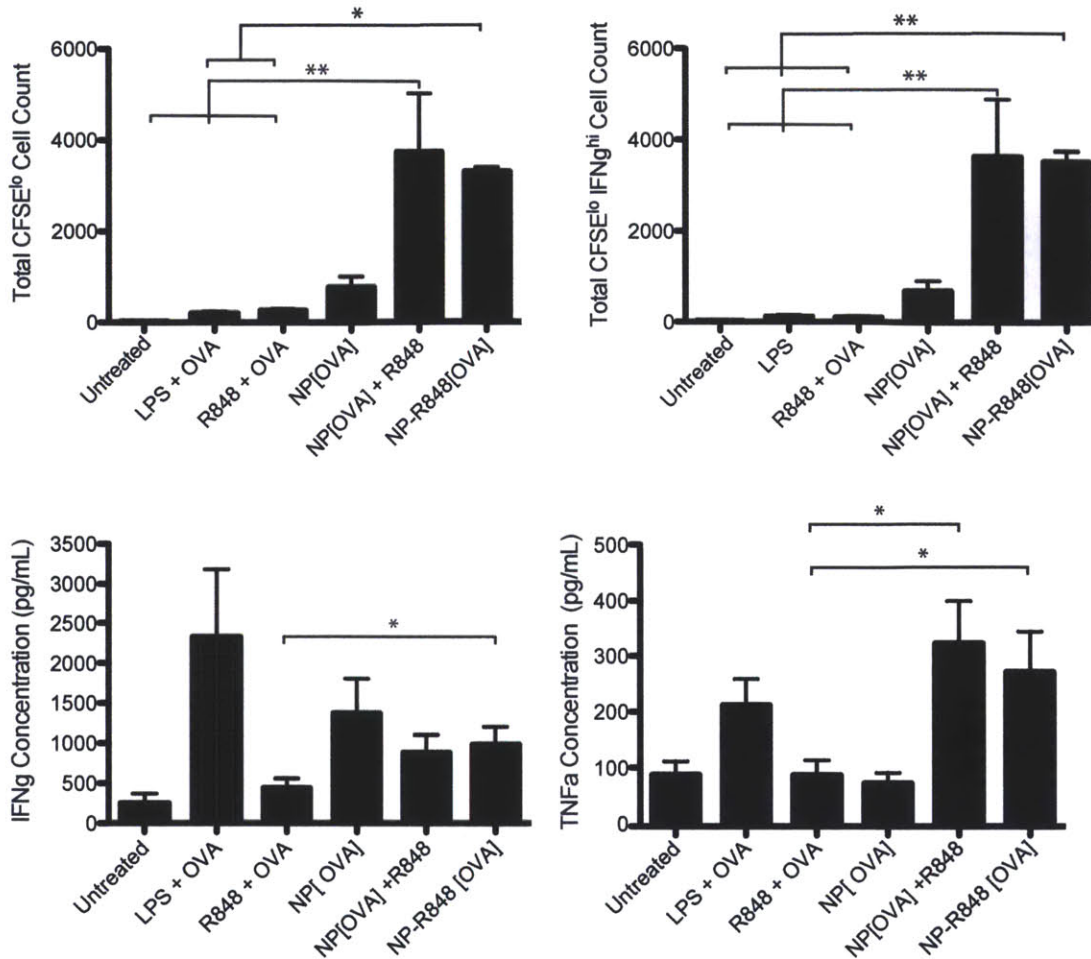


Figure 2.7. Graphs represent mean total cell count +/- s.e.m. of quadruple culture of pooled lymph node cells from one out of 3 independent experiments. Supernatants were collected from each well of co-culture at day 3 and tested by ELISA for IFN γ and TNF α concentrations. * $p < 0.05$ by ANOVA with Tukey's post hoc test. Data shown is $n=8$ of combined three independent experiments.

2.8 Nanoparticle Vaccine Bio-distribution *In Vivo*

To assess the best route of administration and to determine whether nanoparticles are able to sufficiently drain to secondary lymphoid organs, we administered C^{14} labeled nanoparticles at 2 and 24 hour time points. It was observed that nanoparticles localized to lymph nodes via subcutaneous footpad injection over other routes of administration and intraperitoneal injection accumulated in the spleen over other routes at 2 hours. Comparatively, at 24 hours there was no significant difference amongst the three routes,

but notable amounts of nanoparticles were seen in both lymph nodes and the spleen. As intramuscular injections are the typical route for conventional vaccines, subcutaneous injection was favoured. To determine if the nanoparticles localize in the lymph node, subcutaneous footpad injection with Alexa-Fluor 647 labeled R848- nanoparticles encapsulating DQ-OVA indicated substantial delivery of both antigen and the nanoparticle as seen by overlay in Figure 2.8.

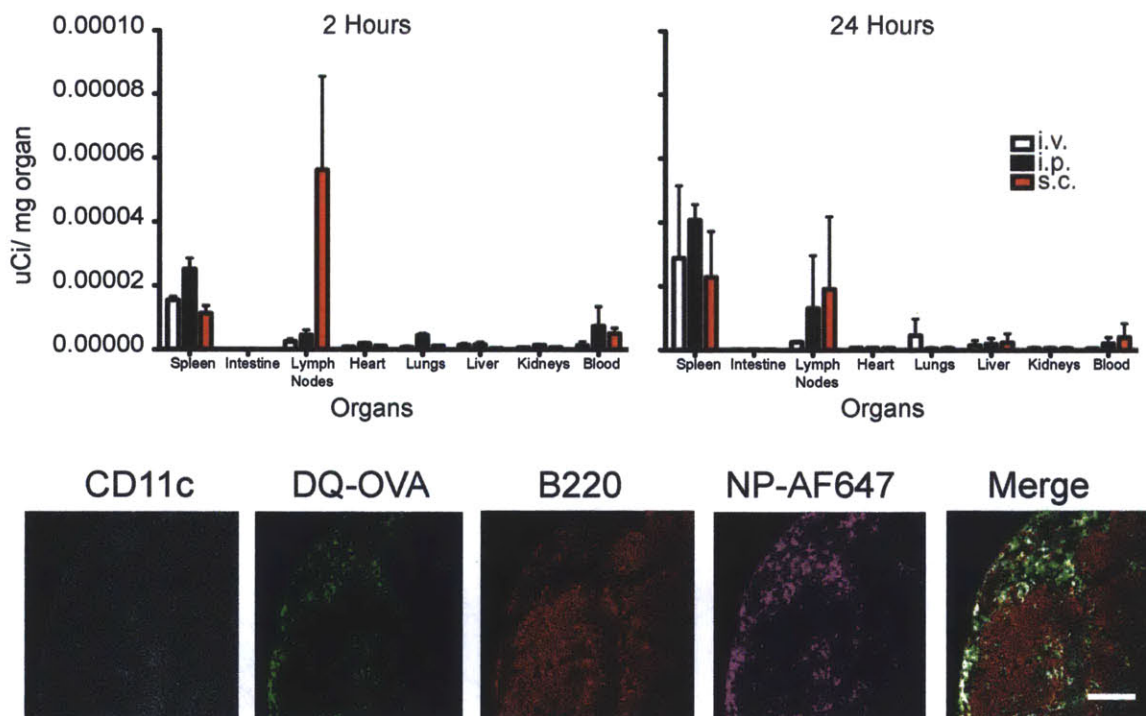


Figure 2.8 (Top) Injection of 0.06 uCi of nanoparticles through different routes of administration: intravenous, intraperitoneal, and subcutaneous. (Bottom) Popliteal lymph node at 1 hour after footpad injection with 100 ug of R848-NPs.

2.9 Nanoparticle Vaccine Induces Antigen-Specific Cell Proliferation In Vivo

Although *in vitro* studies did not differentiate nanoparticle formulations for encapsulated versus free R848, *in vivo* proliferation of CFSE-labeled OTI and OTII that were adoptively transferred into C57BL/6 mice one day prior to vaccination were

examined for functional translation. Upon examination of differences in proliferation alone, ie population of %CFSE^{lo} cells, there was no significant difference between injected cohorts (data not shown). When gated for IFN γ ^{hi}, as an indicator of functional response, within the subpopulation of CFSE^{lo} cells, there was significance for nanoparticles with encapsulated R848 over alum and soluble R848 for OTI cells. Notably, there was no significance between NP[OVA] + R848 and NP-R848[OVA] for OTI adoptive transfer. In regard to OTII cells, there was only a significant difference for alum between the other cohort groups. Soluble R848 without nanoparticles induced functional proliferation similar to nanoparticles. Though not significant, these in vivo results suggest there could be benefit to encapsulation of R848 within the nanoparticle.

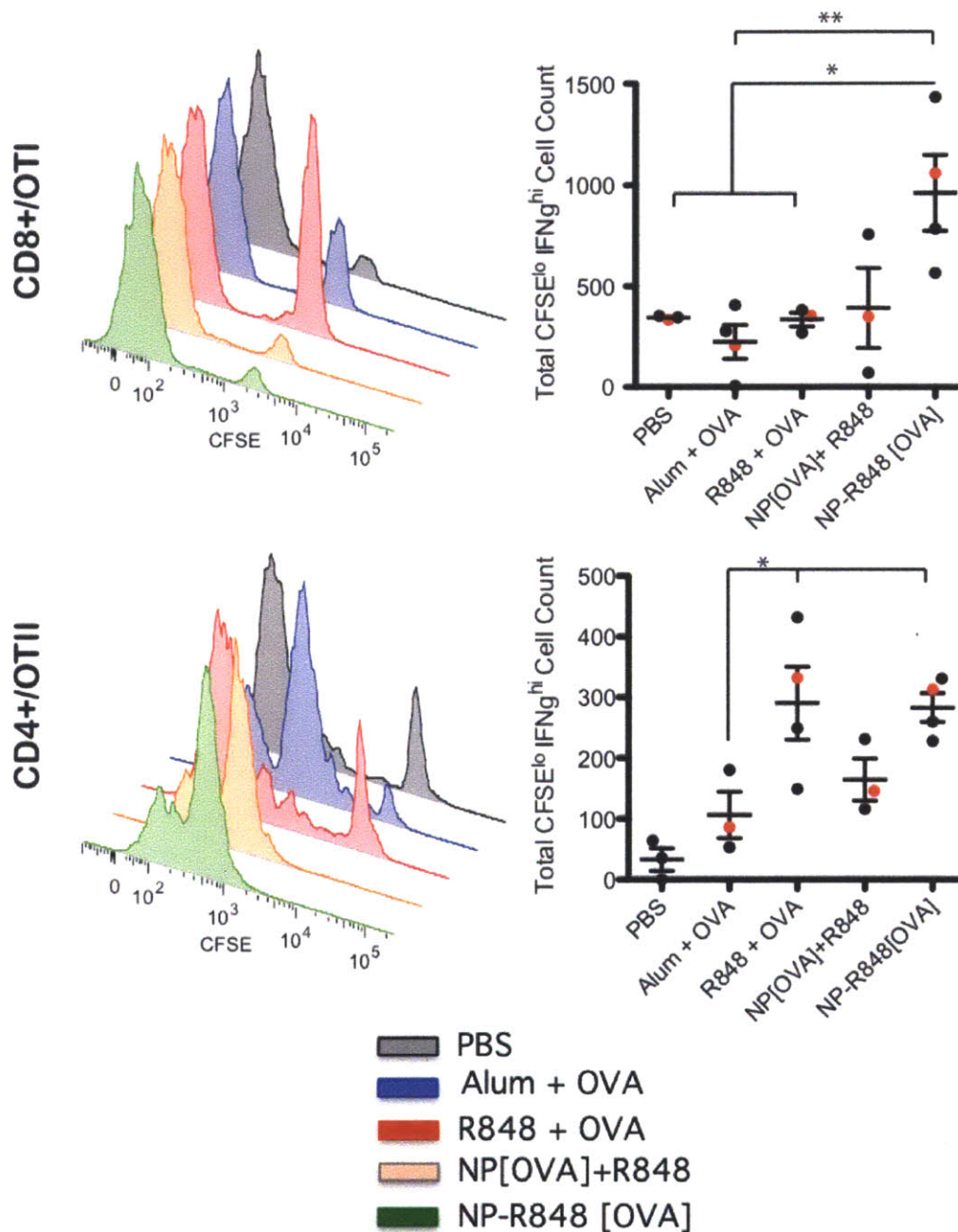


Figure 2.10 Functional proliferation of adoptively transferred CFSE-labelled Va2+ Vb5+ OTI and OTII cells on day 3 after injection on day 0. * $p < 0.05$ ** $p < 0.01$ by ANOVA with Tukey's post hoc test. Data representative of 3 (OTI) and 2 (OTII) experiments.

To assess how nanoparticles can help increase the safety profile of R848, we test the cytokine profile through a Luminex screen through injecting a higher dose of

nanoparticles in comparison to free form. Within 2 hours, there was significance in higher levels of TNF α and IL-6, while R848 encapsulated in nanoparticles increased IL-2, which may indicate T cell activation. At 24 hours, there were significant elevated levels of IFN γ , TNF α , IL-10 and IL-5 of soluble R848 over encapsulated R848. The vaccine is injected subcutaneously at a higher dose indicates that R848 encapsulated within nanoparticles may prevent systemic cytokine release, which may be indicative of the systemic side effects of soluble adjuvants. Ilinskyi et al. has reported a similar advantage in encapsulation of R848 within nanoparticles to bypass cytokine storm seen in R848 delivered in soluble form [43].

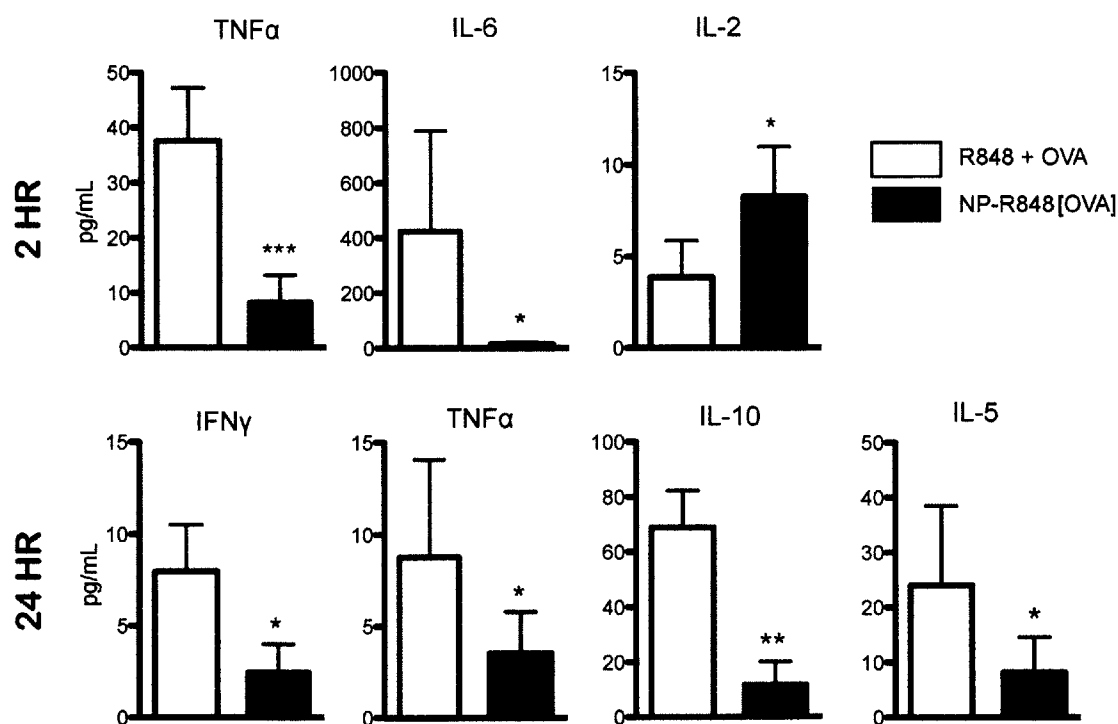


Figure 2.11 Luminex panel on 1:1 dilution of sera taken from mice injected intravenously with 300 ug of nanoparticles or 10 ng of R848 + OVA in soluble form at 2 and 24 hours *p<0.05 ** p<0.01 *** p<0.001 by ANOVA with Tukey's post hoc test. Data shown is pooled data of n=8 of three experiments.

2.10 R848-Nanoparticles Induce Humoral Response

Prophylactic vaccines are designed to generate a long lasting immune response, thereby to determine whether this nanoparticle formulation can induce an antigen-specific humoral response, sera was taken at differing time points after single bolus injection on day 0. In comparison to in vitro and in vivo results of cell-mediated response, NP-R848[OVA] had significantly higher anti-OVA IgG levels than with NP[OVA] + R848, alum + OVA , and free R848 + OVA.

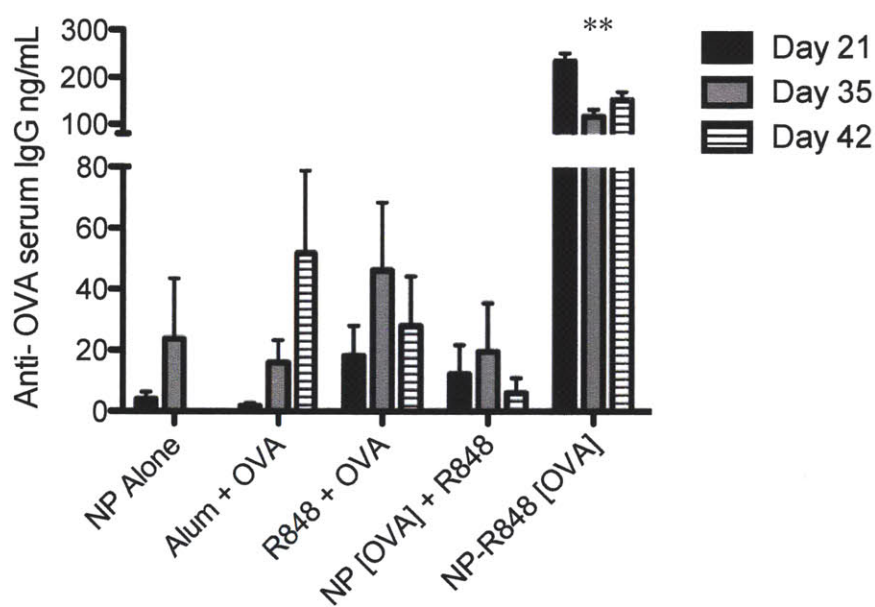


Figure 2.13 Anti-OVA IgG concentration at day 21, day 35, and day 42 after 100 ug day 0 subcutaneous vaccination. ** $p < 0.05$ by ANOVA with Tukey's post hoc test. Data shown is $n=6,7$ of two independent experiments.

To demonstrate that this nanoparticle platform in a translatable application, nicotine-PEG-PLA was formulated with R848-PLA and subcutaneously injected on day 0 with boosts on week 2, 4, and 8 [40]. As seen in Figure 2.14, nicotine conjugated on the particle mounted an antibody response in comparison to in soluble form, thereby proving that nanoparticles can increase the immunogenicity of antigen. Nanoparticles conjugated

to nicotine without R848 (green) showed decrease levels in comparison to nanoparticles with R848 encapsulated within, but could elicit an anti-nicotine antibody response. Notably the theory of encapsulating a T cell antigen, in this case OVA, within the nanoparticle in unison with adoptively transferred 5×10^6 OTII cells demonstrated a significantly increased humoral response.

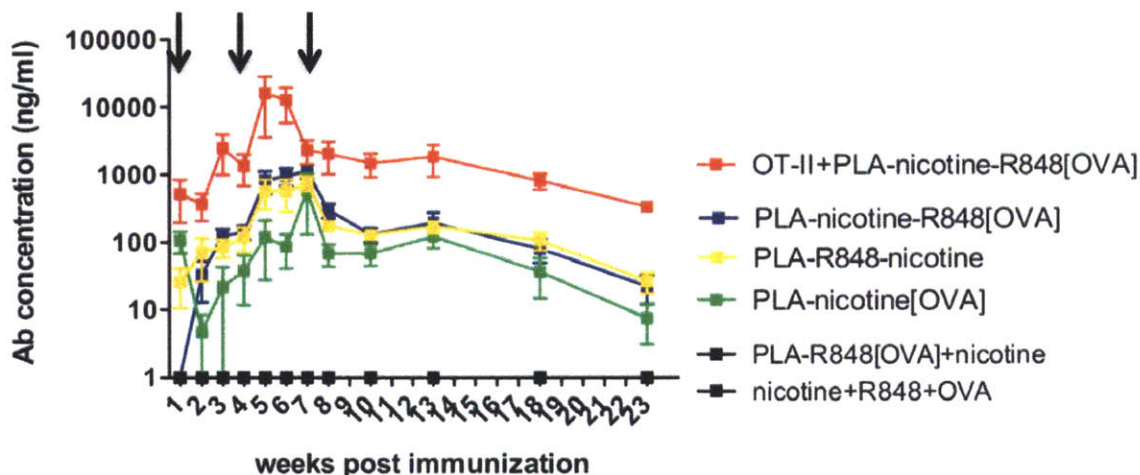


Figure 2.14 Anti-nicotine antibody concentrations of C57BL/6 mice injected with vaccine formulations at week 0, 2, 4, 8. n=4,5 of 1 experiment [40] .

2.11 Summary

We have engineered and synthesized a reproducible PLA-PEG-maleimide/ PLA-R848 nanoparticle delivery system that can efficiently prime B cells and produce potent T cell response through a single packaged dose of R848, a TLR7/8 agonist. R848-nanoparticles were able to be stable in physiological conditions and resuspended to a previous state without aggregation after lyophilization. We were able to show that R848 encapsulated nanoparticles are able to enhance antigen presentation and co-stimulatory molecules on BMDCs. Nanoparticles with and without R848 encapsulated within were able to enhance proliferation of antigen-specific naïve CD4+ and CD8+ cells *in vitro* over soluble form. C^{14} biodistribution studies indicate that at 24 hours, nanoparticles are able

to reach the spleen and lymph nodes with subcutaneous, intravenous, and intraperitoneal routes of administration. AF647-labeled nanoparticles encapsulating DQ-OVA were able to localize to lymph nodes after subcutaneous injection thereby demonstrating co-delivery of both R848 and antigen to the draining lymph node. Upon vaccination, nanoparticles delivering antigen with and without R848 encapsulated within are able to increase functional proliferation as measured by CFSE^{lo}IFN^g^{hi} populations. Humoral response against OVA indicated that nanoparticles have the potential to activate the immune system in a single bolus dose in order to provide protection in comparison to soluble adjuvant and alum, thereby if effective are able to truly mimic viruses to develop protection after a single infection. Application of the R848-PLA nanoparticle for vaccination against nicotine suggested that incorporation of a T cell antigen could provide benefit to vaccine design when antigen-specific memory T cells are present.

The lack of the significant difference between vaccine nanoparticles for OTI *in vitro* and OTI and OTII *in vivo* could be explained by trace endotoxin present in the polymer nanoparticle formulations, which may confound our experiments studying the effects of R848. The next step involves using this nanoparticle system to provide protection against lethal dose of a virus such as influenza or VSV and generation of neutralizing antibody titers in response. Additionally, if this R848-nanoparticle system can provide single dose protection, this would be revolutionary for global health delivery where patient compliance for returning to clinics for subsequent boosts are low. Further studies investigating a titration of doses to determine if one could mount a protective response without side effects.

Chapter 3. Development of a epitope specific vaccine platform applied for PCSK9 serum level reduction

3.1 Introduction

3.1.1. Background & Significance of Cardiovascular Disease in the US

Cardiovascular disease (CVD) remains the leading cause of death worldwide, and as developing countries are increasing in wealth, diseases of affluence (type 2 diabetes mellitus, obesity, cancer), may reach epidemic proportions. Since the 1970s, cardiovascular mortality rates have declined in high-income countries, yet cardiovascular deaths have increased in low to middle income countries. Around 800,000 people die annually of cardiovascular disease (CVD) in the United States, a third of nationwide deaths, and remains above cancer as the leading cause of death for both men and women. According to the CDC, in 2010, the annual total costs of CVD was estimated to be \$444 billion in combined health care expenditures and loss of productivity with coronary heart disease, hypertensive disease, stroke, and heart failure costing \$108.9, \$93.5, \$53.9, and \$34.4 billion respectively [45].

Dyslipidemia is defined as total cholesterol, low density lipoprotein cholesterol (LDL-C), triglyceride, or LP(a) levels either above the 19th percentile of HDL-C or Apo A-1 levels below the tenth percentile for the general population. The alterations in lipoprotein metabolism is often familial with a majority of patients having polygenic inheritance and having a strong influence by external factors such as obesity and the saturated fat content of a patient's diet. In the US and Europe, about 1 in 500 individuals are heterozygous for familial hypercholesterolemia. In its most common presentation, FH is a monogenic autosomal dominant disorder, impairing the function of the LDL receptor causing a reduced clearance of LDL particles from circulation and an elevation in plasma LDL-c. There are 3 gene mutations that 95% of FH patients carry: the LDL-R, apolipoprotein B (APOB) gene which impairs LDL-LDLR binding and gain of function mutations in PCSK9 with the caseload being 93, 5, and 2% respectively.

3.1.2. Current clinical treatments for hypercholesterolemia

Patients with known cardiovascular disease (e.g. myocardial infarction, angina, coronary revascularization) and coronary heart disease risk factors (e.g. type 2 diabetes mellitus, peripheral arterial disease, abdominal aortic aneurysm, symptomatic carotid artery disease) have shown benefit from treatment with statins and other agents such as niacin or fibrates in order to reduce LDL-C. Patients are recommended to undergo behavioural modification such as weight loss, aerobic exercise, and diet changes. These lifestyle modifications have shown to have significant reduction in serum total and LDL-c. In a UK trial of 2508 subjects, diet change alone, 60% of subjects had mean reduction weight of 1.8% associated with a 5-7% reduction in LDL-c. Patients with initial poor baseline diets show LDL-c reduction by as much to 30% upon switching diets [46].

Heterozygous FH patients commonly take high-dose statins (atorvosatatin, rosuvastiat, or simvastatin) for monotherapy. Homozygous FH patients are recommended to receive LDL apheresis, high-dose statin therapy and a cholesterol absorption inhibitor. FH homozygotes and heterozygotes who demonstrate resistance to standard drug therapy are treated with a variety of regimes including LDL apheresis ileal bypass surgery, portacaval anastomosis, liver transplantation, and is under investigation for gene therapy.

Although proven to significantly reduce LDL-c levels, current available therapies for hypercholesterolemia such as HMG-CoA reductase inhibitors (statins) have limitations such as poor patient compliance and side effects such as nausea, headaches, drowsiness and gastrointestinal changes. According to the IMS, the total sales in 2010 for cholesterol-treating medicines were approximately \$35 billion, including statins, and projected to rise in the upcoming years.

3.1.3. PCSK9 Regulates the LDL Receptor Recycling Pathway

A novel approach to modifying LDL cholesterol recycling with the hopes to reduce cardiovascular risk, discovered in 2003, was identified through polymorphisms in the proprotein convertase subtilisin kexin 9 (PCSK9) gene that were associated with increased severity of coronary atherosclerosis in patients with polygenic hypercholesterolemia [47]. Subsequently, meta-analysis of three large population studies, 46L allele carriers had a 12 percent reduction in LDL-cholesterol and a 28 percent reduction in the risk of ischemic heart disease [48]. PCSK9 is a serase protease protein, secreted by the liver into the plasma, which plays an important role in controlling LDL levels in the bloodstream. PCSK9, a 692 aa and 74KDa protein, is a negative regulator of surface-expressed LDL receptor (LDLR) on hepatocytes. LDL-R is essential for the

clearance of LDL-c and studies have shown that PCSK9 acts through binding to the extracellular domain of LDL-R on liver cells and enhancing the degradation of LDLR in hepatocytes[49]. PCSK9 may self-associate to form dimers and multimers, which may increase LDL-R degradation. In addition to LDL-R, the mature form of PCSK9 can bind to VLDL-R, apolipoprotein E receptor (LRP1/APOER) and apolipoprotein receptor 2 (LRP8/APOER2) to induce degradation within intracellular acidic compartments. Autocatalytic cleavage is required to transport from the endoplasmic reticulum to the Golgi apparatus and convert into the mature form that is secreted. Inactivation of PCSK9 in mice reduces plasma cholesterol levels primarily by increasing hepatic expression of LDL-R. PCSK9 has become a highly valued target for lowering plasma LDL cholesterol in order to treat and/or prevent CVD in humans since individuals carrying the loss-of-function mutation in PCSK9 exhibited an 88% reduction in the risk of coronary heart disease [48]. On the contrary, a gain of function in PCSK9 is associated with hypercholesterolemia due to increased binding of plasma PCSK9 to the membrane-expressed LDLR. The PCSK9-LDLR complex undergoes endocytosis followed by degradation in lysosomes resulting in a loss of LDLR bioavailability. Since the discovery of PCSK9, over 50 human variants have been identified that have resulted in levels of LDL-c that are either higher (LOF) or lower (GOF) than in unaltered form.

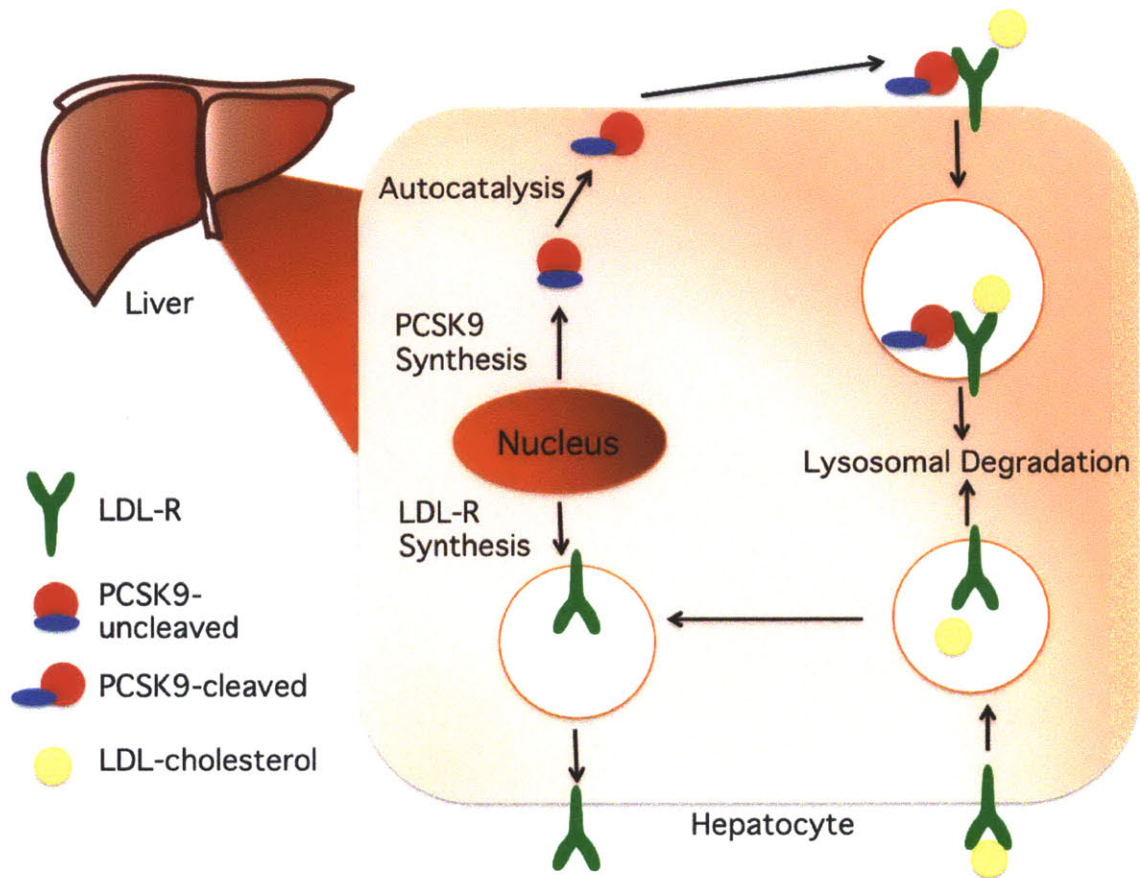


Figure 3.1 Schematic of PCSK9 pathway regulating LDL-R recycling

3.1.3. Current Therapeutics to Inhibit PCSK9

Several clinical correlates have proven that changing the binding affinity of PCSK9 to LDL-R can either reduce or increase the development of cardiovascular disease. As a drug target, PCSK9 inhibition has become of large interest from academics and pharmaceutical companies to lower cholesterol levels and has resulted in many inhibitors currently being tested in clinical trials as seen in Table 4. These therapeutics can be divided into two categories: those that 1) inhibit PCSK9 action (monoclonal antibodies and peptide binding mimetics) and those that 2) inhibit the synthesis of PCSK9 (siRNA and antisense oligonucleotides). Currently monoclonal antibodies and anti-sense oligonucleotides have shown the greatest progress in clinical trials [50, 51].

Mimetic peptides and adnectins are designed to perform as competitive inhibitors. Notable targeted binding sites were those that resemble the epidermal growth factor-like repeat A binding domain of LDL-R. Additionally, strategies utilizing LDL-R fragments or PCSK9 fragments as competitive inhibitors [52, 53]. PCSK9 fragments would effectively bind to LDL-R but due to the lack of other domains of the protein, it would disable the subsequent LDL-R degradation. Adnectins are defined as genetically engineered fibronectin-based binding proteins that are typically single domain without disulfide bonds.

The crystal structure of a complex of human PCSK9 and the EGF-A domain of LDL-R led to the discovery of monoclonal antibodies to block PCSK9 binding to LDL-R and therefore prevent PCSK9-mediated LDL-R down regulation. These antibodies have been shown to reduce the plasma LDL level in mice and non-human primates *in vivo* and increase LDL-R expression on a human hepatocyte cell line *in vitro*. There are numerous monoclonal antibodies in clinical trials that bind to the PCSK9 catalytic domain portion that interacts with the LDL-R to inhibit function: AMG145 (Amgen), 1D05-IgG2 (Merck), and SAR236553/REGN727 (Aventis/ Regeneron). These monoclonal antibodies are designed to neutralize PCSK9 and prevent its binding to LDL-R in order to decrease LDL-R catabolism and increase clearance of LDL-c. Monoclonal antibodies have the advantage of having longer half-lives and greater specificity than small molecules and peptide mimetics. Amgen 145 has shown sustained LDL-c reduction (41-66%) for statin-intolerant patients with 2 week regimens, while 4 week regimen showed LDL-c recovery between intervals.

There are numerous gene silencing mechanisms to target reduction in PCSK9 levels. Graham et al. demonstrated that an anti-sense oligonucleotide against PCSK9 resulted in a two-fold increase in LDL-R and a 38% decrease in LDL-C in mice with high lipid diets [54]. Incorporation of locked nucleic acids (LNAs) to antisense oligonucleotide sequences allowed for shorter sequences with greater binding specificity. Studies in monkeys with LNA ASO showed 85% mRNA and protein reduction and 50% LDL-C reduction for multiple weeks [55]. Lipidoid nanoparticles encapsulating PCSK9 siRNA delivered i.v. to non-human primates have shown a reduction in LDL-C by 50%. Initial results from a phase I trial with ALN-PCS02 has shown that the highest tested dose of the formulation yielded a 66% reduction of plasma PCSK9 concentration and 39% reduction of LDL-C on day 4 [56]. Long non-coding RNAs (lnc-RNA) are currently being investigated to reduce PCSK9 levels.

With many promising candidates as monoclonal antibodies and oligonucleotides requiring routine administration, it still remains to be seen if the costs of these therapeutics can reach the low/middle-income demographic which are the majority of US high-cardiovascular risk patients, but it has been demonstrated that PCSK9 is a robust target for potential cardiovascular disease prevention and treatment.

Table 4. Stages of Development of PCKS9 Therapeutics (Adapted from Do et al. [50])

Monoclonal Antibodies		
mAb1	Amgen	Preclinical
1D05-IgG2	Merck	Preclinical
1B20	Merck	Preclinical
J10, J16	Pfizer	Preclinical
J17	Pfizer	Preclinical
AMG145	Amgen	Phase 1
		Phase 2
		Phase 2/3

		Phase 3
SAR236553/	Sanofi-	Phase 1
REGN727	Aventis	Phase 2
		Phase 3
RN316	Pfizer	Phase 2
LGT-209	Novartis	Phase 2
MPSK3169A/ RG7652	Genentech	Phase 2
Peptide Mimetics		
EGF-AB peptide fragment	Schering-Plough	Preclinical
LDLR (H306Y) subfragment	NIH	Preclinical
LDLR DNA construct	NIH	Preclinical
SX-PCK9	Serometrix	Preclinical
BMS-962476 adnectin	Adnexus	Phase 1
Antisense Oligonucleotides		
ISIS 394814	Isis	Preclinical
Unnamed	Santaris-Pharma	Preclinical
SPC4061	Santaris-Pharma	Preclinical
SPC5011		Phase 1 terminated
Unnamed	Idera	Preclinical
siRNA		
LNP-PCS, ALN-PCS	Alnylam	Preclinical and phase 1 complete
PRO-040201	Tekmira	Phase 1 trial terminated

3.2 Rationale

As seen from the demonstrated potential of monoclonal antibody therapeutics against PCSK9, we hypothesize the design and development of a novel biocompatible, biodegradable vaccine carrier to control the spatial arrangement of peptide antigens in order to generate site-specific blocking antibodies to the LDLR binding region of PCSK9, which can provide a low cost method to prevent and/or treat hypercholesterolemia with the overall aim of reducing CVD risk in humans. We have developed synthetic peptide B cell antigens to mimic the structure of the PCSK9 binding site for the LDL-R EGF-A domain as predicted from *in silico* modeling. To increase the immunogenicity of peptides, we will utilize a nanoparticle platform that enables epitopes

orientated in a specific conformation on the surface of the nanoparticle. This nanoparticle carrier enables utilization of a synthetic carrier that is scalable for manufacturing and can become highly immunogenic. Nanoparticles were synthesized utilizing a polymeric nanoparticle platform that combines the ability to 1) maintain selective orientation of any synthetic epitope and 2) to enhance the density of available biotinylated peptide binding sites utilizing the availability of streptavidin at the surface. To determine the efficacy of candidate peptides, we tested the serum from immunized mice to investigate the concentration of anti-human PCSK9 antibodies, mouse-PCSK9, and LDL-c levels. We examined the ability of host generated anti-hPCSK9 antibodies to downregulate hLDL-R from HepG2. These studies will serve as a proof of principle vaccine strategy to epitope specific antibody generation against PCSK9 with the application towards decreasing CVD risk.

3.3 Methods

2.3.1 Materials:

Streptavidin, polyvinol alcohol, ovalbumin and all solvents were purchased from Sigma (S0677, A7030-50G). Tween 20 (Calbiochem 655265). NH₂-PEG-biotin was purchased from Laysan Biopolymers. Poly(DL-lactide-co-glycolide) was purchased from Boehringer Ingelheim (i.v. 0.45). Peptides were custom synthesized through American Peptide Company at 95% purity. CPG type C and Endofit Ovalbumin were purchased from Invivogen (ODN2395). N-hydroxysuccinimide (24500), 1-Ethyl-3-[3-dimethylaminopropyl] carbodiimide hydrochloride (77149) was purchased from Thermo Scientific/ Pierce. ELISA Rag2^{-/-} OTII mice were from in house colonies, while C57BL/6 mice were purchased from Charles River.

2.3.2 Instrumentation:

¹H were performed on a Bruker 400 spectrometer. Particle size (diameter, nm) and surface charge (zeta potential) measurements were made using a Malvern Nano ZS with ZetaSizer Software 6.32. Experiments were performed in DNase free water unless specifically noted and viscosity and refraction indices were set to those equal to water. Average electrophoretic mobilities were measured at 25C using Malvern data analysis software and the Smoluchowsky model for aqueous solutions. Size (nm) and zeta potential (mV) is expressed as an average of 3 measurements of 10 runs +/- standard deviation. HPLC measurements utilized Agilent 1100 with Chemstation A.10.01.165. GPC measurements used Viscotek 5200 with OmniSec 4.51.554 software.

2.3.4 Synthesis of PLGA-PEG-biotin Block Copolymer

PLGA-PEG-biotin was synthesized via EDC/NHS conjugation. 1 gram of vacuum-dried PLGA in 4 mL of chloroform mixed with 50 ug (0.250 mmol, 5 mol eq) of EDC and 28 ug of NHS (0.250 mmol, 5 mol eq) for 15 minutes. 1 gram of NH₂-PEG-biotin dissolved in 1 mL of chloroform was added for an overnight conjugation reaction. PLGA-PEG was precipitated in 50:50 ice cold ether: methanol solution and centrifuged at 4000 rpm for 10 minutes and subsequently dissolved in acetonitrile and washed in methanol twice. The resulting block co-polymer was characterized by GPC and NMR. $M_n = 19780$ (THF GPC).

2.3.2 Biotin-Streptavidin Nanoparticle Platform Formulation & Characterization:

Nanoparticles were synthesized by double emulsion through first dissolving 0.25 mL of 13.2 mg/mL PLGA-PEG-biotin within 0.75mL of dichloromethane, subsequently vortex 0.25 mL of 2 mg/mL ovalbumin solution with 0.25 mL of dH₂O and sonicating for 15s on homogenizer at 30% with 2 mL 1 %w/v PVA and a secondary 15s sonicator.

Subsequently, we added 40 mL of H₂O to spin for 1.5 hours and then wash 3x in H₂O in 100K MWCO Amicon filters. Nanoparticles were measured for appropriate size and charge. 1 mg of nanoparticles were added to 100 uL of 10 mg/mL streptavidin and spun for 30 minutes at room temperature. The nanoparticles were then subsequently dialyzed for 2 hours with 10⁶ MWCO dialysis membrane (SpectraPor) and subsequently sized and charged to ensure lack of aggregation. 1 mg of the streptavidin conjugated nanoparticles were added to 1 mg of peptide at 5 mg/mL and shaken overnight. Stock solution of peptide 1 and 1' at 5 mg/mL had 1 uL of 8%w/v NH₄OH added to facilitate solubility. The nanoparticles were subsequently washed three times with a 100K Amicon filter.

2.3.3 Assay for determination of available active binding sites:

100 ug in 20 uL of PLGA-PEG-biotin-streptavidin nanoparticles were incubated with increasing levels (0, 0.1, 1, 2, 5, 10 mg/mL) of soluble biotin in 200 uL and stirred for 2 hours. Unbound biotin were subsequently washed off through 3 dH₂O washes in a 100K Amicon filter. Nanoparticles were added to separate stirring solutions of 100 ug of fluorescein-biotin at 2 mg/mL for 1 hour. Unbound fluorescein-biotin were subsequently washed off through 3 dH₂O washes in a 100K Amicon filter. The absorbance of 100ug of nanoparticles in 100 uL was read at 494 nm.

2.3.3 PCSK9 Nanoparticle Vaccination:

Based on the concentration of PLGA-PEG-biotin polymer, 200 ug of nanoparticles with 14 ug of CPG in 1x 7.4 pH PBS (Invitrogen) were subcutaneously injected per C57BL/6 female mouse, aged at 6 weeks, in the base of tail and both footpads at day 0 with a boost at day 28. Nanoparticles were sterile filtered in 0.2 um filters prior to injection. Serum was taken at day 10 and day 38 for analysis.

2.3.4 WT-PCSK9 & GOF-PCSK9 LDL-R Binding Assay:

HepG2 cells were transfected with lipofectamine + plasmids containing either the WT-hPCSK9 or GOF-hPCSK9 sequence (Appendix A1.1, A1.2) and selected twice with geneticin. Transfected cell lines were plated in a 48 well plates with 5×10^5 cells/ well. Media (100ul) was changed 2-4 hours prior to transfection. 12ul Lipofectamine + 288ul of OPTI-MEM (300ul). 4.8 ug DNA in 300ul of OPTI-MEM (300ul) were mixed for 20 minutes prior to placing 50ul per well. After 12 hours, change media (100ul), wash 1X with PBS. Serum was placed in wells at two different dilutions 1:4 (25 uL serum) for 48 hours prior to flow cytometry of the LDL-R expression using 20 uL of APC hLDL-R (R&D FAB2148A).

2.3.5: Assays for mPCSK9, LDL-c/HDL-c, and anti-hPCSK9 antibodies:

ELISAs were performed for serum at day 10 and day 38 at 1:200 dilution utilizing a sandwich Quantikine ELISA for mouse PCSK9 (R&D MPC 900). LDL-c/HDL-c levels were quantified using cholesterol assay kit (Abcam ab65390). Anti-hPCSK9 antibodies were assayed using 0.10 ug/well recominant hPCSK9 (R&D 3888-SE-010) plated on 96 well MaxiSorp plates (VWR 62409-024) with mouse anti-hPCSK9 (MAbCL 410420) as a standard. Serum was assayed at 1:200 dilution for all cohorts. Anti-mouse IgG-HRP, Anti-mouse IgG1-HRP, and Anti-mouse IgG2-HRP (Southern Biotech 1030-05, 1070-05, 1079-05) were used for secondary detection followed by TMB (Pierce 34028) for 15 minutes prior to 2M sulfuric acid stop solution and read at 450 nm.

3.3 PCSK9 Epitope Selection

In order to elicit an antigen-specific B cell response, epitopes were selected via *in silico* modeling to identify key epitope candidates that can precisely mimic the PCSK9

binding site for LDL-R. Analysis of the crystal structure of PCSK9-EGF A complex indicates that the structures of PCSK9 and PCSK9-EGF-A are almost identical except for a subdomain located within the C-terminal domain of PCSK9 (residues 532-601)[57]. Epitope candidates were selected as seen in Table 4. Candidate 1 is a structural region which binds LDL-R, while Candidate 1' is the same region with end modifications to include a disulfide bridge to stabilize the 3D structure of the epitope. The crystal structure of PCSK9 in complex with a Fab fragment of the blocking monoclonal antibody[58] indicates that the antibody sterically hinders the binding of PCSK9 to the EGF-A domain of LDL-R making the antibody binding motif a viable candidate (Candidate 2) as seen in Figure 3.2. Candidate 3 is another predicted binding region of LDL-R but due to the determined epitope length and lower degree of homology between human and mouse, we did not further pursue utilizing this candidate epitope in this thesis.

Table 5. PCSK9 epitope candidates for nanoparticle B antigen

Candidate	Residue	Human Mouse	% Homologous
1	366-383	EDIIGASSDCSTCFVSQS KDIIGASSDCSTCFMSQS	88.9%
1'	366-383	EDCIGASSDCSTCFVSCS KDIIGASSDCSTCFMSQS	77.8%
2	209-224	PEEDGTRFHRQASKCD PEEDGTRFHRQASKCD	100%
3	153-181	SIPWNLERITPPRYRADEYQPPDGGSLVE SIPWNLERIIPAWHQTEEDRSPDGSSQVE	57.1%

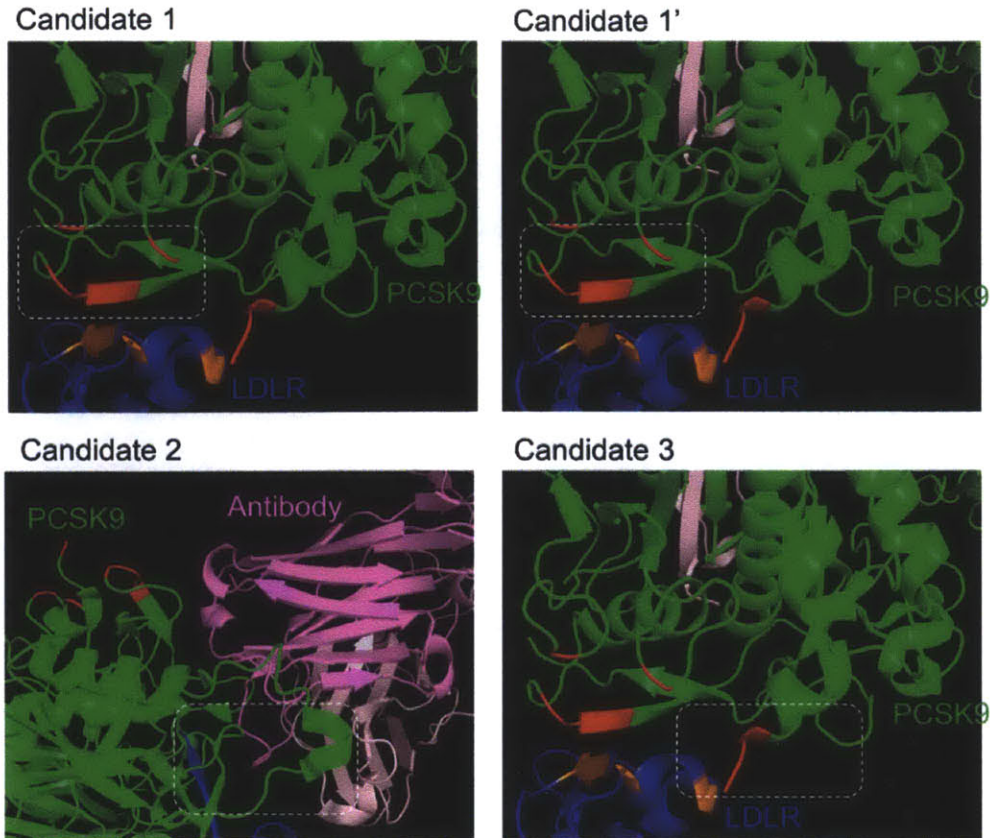


Figure 3.2 Three-dimensional ribbon diagrams illustrate the location of the predicted epitopes of all four candidates as recommended by Professor Timothy Springer.

3.4 Nanoparticle Synthesis & Characterization

Due to several layers of proteins, nanoparticles were synthesized, measured for biotin loading site availability and characterized for stability/ reproducibility. The nanoparticle platform was developed with utilizing the concept that the avidin family has four binding sites for biotin, thereby allowing an increase in the surface functionality for available binding sites of biotinylated synthetic peptides, as seen in Figure 3.3 A. Nanoparticles were synthesized using double emulsion to encapsulate a T antigen. For our applications in mice, we used the model protein ovalbumin, but for human clinical translation we would use an antigen that we have developed CD4+ immunity against, such as tetanus toxoid. Although we did not utilize an adjuvant conjugated polymer for

this work, PLA-R848, or an analogous immunostimulatory polymer, could be blended with the PLGA-PEG-biotin for clinical translation. For our study to determine whether peptide epitopes can elicit antibodies that recognize and inhibit human PCSK9, we have used soluble CPG, a proven potent TLR9 ligand in mice.

Variable	Value
T Antigen Loading (ug/ mg polymer)	15 +/- 0.2
Peptide on the surface (ug/ 100 ug polymer)	3 +/- 0.5
Size (nm)	223 +/- 12
Zeta Potential (mV)	-5- -18 +/- 3

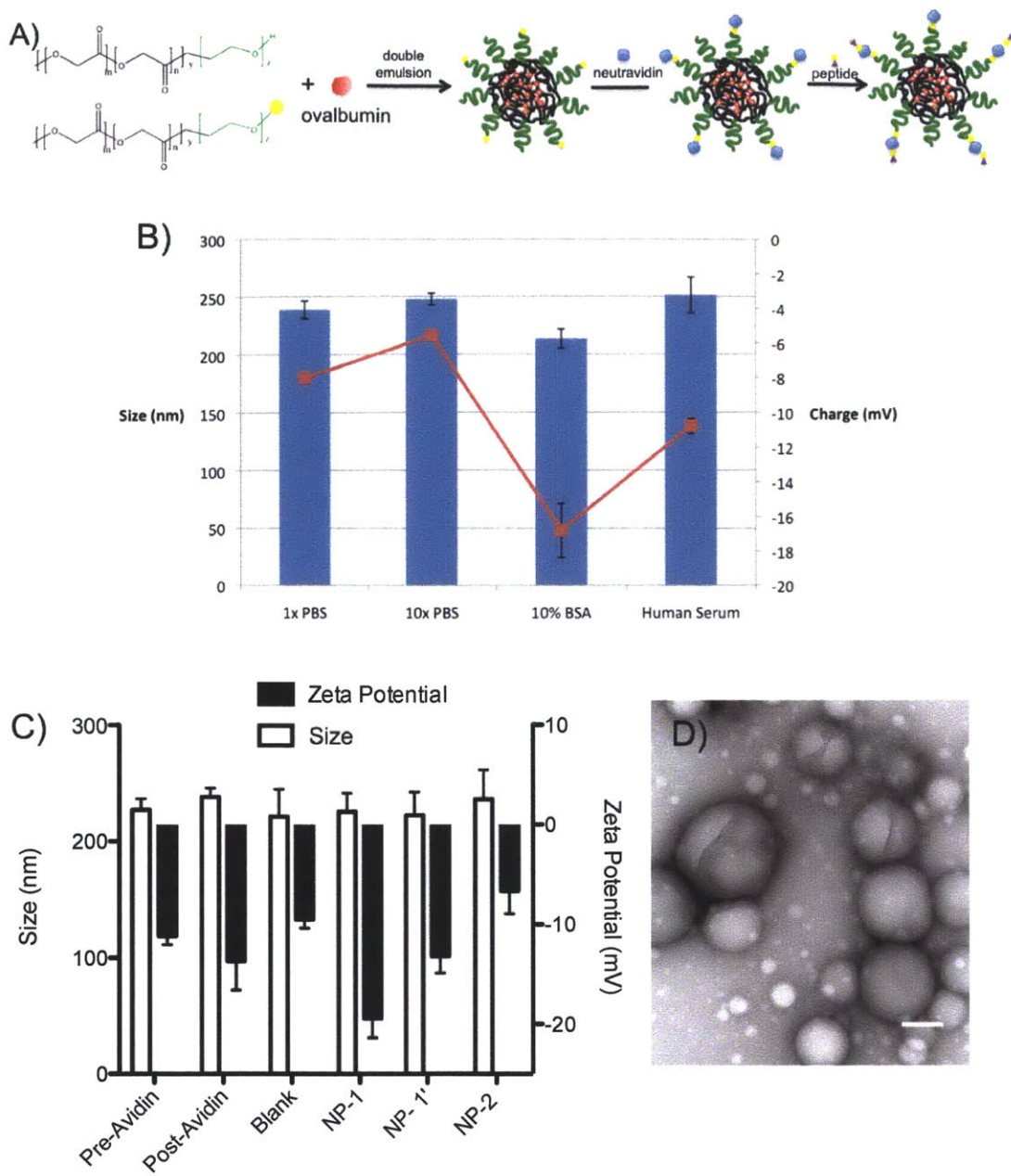


Figure 3.3 A) Schematic of biotin-streptavidin-biotin-epitope nanoparticle formulation. B) Nanoparticle stability of OVA₃₂₃₋₃₃₉-biotin- NPs in physiological conditions. n=3 C) Size and charge of nanoparticle formulation using streptavidin and candidate epitopes in water, n=12 D) TEM of nanoparticle formulation of OVA₃₂₃₋₃₃₉-biotin- NPs, bar is 100 nm.

In determining the type of avidin to use for conjugation, we compared properties of interest as seen in Table 5. We initially used neutravidin due the lowest reported non-

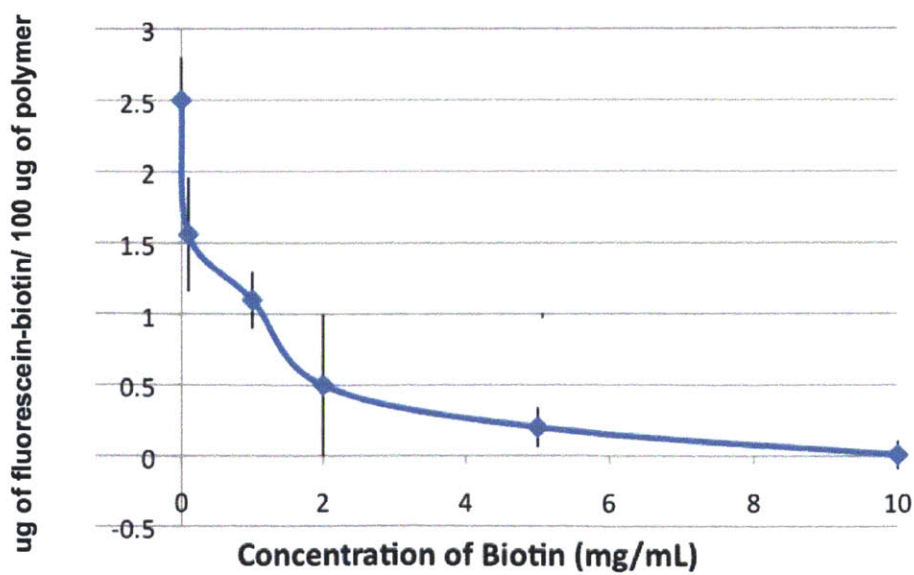
specific binding, but reproducibility issues and nanoparticle aggregation due to batch variation of neutravidin lead the switch to streptavidin. The concentration of avidin protein to PLGA-PEG-biotin must be high to oversaturate the surface of the nanoparticle in order to avoid aggregation. To determine if the nanoparticle platform is stable in physiological conditions, we used biotinylated OVA₃₂₃₋₃₃₉ for surface conjugation and optimization of the synthesis (Figure 3.4 A). After the nanoparticle is optimized, we utilized identified biotinylated epitopes of PCSK9. Reproducibly, Candidate 1 produced more negatively charged nanoparticles (-19 mV +/- 2.5 mV) in comparison to other candidates, which is important as nanoparticles with larger charge has been seen to be more prone to macrophage uptake (Figure 3.4 B). TEM images indicate a heterogenous distribution of nanoparticles under 300 nm without aggregates (Figure 3.4 C), which fits in the <400 nm size range for the nanoparticles to enter the lymph node.

Table 6. Comparison of available Thermo Scientific Biotin-Binding Proteins.

	Avidin	Streptavidin	Neutravidin
Molecular Weight	67K	53K	60K
Biotin-binding Sites	4	4	4
Isoelectric Point (pI)	10	6.8-7.5	6.3
Specificity	Low	High	Highest
Affinity for Biotin (K _d)	10 ⁻¹⁵ M	10 ⁻¹⁵ M	10 ⁻¹⁵ M
Nonspecific Binding	High	Low	Lowest

To assess the coupling efficiency of the biotinylated peptide candidates, we first measured the binding capability of our streptavidin conjugated nanoparticles to soluble

fluorescein-biotin after blocking the number of sites with free biotin at different concentrations (Figure 3.4). We determined that 100 ug of PLGA-PEG-biotin-streptavidin nanoparticles were able to have a maximum fluorescein-biotin loading of 2.6 +/- 0.4 ug and chose the concentration of biotinylated peptides to incubate these nanoparticles with to saturate available binding sites is 5 mg/mL (Figure 3.4 A). Upon overnight 12 hour incubation selected biotinylated peptide candidates, subsequent incubation with fluorescein-biotin resulted in 1-1.5 ug bound peptide per 100 ug of polymer nanoparticle (Figure 3.4 B). With the assumptions of the density of PLGA particles at 1.28 g/cm³ (average range 1.22-1.34 g/cm³) with the average nanoparticle diameter at 225 nm and maximum biotin loading at 3 ug/ 100 ug of polymer, the calculated number of binding sites per particle is 4.42x10⁵ and maximum loading of candidate 1 peptide (MW 2093 g/mol) is 8.43 ug/ 100 ug. Since the amount of surface loading of biotinylated peptide is 1-1.5 ug, the amount of peptide on the surface of 100 ug of nanoparticles is 2.8-4.2 ug.



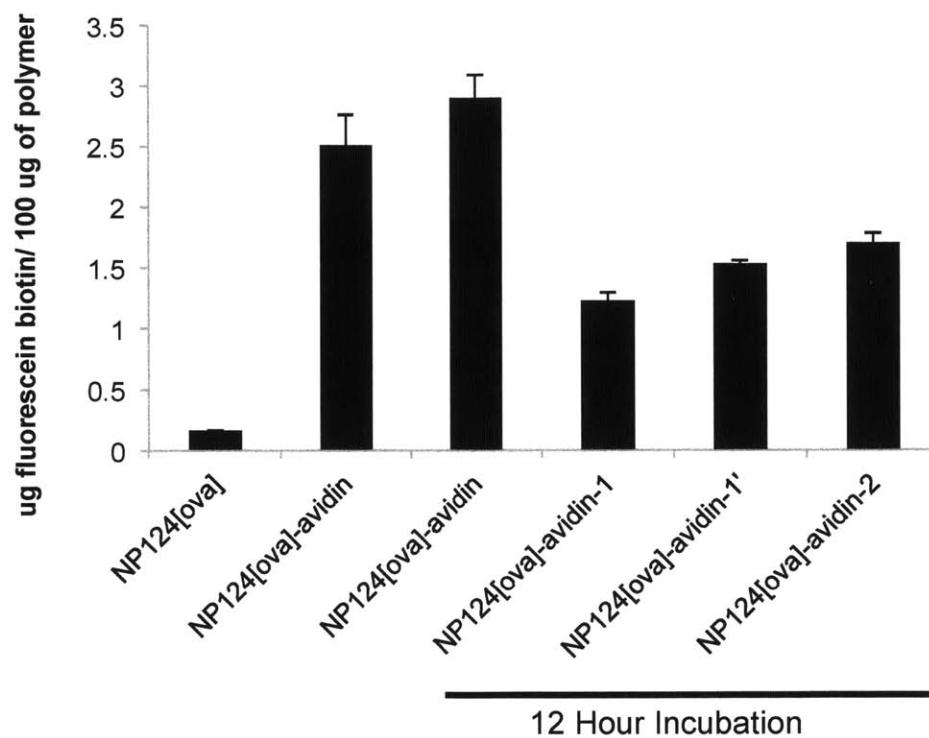


Figure 3.4 Assessment of available biotin binding sites on PLGA-PEG-biotin-streptavidin nanoparticles with fluorescein-biotin A) Free biotin was incubated with 100 ug of nanoparticles prior to fluorescein-biotin to find the lowest concentration for available binding site saturation, n=4 B) Amount of fluorescein-biotin binding after incubation with associated peptide candidates n=6

To determine whether the T cell antigen encapsulated within the PLGA-PEG-biotin nanoparticle was able to activate antigen-specific CD4+ cells *in vivo*, we performed an adoptive transfer assay using CFSE-labelled OTII (ovalbumin specific CD4+) cells with the timeline depicted in Figure 3.5. On day 3, nanoparticles[OVA] + CPG were able to induce antigen-specific proliferation similar to antigen + CPG alone and than nanoparticle[OVA₃₂₃₋₃₃₉] + CPG even with the amount of OVA peptide at 0.9 ug/ 100 ug polymer and amount of OVA at 1.2 ug/ 100 ug polymer. This data highlights the purpose and potential of designing an encapsulated T antigen to elicit the help of the memory CD4+ cells against a toxin/protein in order to mount a synergistic immune response.

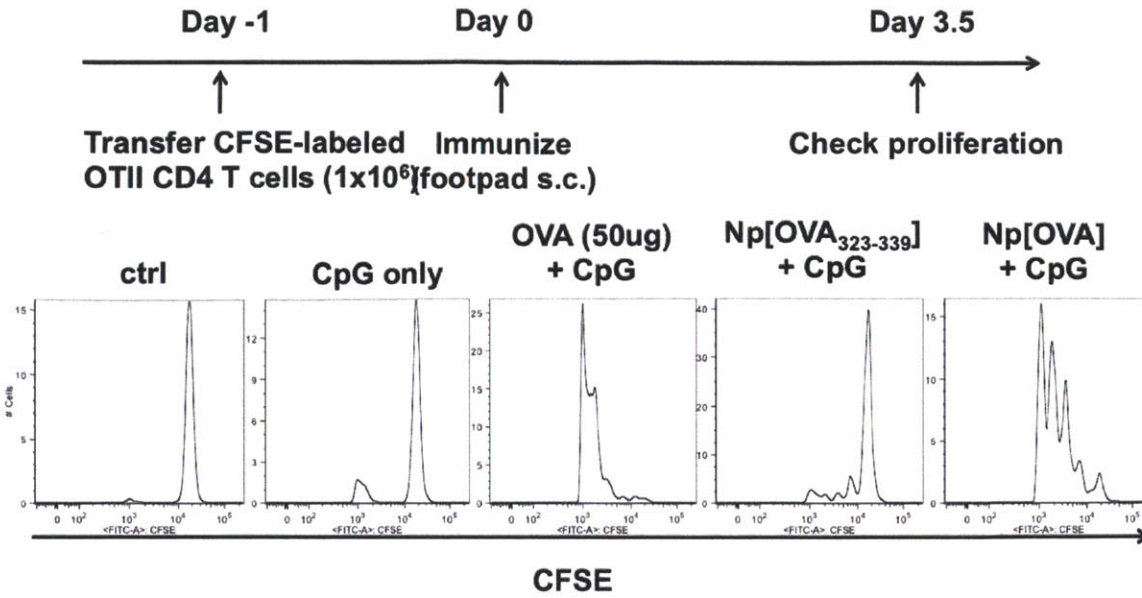
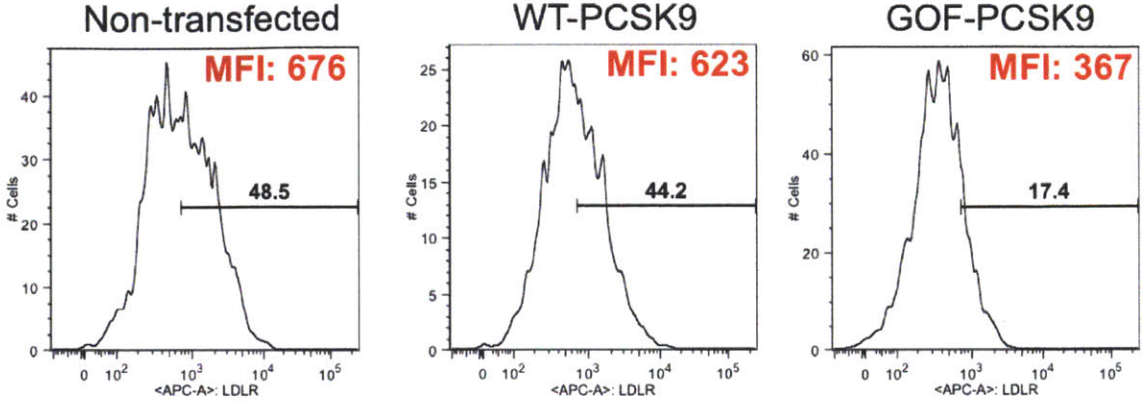


Figure 3.5 Vaccination timeline of CFSE labeled OTII cells after adoptive transfer on Day -1 and immunization with nanoparticles on Day 0; followed by histograms of CFSE labeled OTII cells on Day 3 with varying vaccination protocols.

3.5 In Vitro LDL-R knockdown with Sera from Immunized Mice

To determine if antibodies against human PCSK9 were generated in immunized mice, an *in vitro* assay was developed utilizing HepG2 cells transfected with either WT-PCSK9 or GOF-PCSK9 (D374Y mutation) to emulate LDL-R recycling in common and pathological conditions. Cells transfected with GOF-PCSK9 decreased LDL-R surface expression in comparison to WT-PCSK9 as seen in Figure 3.6 A. After 48 hour incubation with sera from immunized mice at day 38, presence of blocking anti-human PCSK9 antibodies were assessed to determine whether functional inhibition of PCSK9 binding to LDL-R occurs. Sera from mice immunized with peptide candidate 1 and 2 trended to show increased antibody activity to reverse the production of PCSK9 and LDL-R for both WT-PCSK9 and GOF-PCSK9, thereby indicating that these selected synthetic peptides were able to mount an epitope-specific CD4+ response. Although the

HepG2 were only transiently transfected, data over three experimental repeats suggest that nanoparticles with candidates 1 and 2 could increase surface expression of LDL-R. Cell lines that are stably transfected may provide data with consistent starting LDL-R levels.



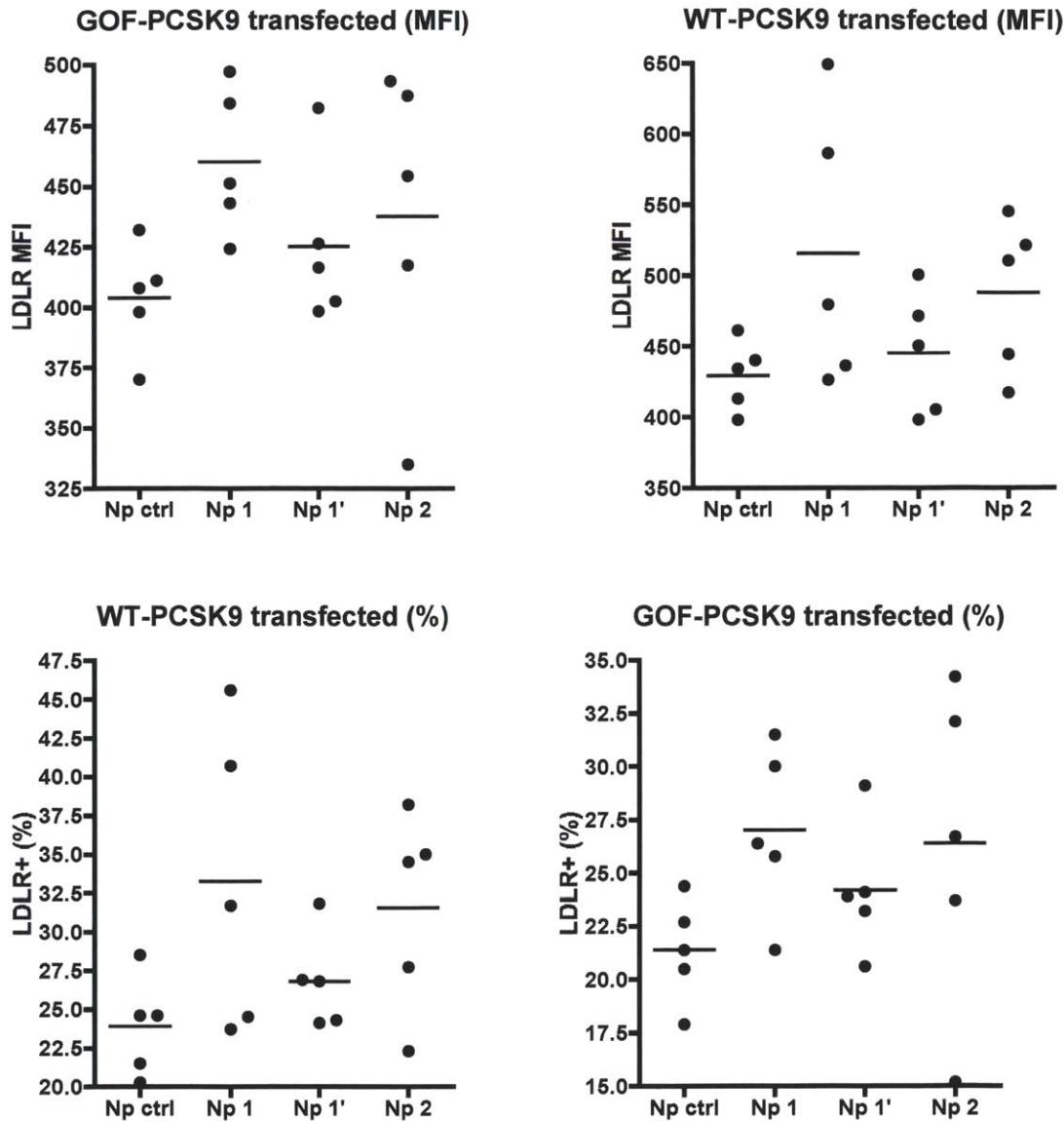


Figure 3.6 A) Histograms depicting LDL-R levels on the surface of non-transfected, WT-PCSK9, and GOF-PCSK9 HepG2 cell lines B) Day 38 sera on transfected HepG2 cell lines n=5, 2 experimental repeats.

3.6 In Vivo mPCSK9 Reduction and α -hPCSK9 IgG Increase

Mouse PCSK9 and anti-human PCSK9 IgG levels were characterized to determine if antibodies in the sera, as demonstrated by Figure 3.6 B, were cross reactive with mouse PCSK9 since all three human PCSK9 candidates used were >75%

homologous with mouse (Table 5). Mice immunized with nanoparticles with epitope candidate 2 showed a significant 48% reduction ($p < 0.01$) in serum PCSK9 levels in comparison with controls on day 38, while candidate 1' demonstrated a notable trend in lowering serum PCSK9. There was no overall significance of PCSK9 levels on day 10, notably some vaccinated mice showed increased levels of PCSK9. Levels of mouse anti-human PCSK9 (Figure 3.7 B) indicates that epitope candidate 1 and 2 were able to produce epitope specific antibodies that can explain the *in vitro* results (Figure 3.6 A). Although these results appear promising, antibody affinity is unknown and can be assessed by surface plasmon resonance (SPR) against both human PCSK9 and the epitope to assess the candidate epitope that develops high affinity, specific antibodies against our epitope candidates.

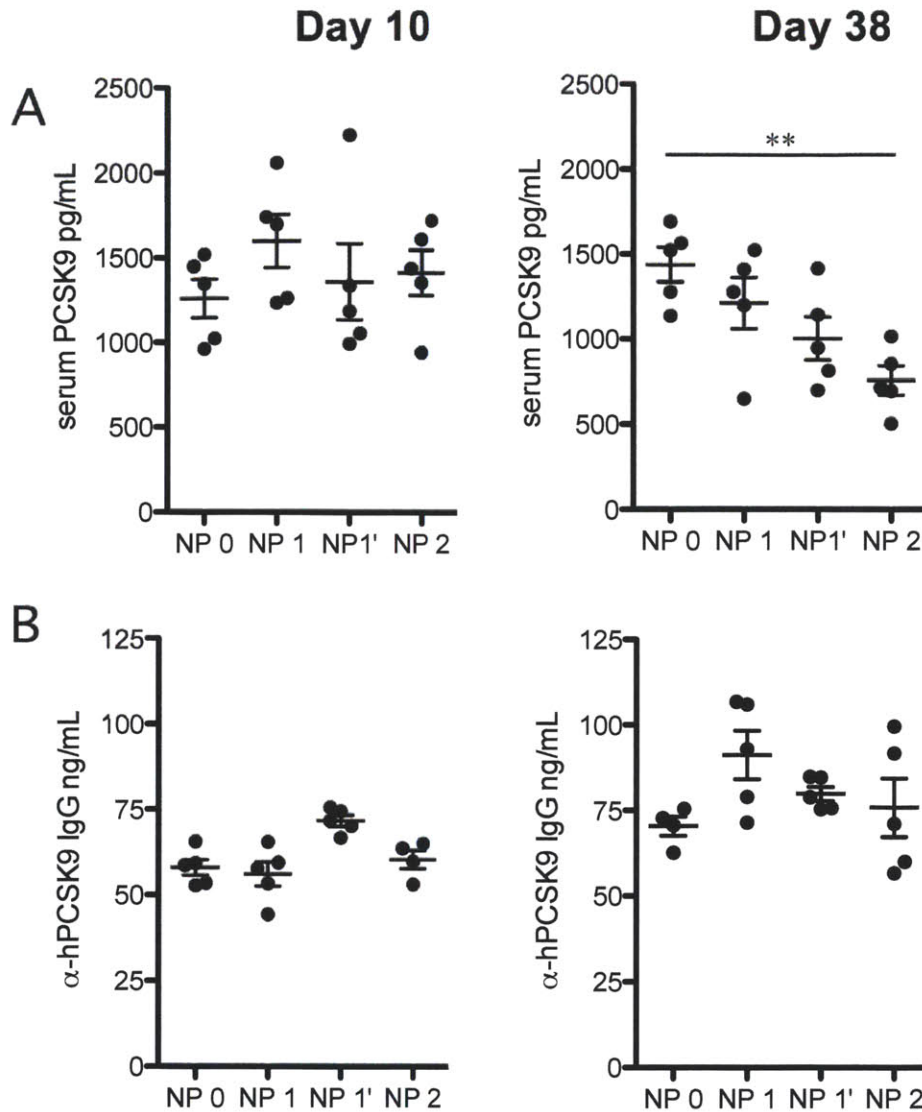


Figure 3.7 ELISA results for mouse PCSK9 levels and anti-hPCSK9 IgG levels in the serum at day 10 and day 38 after immunization on day 0 and day 28. A) Levels of mouse PCSK9 assessed by ELISA in 1:200 serum dilution at day 10 and day 38. ** $p < 0.01$ by ANOVA with Tukey post test. B) Anti-human PCSK9 IgG levels demonstrate mice immunized with nanoparticle vaccines with candidate epitopes have increased levels of human PCSK9 specific antibodies. Data representative of two experimental cohorts.

3.7 Nanoparticle Vaccines have potential to Reduce LDL-Cholesterol *In Vivo*

Sera from vaccinated mice were tested for LDL/VLDL and HDL levels (Figure 3) at day 10, day 38, and day 212. HDL levels are typically monitored in conjunction

with LDL to ensure that other parts of the lipid metabolism have not been altered. Notably, in with our vaccine, HDL levels consistently produces more noise than the LDL/VLDL, which maybe attributed to the isolation of HDL from the kit itself. At Day 10, serum LDL/VLDL and HDL levels were unaffected, yet at Day 38, there is a notable decrease in LDL/VLDL for candidate 2, in comparison to control nanoparticle 0, which corresponds favorably with decreases in mouse PCSK9 and increased the trend in anti-PCSK9 antibodies. At Day 212, a notable overall lowering of LDL/VLDL levels for nanoparticles with candidate 1 and 2 suggests that these two candidate epitopes are promising to induce a long-lasting humoral response against PCSK9.

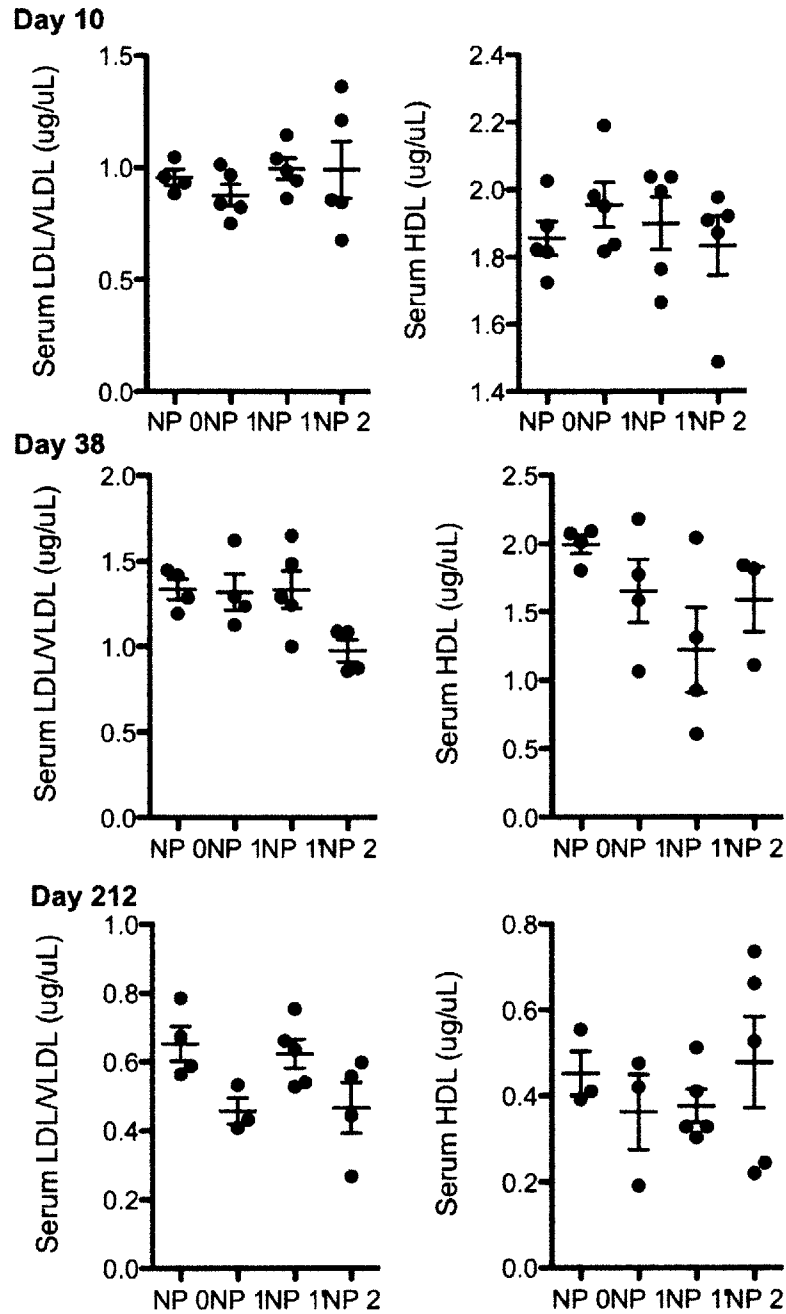


Figure 3.8 Serum LDL/VLDL and HDL levels in vaccinated mice at day 10, 38, and 212. Day 10 and day 38 are representative of two cohorts, day 212 represents one cohort. n=4,5

3.5 Summary & Future Directions

We have developed a nanoparticle formulation based on streptavidin-biotin conjugation that enables selective orientation of epitopes on the surface that suggests that targeted vaccination against PCSK9 may be a strategy to reduce the risk of CVD. Candidate epitope 2 shows promise for further study, which is notable since it is the epitope of anti-PCSK9 monoclonal antibody in clinical trials.

Future directions include repeating these studies with a larger cohort for each epitope and determining whether an additional boost on day 58 may help mount a more significant response. Inclusion of initial readings of murine PCSK9, anti-human PCSK9 and cholesterol levels per mouse with the difference over time as a readout to minimize endogenous differences between each mouse can serve to minimize the amount of noise per mouse. Additionally, assaying hepatocyte LDL-R expression after vaccination may demonstrate reduction in endogenous PCSK9 through cross-reactive antibodies produced by this vaccination. This strategy is essentially mounting an autoimmune response against self, it is to be seen the long term effects of this vaccination after 212 days and whether the immune system will identify and destroy self-autoreactive clone which may require additional vaccinations if humoral response tapers. To make this formulation clinically translatable, an adjuvant construct would be introduced for the advantages listed in Chapter 2 of this thesis. Addition of R848-PLA to replace CPG or even to act in synergy with CPG may confer a more potent immune response. Although the biotinylated nanoparticle platform provides additional surface for conjugation, it remains to be seen how the density compares to other means of bioconjugation, such as maleimide-thiol chemistry as seen in Chapter 2. Surface plasmon resonance could be utilized to analyze

the surface density or high resolution SEM to choose the platform that would provide the optimal surface density to emulate the surface density of glycoproteins on virus capsids.

Although we have shown promise for candidate 1 and 2 utilizing our nanoparticle platform with a readout of reduction in murine PCSK9 levels, increases in human anti-PCSK9 IgG and LDL/VLDL levels, to determine the ability of these nanoparticles to function to reduce atherosclerosis or CVD risk, vaccination of transgenic mice must be tested. Mice commonly used for atherosclerosis are LDL-R^{-/-} and ApoE^{-/-}. Since LDL-R is a dependent readout in our studies, LDL-R^{-/-} would be counterproductive as a model. ApoE^{-/-} provides the advantage of spontaneous development of atherosclerosis but the majority of the plasma cholesterol is VLDL, not HDL as in human [59]. ApoE*3-Leiden (E3L) Tg Mice display a moderate hyperlipidemia profile in comparison to ApoE^{-/-} or LDLR^{-/-} and are closer to human vascular pathology. PCSK9 mouse (Pfizer) has a transgene expressed in the kidney with overall reduction in endogenous PCSK9 expression and elevated human PCSK9 levels. Additionally, hydrodynamic tail vein injection with hPCSK9 integrated in the sleeping beauty plasmid is known to stably transfect hepatocytes in vivo with a slight increased risk of cancer. Human PCSK9 transfected mice can be used as a model to study the vaccine immune response against its intended target. Although both ApoE transgenic mice are known to develop atherosclerotic plaques on a high-fat diet, the PCSK9 murine model needs to be assessed for as an atherosclerotic model. The vaccine should be given 6 weeks and then subsequently at 28 days afterwards as conducted in this work. Upon the start of a cholesterol and cholate rich diet, the thickness of plaques on the carotid or femoral

arteries can be compared between epitopes in vaccinated mice [60]. These murine models will help assess whether vaccination against PCSK9 can alleviate the risks of CVD.

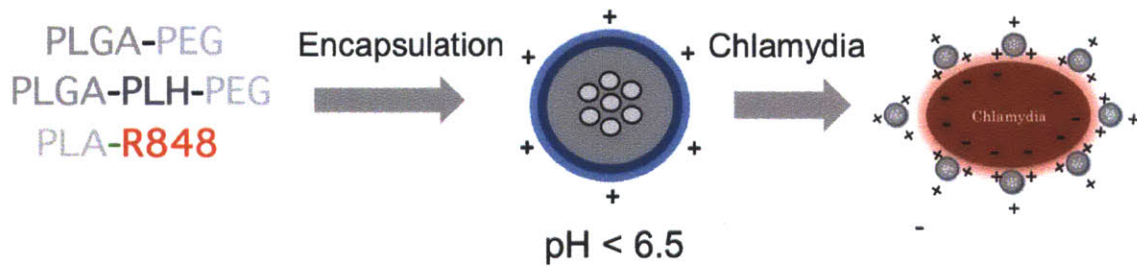
Chapter 4. Future Directions

4.1 Summary

Novel vaccines afford the possibility of providing prophylactic protection for pathogens that have been unable to be vaccinated against for using conventional treatments and provide an alternative option to treat chronic diseases. As our community learns more about the pathogenesis and discover new immunological mechanisms, we are able to incorporate these findings towards providing better treatments. This thesis investigated the usage of polymeric nanocarriers to serve as synthetic vaccine constructs with the ability to 1) integrate small molecule adjuvants to deliver a potent payload of antigen and adjuvant in secondary lymph nodes and 2) create a platform that can place epitopes in a conformational order. We showed that the adjuvant conjugated to polymer provided a better safety profile, prolonged its therapeutic window, and showed that at a small dose is able to mount a cell-mediated and humoral response in comparison to its soluble form. In Chapter 3, we explored the concept of selecting precise epitopes *in silico* to generate autoimmune response against a self protein to decrease levels of LDL-cholesterol. We showed that two promising candidates were able to reduce mouse PCSK9, increase LDL-R *in vitro* and showed a promising trend of lower LDL-c over time. This proof-of-concept demonstrates that we can systematically engineer an immune response against a self antigen, which can also be applied as a therapeutic vaccination against other pathologies.

4.2 Next generation vaccines against infectious disease

As we have described the therapeutic potential of R848-PLA nanoparticles to a model protein, ovalbumin. To apply the R848-PLA nanoparticle platform towards prevention against a pathogen, we showed that if we design a vaccine that incorporates a polymer (PLGA-PLH-PEG) to specifically bind to the surface of UV-inactivated bacteria[61], we can use the entire bacterium as a carrier to ease manufacturing scale-up from lysing or using synthetic proteins (Figure 4.1 A). qPCR data of chlamydia load in the uterus after challenge indicates that NP-UV inactivated bacterium constructs can provide protection equivalent only to inoculation with live bacteria (Figure 4.1 B) and notably providing more protection than combined with free R848 and the carrier alone [61, 62]. These pathogen-particle constructs are a new vaccine platform that can be applied to other mucosal pathogens that have been traditionally difficult to vaccinate such as tuberculosis and staphylococcus.



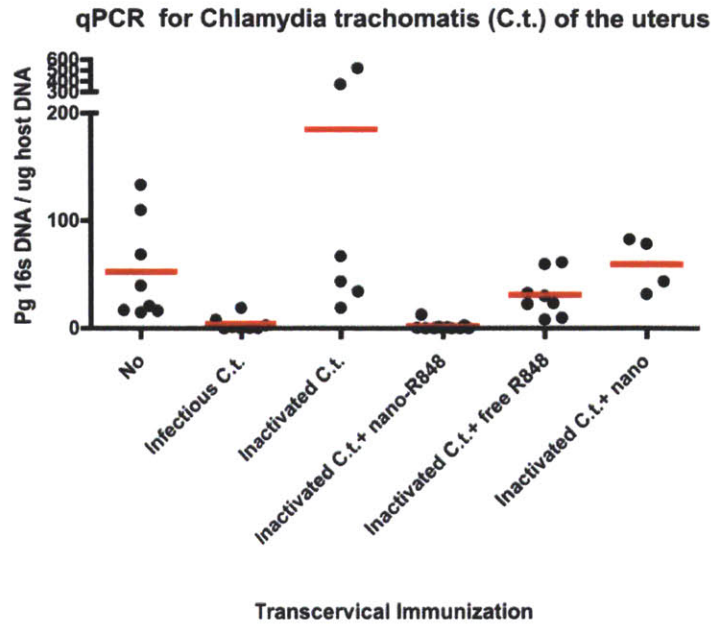


Figure 4.1 A) Schematic of nanoparticle vaccine for Chlamydia trachomatis B) Chlamydia loads via qPCR of the uterus on day 6 after challenge after transcervical immunization 4 weeks prior. Data by Georg Stary and Aleksandar Radovic-Moreno. Reproduced from [62, 63]

4.2 Non-traditional epitopes for cancer vaccine development

Vaccines against cancer have been an elusive target and although showing promise in murine models have had difficulties in translating to the clinics. The immune system plays a crucial role in tumour progression as been highlighted in patients through several observations: 1) intratumoral immune responses can predict prognosis, 2) spontaneous immune response in cancer patients (paraneoplastic syndrome), and 3) immunodeficient patients are associated with higher cancer risks [64]. It has been demonstrated that cancers with higher clinical staging have evolved to evade the host immune system through a combination of mechanisms including but not limited to: generation of an immunosuppressive tumour environment thereby reducing the host's or induced cell-mediated immune response and a reduction in tumour antigens [65]. Future immunotherapy may include a combination of thrusts focusing on increasing both the

quantity and the quality of effector cells, discovery of new tumour antigens, and methods to reduce or inhibit the molecular/cellular mechanisms involved with cancer-induced immunosuppression.

Table 7. Clinically available or ongoing clinical trials of cancer vaccine candidates

Company	Candidate	Cancer	Phase	Method
Antigenics	Oncophage	renal glioblastoma	clinically available	hsp- lysate
Dendron	Sipuleucel-T, Provenge	prostate	clinically available	adoptive transfer
Cuba's Center of Molecular Immunology	CimaVax-EGF	Lung Cancer	N/A	N/A
Panacela Labs	MOBILAN		preclinical	Adenovirus
Dendreon Corp	DNDN, Neuvence	Breast, Bladder, Colon, Ovarian	I	fusion peptide- GMCSF
Celldex Therapeutics	CDX110, CDX1307 and CDX1401	glioblastoma	I-III	mAb, antibody-drug conjugates
Heat Biologics	ImPACT	NSCLC		
Geron Corporation	GRNVAC1	multiple melanoma	II	telomerase targeted
BN ImmunoTherapeutics	PROSTVAC	prostate cancer	III	
Globelimmune	Tarmogens, GI-4000, GI-6207, GI-6301	NSCLC, breast	I-III	brachyury protein/ yeast
Advaxis	ADXS11-001, ADXS31-001, ADXS31-164	prostate, cervical	I-III	electroporation DNA vaccine, fusion peptide
Accentia Biopharmaceuticals	BiovaxID	non Hodgkins	III	lysate- GMCSF
Galena Biopharma	NeuVAX	breast cancer	III	Her2-GMCSF
Avax Technologies	AC Vaccine	melanoma	III	hapten-lysate
Generex Biotechnology	Ae-37	breast	II	Her2 peptide vaccine
Immatics biotechnologies	IMA901	renal	II	multi-peptide+ GMCSF
Scancell Holdings	SCIB1		II	plasmid
Merck	Stimuvax	lung, MUC-1	III	liposome
Prima BioMed LTD	Cvac	ovarian, MUC-1	III	mannan-fusion peptide

These nanoparticle vaccine platforms allow the ability to accommodate more than one protein simultaneously, i.e. isolated tumour antigens purified from a patient's biopsy, where the precise sequence and heterogeneous composition of the proteins remains unknown. With discovery of more widely prevalent malignant tumour associated peptides such as NY-ESO-1 (melanoma, breast, ovary and lung carcinomas) and MAGE-A3 (melanoma, non-small cell lung cancer, hematologic malignant tumours), we can vaccinate against a larger panel of malignancies. Identification of universal tumour antigens maybe advantageous to provide shelf ready vaccines. Reports have shown aberrant glycosylation is prevalent in cancer cells namely the Thomsen-Friedenreich antigen and Tn epitopes, typically shielded in normal cells are exposed in 90% of carcinomas [66]. Notably, cancer cells that have a high density of Tn over T epitopes have increased metastatic potential. Springer et al. ran a trial on 32 advance breast cancer patients (stages II-IV), who had undergone modified radical mastectomy/ lumpectomy and their first chemotherapy/ radiation therapy treatment. They were intradermally vaccinated with human O RBC derived T/Tn antigen in combination with $\text{Ca}_3(\text{PO}_4)_2$ and traces of typhoid vaccine and were able to demonstrate an increase in both five ($p < 10^{-7}$) and ten year ($p < 10^{-5}$) survival over NCI reported survival rates [67, 68]. It is well known that the gene product of MUC-1, epithelial membrane antigen (EMA), is heavily O-glycosylated and is selectively overexpressed in colon, breast, ovarian, lung and pancreatic cancers [69]. Since it is also expressed in the apical surface of normal epithelial cells in the lungs, stomach, intestine, eyes, and several other organs, for vaccine purposes, if one can generate eukaryotic MUC-1 antigens, in particular focusing on the

non-cleavable SEA domain [69], in combination with a knock-down of glycotransferase to emulate the production of T antigen in cancer, then upon vaccination, we would be able to mount a more effective humoral and cell mediated immune response towards cancerous MUC-1 phenotype over normal tissues.

Bibliography

1. WorldHealthOrganization, *Global Alliance for Vaccines and Immunization Factsheet*. World Health Organization. **Rep 169**: p. 2001.
2. Ehreth, J., *The global value of vaccination*. *Vaccine*, 2003. **21**(7-8): p. 596-600.
3. Hori, Y., et al., *Injectable dendritic cell-carrying alginate gels for immunization and immunotherapy*. *Biomaterials*, 2008. **29**(27): p. 3671-82.
4. Reddy, S.T., M.A. Swartz, and J.A. Hubbell, *Targeting dendritic cells with biomaterials: developing the next generation of vaccines*. *Trends in Immunology*, 2006. **27**(12): p. 573-579.
5. Fahmy, T.M., et al., *Design opportunities for actively targeted nanoparticle vaccines*. *Nanomedicine*, 2008. **3**(3): p. 343-355.
6. Tyagi, R.K., et al., *Various carrier system(s)- mediated genetic vaccination strategies against malaria*. *Expert Review of Vaccines*, 2008. **7**(4): p. 499-520.
7. Baba, T.W., et al., *Human neutralizing monoclonal antibodies of the IgG1 subtype protect against mucosal simian-human immunodeficiency virus infection*. *Nat Med*, 2000. **6**(2): p. 200-6.
8. Doeing, D.C., J.L. Borowicz, and E.T. Crockett, *Gender dimorphism in differential peripheral blood leukocyte counts in mice using cardiac, tail, foot, and saphenous vein puncture methods*. *BMC Clin Pathol*, 2003. **3**(1): p. 3.
9. Mestas, J. and C.C. Hughes, *Of mice and not men: differences between mouse and human immunology*. *J Immunol*, 2004. **172**(5): p. 2731-8.
10. Lim, K.H. and L.M. Staudt, *Toll-like receptor signaling*. *Cold Spring Harb Perspect Biol*, 2013. **5**(1): p. a011247.
11. Osamu Takeuchi, S.A., *Innate immunity to virus infection*. *Immunological Reviews*, 2009. **227**(1): p. 75-86.
12. Hamdy, S., et al., *Enhanced antigen-specific primary CD4+ and CD8+ responses by codelivery of ovalbumin and toll-like receptor ligand monophosphoryl lipid A in poly(D,L-lactic-co-glycolic acid) nanoparticles*. *J Biomed Mater Res A*, 2007. **81**(3): p. 652-62.
13. Hamdy, S., et al., *Co-delivery of cancer-associated antigen and Toll-like receptor 4 ligand in PLGA nanoparticles induces potent CD8+ T cell-mediated anti-tumor immunity*. *Vaccine*, 2008. **26**(39): p. 5046-5057.
14. Irache, J.M., et al., *Mannose-targeted systems for the delivery of therapeutics*. *Expert Opinion on Drug Delivery*, 2008. **5**(6): p. 703-724.
15. Jordan, M.B., et al., *Promotion of B cell immune responses via an alum-induced myeloid cell population*. *Science*, 2004. **304**(5678): p. 1808-10.
16. Lindblad, E.B., *Aluminium compounds for use in vaccines*. *Immunol Cell Biol*, 2004. **82**(5): p. 497-505.
17. Greenland, J.R. and N.L. Letvin, *Chemical adjuvants for plasmid DNA vaccines*. *Vaccine*, 2007. **25**(19): p. 3731-3741.
18. Aucouturier, J., L. Dupuis, and V. Ganne, *Adjuvants designed for veterinary and human vaccines*. *Vaccine*, 2001. **19**(17-19): p. 2666-2672.

19. Tuvim, M.J., et al., *Synergistic TLR2/6 and TLR9 activation protects mice against lethal influenza pneumonia*. PLoS One, 2012. **7**(1): p. e30596.
20. Peek, L.J., C.R. Middaugh, and C. Berkland, *Nanotechnology in vaccine delivery*. Advanced Drug Delivery Reviews, 2008. **60**(8): p. 915-928.
21. Singh, M., A. Chakrapani, and D. O'Hagan, *Nanoparticles and microparticles as vaccine-delivery systems*. Expert Review of Vaccines, 2007. **6**(5): p. 797-808.
22. Wang, X., et al., *Potent activation of antigen-specific T cells by antigen-loaded nanospheres*. Immunol Lett, 2005. **98**(1): p. 123-30.
23. Carbone, F.R. and M.J. Bevan, *Induction of ovalbumin-specific cytotoxic T cells by in vivo peptide immunization*. J Exp Med, 1989. **169**(3): p. 603-12.
24. Saupe, A., et al., *Immunostimulatory colloidal delivery systems for cancer vaccines*. Expert Opinion on Drug Delivery, 2006. **3**(3): p. 345-354.
25. Lemoine, D. and V. PrÉat, *Polymeric nanoparticles as delivery system for influenza virus glycoproteins*. Journal of Controlled Release, 1998. **54**(1): p. 15-27.
26. Mottram, P.L., et al., *Type 1 and 2 Immunity Following Vaccination Is Influenced by Nanoparticle Size: Formulation of a Model Vaccine for Respiratory Syncytial Virus*. Molecular Pharmaceutics, 2007. **4**(1): p. 73-84.
27. Kohane, D.S., *Microparticles and nanoparticles for drug delivery*. Biotechnol Bioeng, 2007. **96**(2): p. 203-9.
28. Mundargi, R.C., et al., *Nano/micro technologies for delivering macromolecular therapeutics using poly(d,l-lactide-co-glycolide) and its derivatives*. Journal of Controlled Release, 2008. **125**(3): p. 193-209.
29. Rĭhov, B., *Immunomodulating activities of soluble synthetic polymer-bound drugs*. Advanced Drug Delivery Reviews, 2002. **54**(5): p. 653-674.
30. Tracy, M.A., et al., *Factors affecting the degradation rate of poly(lactide-co-glycolide) microspheres in vivo and in vitro*. Biomaterials, 1999. **20**(11): p. 1057-62.
31. Gupta, R.K., et al., *Development of a Single-Dose Tetanus Toxoid Based on Controlled-Release from Biodegradable and Biocompatible Polyester Microspheres*. Vaccines93 : Modern Approaches to New Vaccines Including Prevention of Aids, 1993: p. 391-396.
32. Sanchez, A., et al., *Pulsed controlled-release system for potential use in vaccine delivery*. J Pharm Sci, 1996. **85**(6): p. 547-552.
33. Schwendeman, S.P., et al., *Strategies for stabilising tetanus toxoid towards the development of a single-dose tetanus vaccine*. New Approaches to Stabilisation of Vaccines Potency, 1996. **87**: p. 293-306.
34. Berry, C.C., *Intracellular delivery of nanoparticles via the HIV-1 tat peptide*. Nanomedicine, 2008. **3**(3): p. 357-365.
35. De Temmerman, M.L., et al., *Particulate vaccines: on the quest for optimal delivery and immune response*. Drug Discov Today, 2011. **16**(13-14): p. 569-82.
36. Gorden, K.B., et al., *Synthetic TLR agonists reveal functional differences between human TLR7 and TLR8*. J Immunol, 2005. **174**(3): p. 1259-68.

37. Hornung, V., et al., *Sequence-specific potent induction of IFN-alpha by short interfering RNA in plasmacytoid dendritic cells through TLR7*. Nat Med, 2005. **11**(3): p. 263-70.
38. Kariko, K., et al., *Suppression of RNA recognition by Toll-like receptors: the impact of nucleoside modification and the evolutionary origin of RNA*. Immunity, 2005. **23**(2): p. 165-75.
39. Tomai, M.A., and J. P. Vasilakos, *TLR-7 and -8 agonists as vaccine adjuvants*. Expert Rev. Vaccines, 2011. **10**: p. 405-407.
40. Von Andrian, U.H.e.a., *Nicotine Immunotherapeutics*. 2010. **USPTO 20100092425**.
41. Batista-Duharte, A., E.B. Lindblad, and E. Oviedo-Orta, *Progress in understanding adjuvant immunotoxicity mechanisms*. Toxicol Lett, 2011. **203**(2): p. 97-105.
42. Farokhzad, O.C., et al., *Targeted nanoparticle-aptamer bioconjugates for cancer chemotherapy in vivo*. Proc Natl Acad Sci U S A, 2006. **103**(16): p. 6315-20.
43. Petr O. Ilyinskii¹, Christopher J. Roy², Conlin P. O'Neil², Erica A. Browning², Lynnelle A. Pittet², David H. Altreuter², Frank Alexis^{3,7}, Elena Tonti^{4,8}, Jinjun Shi^{3,6}, Pamela A. Basto^{5,6}, Aleksandar F. Radovic-Moreno^{5,6}, Matteo Iannacone^{4,8}, Robert S. Langer^{5,6}, Omid C. Farokhzad³, Ulrich H. von Andrian⁴, Lloyd P.M. Johnston², and Takashi Kei Kishimoto, *Adjuvant-Carrying Synthetic Vaccine Particles Augment the Immune Response to Encapsulated Antigen and Exhibit Strong Local Immune Activation without Inducing Systemic Cytokine Release*. submitted.
44. Ivan Zanoni, R.O.F.G., *Generation of mouse bone marrow-derived dendritic cells* Protocol Exchange, 2009.
45. Heidenreich, P.A., et al., *Forecasting the future of cardiovascular disease in the United States: a policy statement from the American Heart Association*. Circulation, 2011. **123**(8): p. 933-44.
46. Butowski, P.F. and A.F. Winder, *Usual care dietary practice, achievement and implications for medication in the management of hypercholesterolaemia. Data from the U.K. Lipid Clinics Programme*. Eur Heart J, 1998. **19**(9): p. 1328-33.
47. Abifadel, M., et al., *Mutations in PCSK9 cause autosomal dominant hypercholesterolemia*. Nat Genet, 2003. **34**(2): p. 154-6.
48. Cohen, J.C., et al., *Sequence variations in PCSK9, low LDL, and protection against coronary heart disease*. N Engl J Med, 2006. **354**(12): p. 1264-72.
49. Zhang, D.W., et al., *Structural requirements for PCSK9-mediated degradation of the low-density lipoprotein receptor*. Proc Natl Acad Sci U S A, 2008. **105**(35): p. 13045-50.
50. Do, R.Q., R.A. Vogel, and G.G. Schwartz, *PCSK9 Inhibitors: potential in cardiovascular therapeutics*. Curr Cardiol Rep, 2013. **15**(3): p. 345.
51. Stein, E.A., et al., *Effect of a monoclonal antibody to PCSK9 on LDL cholesterol*. N Engl J Med, 2012. **366**(12): p. 1108-18.
52. McNutt, M.C., et al., *Antagonism of secreted PCSK9 increases low density lipoprotein receptor expression in HepG2 cells*. J Biol Chem, 2009. **284**(16): p. 10561-70.

53. Du, F., et al., *Novel domain interaction regulates secretion of proprotein convertase subtilisin/kexin type 9 (PCSK9) protein*. J Biol Chem, 2011. **286**(50): p. 43054-61.
54. Graham, M.J., et al., *Antisense inhibition of proprotein convertase subtilisin/kexin type 9 reduces serum LDL in hyperlipidemic mice*. J Lipid Res, 2007. **48**(4): p. 763-7.
55. Lindholm, M.W., et al., *PCSK9 LNA antisense oligonucleotides induce sustained reduction of LDL cholesterol in nonhuman primates*. Mol Ther, 2012. **20**(2): p. 376-81.
56. Frank-Kamenetsky, M., et al., *Therapeutic RNAi targeting PCSK9 acutely lowers plasma cholesterol in rodents and LDL cholesterol in nonhuman primates*. Proc Natl Acad Sci U S A, 2008. **105**(33): p. 11915-20.
57. Piper, D.E., et al., *The crystal structure of PCSK9: a regulator of plasma LDL-cholesterol*. Structure, 2007. **15**(5): p. 545-52.
58. Chan, J.C., et al., *A proprotein convertase subtilisin/kexin type 9 neutralizing antibody reduces serum cholesterol in mice and nonhuman primates*. Proc Natl Acad Sci U S A, 2009. **106**(24): p. 9820-5.
59. Jawien, J., P. Nastalek, and R. Korbut, *Mouse models of experimental atherosclerosis*. J Physiol Pharmacol, 2004. **55**(3): p. 503-17.
60. Carmeliet, P., L. Moons, and D. Collen, *Mouse models of angiogenesis, arterial stenosis, atherosclerosis and hemostasis*. Cardiovasc Res, 1998. **39**(1): p. 8-33.
61. Radovic-Moreno, A.F., et al., *Surface charge-switching polymeric nanoparticles for bacterial cell wall-targeted delivery of antibiotics*. ACS Nano, 2012. **6**(5): p. 4279-87.
62. Stary, G., *Nanoparticle-Based Vaccines*, Harvard, Editor 2013.
63. Radovic-Moreno, A., *Bacteria-Targeting Nanoparticles for Managing Infections*. 2013.
64. Schreiber, R.D., L.J. Old, and M.J. Smyth, *Cancer immunoediting: integrating immunity's roles in cancer suppression and promotion*. Science, 2011. **331**(6024): p. 1565-70.
65. Shankaran, V., et al., *IFN γ and lymphocytes prevent primary tumour development and shape tumour immunogenicity*. Nature, 2001. **410**(6832): p. 1107-11.
66. Springer, G.F., *Immunoreactive T and Tn epitopes in cancer diagnosis, prognosis, and immunotherapy*. J Mol Med (Berl), 1997. **75**(8): p. 594-602.
67. Springer, G.F., et al., *T/Tn Antigen Vaccine Is Effective and Safe in Preventing Recurrence of Advanced Breast-Carcinoma*. Cancer Detection and Prevention, 1995. **19**(4): p. 374-380.
68. Springer, G.F., et al., *T/Tn Antigen Vaccine Is Effective and Safe in Preventing Recurrence of Advanced Human Breast-Carcinoma*. Cancer Biotherapy, 1994. **9**(1): p. 7-15.
69. Pichinuk, E., et al., *Antibody targeting of cell-bound MUC1 SEA domain kills tumor cells*. Cancer Res, 2012. **72**(13): p. 3324-36.
70. Valencia, P.M., et al., *Single-step assembly of homogenous lipid-polymeric and lipid-quantum dot nanoparticles enabled by microfluidic rapid mixing*. ACS Nano, 2010. **4**(3): p. 1671-9.

Appendix

A1. PCSK9 Insert Sequences

A1.1 WT Sequence

ATGGGCACCGTCAGCTCCAGGCGGTCTGGTGGCCGCTGCCACTGCTGCT
GCTGCTGCTGCTGCTCCTGGGTCCCGCGGGCGCCCGTGCGCAGGAGGACGAG
GACGGCGACTACGAGGAGCTGGTGTAGCCTTGCGTTCCGAGGAGGACGGCC
TGGCCGAAGCACCCGAGCACGGAACCACAGCCACCTTCCACCGCTGCGCCAA
GGATCCGTGGAGGTTGCCTGGCACCTACGTGGTGGTGTGAAGGAGGAGACC
CACCTCTCGCAGTCAGAGCGCACTGCCCGCCGCTGCAGGCCAGGCTGCC
GCCGGGATACCTCACCAAGATCCTGCATGTCTTCCATGGCCTTCTTCTGGC
TTCCTGGTGAAGATGAGTGGCGACCTGCTGGAGCTGGCCTTGAAGTTGCCCC
ATGTCGACTACATCGAGGAGGACTCCTCTGTCTTTGCCAGAGCATCCCGTGG
AACCTGGAGCGGATTACCCCTCCACGGTACCGGGCGGATGAATACCAGCCCC
CCGACGGAGGCAGCCTGGTGGAGGTGTATCTCCTAGACACCAGCATAACAGAG
TGACCACCGGGAAATCGAGGGCAGGGTTCATGGTCCACCGACTTCGAGAATGTG
CCCGAGGAGGACGGGACCCGCTTCCACAGACAGGCCAGCAAGTGTGACAGT
CATGGCACCCACCTGGCAGGGGTGGTTCAGCGGCCGGGATGCCGGCGTGGCCA
AGGGTGCCAGCATGCGCAGCCTGCGCGTGTCAACTGCCAAGGGAAGGGCA
CGTTAGCGGCACCCTCATAGGCCTGGAGTTTATTTCGGAAAAGCCAGCTGGT
CCAGCCTGTGGGGCCACTGGTGGTGTGCTGCCCTGGCGGGTGGGTACAGC
CGCGTCTCAACGCCGCTGCCAGCGCCTGGCGAGGGCTGGGGTCTGTGCTGG
TCACCGCTGCCGGCAACTTCGGGACGATGCCTGCCTCTACTCCCCAGCCTCA
GCTCCCGAGGTCATCACAGTTGGGGCCACCAATGCCAGGACCAGCCGGTGA
CCCTGGGGACTTTGGGGACCAACTTTGGCCGCTGTGTGGACCTCTTTGCACCA
GGGGAGGACATCATTGGTGCCTCCAGCGACTGCAGCACCTGCTTTGTGGCAC
AGAGTGGGACATCACAGGCTGCTGCCACGTGGCTGGCATTGCAGCCATGAT
GCTGTCTGCCGAGCCGGAGCTCACCTGGCCGAGTTGAGGCAGAGACTGATC
CACTTCTCTGCCAAAGATGTCATCAATGAGGCCTGGTTCCCTGAGGACCAGC
GGTACTGACCCCCAACCTGGTGGCCGCCCTGCCCCCAGCACCCATGGGGC
AGGTTGGCAGCTGTTTTGCAGGACTGTGTGGTTCAGCACACTCGGGGCCTACA
CGGATGGCCACAGCCATCGCCCGCTGCGCCCCAGATGAGGAGCTGCTGAGCT
GCTCCAGTTTCTCCAGGAGTGGGAAGCGGGGGCGAGCGCATGGAGGCC
AAGGGGGCAAGCTGGTCTGCCGGGCCCACAACGCTTTTGGGGGTGAGGGTGT
CTACGCCATTGCCAGGTGCTGCCTGCTACCCAGGCCAACTGCAGCGTCCAC
ACAGCTCCACCAGCTGAGGCCAGCATGGGGACCCGTGTCCACTGCCACCAAC
AGGGCCACGTCCTCACAGGCTGCAGCTCCCACTGGGAGGTGGAGGACCTTGG
CACCCACAAGCCGCTGTGCTGAGGCCACGAGGTCAGCCCAACCAGTGCCTG

GGCCACAGGGAGGCCAGCATCCACGCTTCCTGCTGCCATGCCCCAGGTCTGG
AATGCAAAGTCAAGGAGCATGGAATCCCGGCCCTCAGGAGCAGGTGACCG
TGGCCTGCGAGGAGGGCTGGACCCTGACTGGCTGCAGTGCCCTCCCTGGGAC
CTCCACGTCCTGGGGGCCTACGCCGTAGACAACACGTGTGTAGTCAGGAGC
CGGGACGTCAGCACTACAGGCAGCACCAGCGAAGGGGGCCGTGACAGCCGTT
GCCATCTGCTGCCGGAGCCGGCACCTGGCGCAGGCCTCCCAGGAGCTCCAG

A1.2 PCSK9 Mutated sequence

ATGGGCACCGTCAGCTCCAGGCGGTCTGGTGGCCGCTGCCACTGCTGCT
GCTGCTGCTGCTGCTCCTGGGTCCCGCGGGCGCCCGTGCGCAGGAGGACGAG
GACGGCGACTACGAGGAGCTGGTGTAGCCTTGCGTTCGAGGAGGACGGCC
TGGCCGAAGCACCCGAGCACGGAACCACAGCCACCTTCCACCGCTGCGCCAA
GGATCCGTGGAGGTTGCCTGGCACCTACGTGGTGGTGTGAAGGAGGAGACC
CACCTCTCGCAGTCAGAGCGCACTGCCCGCCGCCTGCAGGCCCAGGCTGCC
GCCGGGGATACCTACCAAGATCCTGCATGTCTTCCATGGCCTTCTTCTGGC
TTCCTGGTGAAGATGAGTGGCGACCTGCTGGAGCTGGCCTTGAAGTTGCCCC
ATGTCGACTACATCGAGGAGGACTCCTCTGTCTTTGCCAGAGCATCCCGTGG
AACCTGGAGCGGATTACCCCTCCACGGTACCGGGCGGATGAATACCAGCCCC
CCGACGGAGGCAGCCTGGTGGAGGTGTATCTCCTAGACACCAGCATAACAGAG
TGACCACCGGGAAATCGAGGGCAGGGTTCATGGTTCACCGACTTCGAGAATGTG
CCCGAGGAGGACGGGACCCGCTTCCACAGACAGGCCAGCAAGTGTGACAGT
CATGGCACCCACCTGGCAGGGGTGGTTCAGCGGCCGGGATGCCGGCGTGGCCA
AGGGTGCCAGCATGCGCAGCCTGCGCGTGTCAACTGCCAAGGGAAGGGCA
CGTTAGCGGCACCCTCATAGGCCTGGAGTTTATTTCGGAAAAGCCAGCTGGT
CCAGCCTGTGGGGCCACTGGTGGTGTGCTGCTGCCCTGGCGGGTGGGTACAGC
CGCGTCTCAACGCCGCCTGCCAGCGCCTGGCGAGGGCTGGGGTCTGTGCTGG
TACCCTGCGCGCAACTTCGGGACGATGCCTGCCTCTACTCCCCAGCCTCA
GCTCCCGAGGTCATCACAGTTGGGGCCACCAATGCCAGGACCAGCCGGTGA
CCCTGGGGACTTTGGGGACCAACTTTGGCCGCTGTGTGGACCTCTTTGCACCA
GGGGAGGACATCATTGGTGCCTCCAGCTACTGCAGCACCTGCTTTGTGGCAC
AGAGTGGGACATCACAGGCTGCTGCCACGTGGCTGGCATTGCAGCCATGAT
GCTGTCTGCCGAGCCGGAGCTCACCTGGCCGAGTTGAGGCAGAGACTGATC
CACTTCTTGCCAAAGATGTCATCAATGAGGCCTGGTTCCCTGAGGACCAGC
GGTACTGACCCCCAACCTGGTGGCCGCCCTGCCCCCAGCACCCATGGGGC
AGGTTGGCAGCTGTTTTGCAGGACTGTGTGGTTCAGCACACTCGGGGCCTACA
CGGATGGCCACAGCCATCGCCCCGCTGCGCCCCAGATGAGGAGCTGCTGAGCT
GCTCCAGTTTCTCCAGGAGTGGGAAGCGGCGGGGCGAGCGCATGGAGGCC
AAGGGGGCAAGCTGGTCTGCCGGGCCACAACGCTTTTGGGGGTGAGGGTGT
CTACGCCATTGCCAGGTGCTGCCTGCTACCCAGGCCAACTGCAGCGTCCAC
ACAGCTCCACCAGCTGAGGCCAGCATGGGGACCCGTGTCCACTGCCACCAAC
AGGGCCACGTCCTCACAGGCTGCAGCTCCCACTGGGAGGTGGAGGACCTTGG
CACCCACAAGCCGCCTGTGCTGAGGCCACGAGGTCAGCCCAACCAGTGCCTG
GGCCACAGGGAGGCCAGCATCCACGCTTCCTGCTGCCATGCCCCAGGTCTGG
AATGCAAAGTCAAGGAGCATGGAATCCCGGCCCTCAGGAGCAGGTGACCG
TGGCCTGCGAGGAGGGCTGGACCCTGACTGGCTGCAGTGCCCTCCCTGGGAC

CTCCCACGTCCTGGGGGCCTACGCCGTAGACAACACGTGTGTAGTCAGGAGC
CGGGACGTCAGCACTACAGGCAGCACCAGCGAAGGGGCCGTGACAGCCGTT
GCCATCTGCTGCCGGAGCCGGCACCTGGCGCAGGCCTCCCAGGAGCTCCAG

A2. HER-2-Targeted Nanoparticle–Affibody Bioconjugates for Cancer Therapy*

*** This work is published and copyrighted by ChemMedChem**

Frank Alexis,[a, b] Pamela Basto,[a, b] Etgar Levy-Nissenbaum,[a, b] Aleksandar F. Radovic-Moreno,[b] Liangfang Zhang,[b] Eric Pridgen,[c] Andrew Z. Wang,[b, d] Shawn L. Marein,[a] Katrina Westerhof,[a, b], Linda K. Molnar,[e] and Omid C. Farokhzad*[a, b]. ChemMedChem 2008, 3, 1839 – 1843.

Drug encapsulated controlled release nanoparticles (NPs) have the potential to improve the current cancer chemotherapies by increasing drug efficacy, lowering drug toxicity, and maintaining a relatively high concentration of drug at the site of interest [1-3]. Encapsulating drugs within NPs can improve the solubility and pharmacokinetics of drugs, and, in some cases, enable the further clinical development of new chemical entities that have stalled because of poor pharmacokinetic properties. The breakthrough potential of cancer nanotechnology is becoming more apparent with several examples of non-targeted NP platforms in clinical practice today. These include Abraxane (paclitaxol-albumin) [4], Doxil (doxorubicin-liposomes) [5], DaunoXome (daunorubicin-liposomes)[6], Cycloset (camptothecin-cyclodextrin) [7] and Genexol-PM [paclitaxolmethoxy-polyethyleneglycol-poly(D,L-Lactide)] [8]. The functionalization of non-targeted NPs with ligands that bind to the extracellular domain of tumor-associated trans-membrane antigens may further increase the therapeutic index of cytotoxic drugs by differentially targeting drugs to the diseases cells.

The first examples of targeted nanoparticles were reported in 1980 and despite nearly 3 decades of research, targeted nanoparticles have made a limited impact on human health. This is in part because the optimal biophysicochemical properties of the nanoparticles, including the choice of a suitable ligand for targeting has remained elusive [9-11]. These include the utilization of targeting approaches that go beyond antibodies which have several known drawbacks including their large hydrodynamic size which limits both intratumoral uptake and homogeneous distribution in the tumor adversely affecting pharmacokinetic properties. Further, the use of an antibody as a component of a multifunctional nanoparticle adds an additional level of complexity to the scale-up and manufacturing of the resultant targeted nanoparticles. There is a clear need for new methods of targeting that are compatible with the size of nanoparticles and their manufacturing. Additionally, while monoclonal antibodies have shown some promise their effects tend to be variable and ultimately not curative. Attempts to develop immunoconjugates, which add the therapeutic benefit of a drug, toxin, or radionuclide, have not met with much success either probably due to low drug content per antibody molecule. However, the combination of the targeting capabilities of an antibody, without

the inherent limitations of antibodies [12] as mentioned above, and a controlled release system utilizing a payload consisting of a small molecule chemotherapeutic may prove to be advantageous.

The anti-HER-2 Affibody has many merits as a targeting ligand in contrast to an anti-HER-2 monoclonal antibody. Its small size (Molecular weight ~ 15 kDa) results in a favorable ratio of binding site to ligand size, bearing in mind that the molecular weight of an anti-HER-2 monoclonal antibody is typically about 150 kDa; it promotes an endocytosis dependent internalization mechanism [13-16]; it has a functional end group distanced from its active site for chemical conjugation; it has high *in vitro* and *in vivo* stability; and the total chemical synthesis allows facile large scale production of the Affibody. The anti-HER-2 Affibody (Z-HER2: 342 Affibody) has shown high binding affinity ($K_D \sim 22$ pM) to the recombinant extracellular domain of the protein HER-2 (HER-2-ECD) [17, 18]. In addition, Orlova et al. [17] has shown that this class of molecules can selectively bind to HER-2 over-expressing cell lines (SK-BR-3 and SK-OV-3). All of these characteristics make Affibody a potentially viable ligand for targeted drug delivery.

To develop HER-2 targeted drug encapsulated NPs, we conjugated the anti-HER-2 Affibody to the thiol-reactive maleimide of the PLA-PEG-Maleimide (PLA-PEG-Mal) copolymer of the previously formed NPs through a stable thioether bond and evaluated the targeting specificity and efficacy using fluorescent microscopy. Subsequently, we encapsulated paclitaxel into the targeted polymeric NPs and examined whether this system could increase the drug cytotoxicity in HER-2 positive cell lines: SK-BR-3 and SK-OV-3. We chose to deliver the taxane paclitaxel due to its poor water solubility which results in a reduced therapeutic index for intravenous administration of the free drug in a clinical setting.

We first synthesized a copolymer comprised of a hydrophobic block, poly (D,L lactic acid), and a hydrophilic block, poly(ethylene glycol) with a maleimide terminal group (PLA-PEG-Mal). Then the copolymers form negatively charged NPs with a core-shell structure in an aqueous environment via the nanoprecipitation method. The hydrophobic core of the NPs is capable of carrying pharmaceuticals, especially those with poor water solubility. The hydrophilic shell not only provides a “stealth” layer [19], together with the surface charge property (Zeta potential) = -10 mV \pm 5 mV [20, 21], to improve the stability and the circulation half-time of these drug delivering NPs, but also functional maleimide groups for Affibody conjugation (Figure 1A). Lack of protein adsorption in solutions including 10%, 20% and 100% serum (data not shown) demonstrated the stability of NP size (< 100 nm). We also evaluated the freeze-drying process for storing the nanoparticles in a dry state, as described previously [22]. We were able to reconstitute nanoparticles with a similar original size after lyophilization, confirming the stability of this type of carrier to this process.

The anti-HER-2 Affibody molecule was previously selected against the extracellular domain of the HER-2 protein [23] and further modified by affinity maturation and dimerization [14, 18]. The anti-HER-2 Affibody is commercially available and has been shown to have high binding specificity and affinity *in vitro* and *in vivo* as a targeted imaging agent [17, 24-26]. Therefore, the multiple advantages of the combination of biodegradable polymeric NPs and targeting anti-HER-2 Affibody molecules led to our interest in developing a a targeted, controlled release drug delivery system for cancer

therapy aimed at HER-2 positive cells. Particle size and surface charge (Zeta potential) of PLA-PEG-Mal NPs both with and without Affibody were characterized using laser light scattering, ZetaPALS system and electron microscopy (Figure 1A). The addition of Affibody molecules on the surface of the NPs did not significantly affect the size, size distribution and surface charge of the NPs (NP = 70 ± 5 nm, NP-Affibody 85 ± 5 nm). The chemical conjugation of the Affibody molecules on the surface of the PLA-PEG-Mal NPs was confirmed using UV imaging (Figure 1A) and proton nuclear magnetic resonance spectroscopy in d-DMSO ($^1\text{H-NMR}$) (Figure 1B). To visualize the presence of Affibody molecules on the NPs, we labeled Affibody molecules with the fluorescence probe, Alexa Fluor 532, and subsequently conjugated them to the PLA-PEG-Mal NPs with different molar ratios of Affibody:PLA-PEG-Mal (0, 1, 2, 5, 20%). The NP-Affibody bioconjugates were then exposed under UV lamp to observe their fluorescence signals. As shown in Figure 1B, no fluorescence signal was observed from the NPs without fluorescently labeled Affibody, however, the fluorescence intensity from those NPs with fluorescent Affibody continuously enhances with the increase of Affibody:PLA-PEG-Mal molar ratio. The $^1\text{H-NMR}$ spectrum of the purified PLA-PEG-Affibody in d-DMSO showed the characteristic peaks of PLA-PEG at chemical shift of $\delta \sim 1.4$ ppm ($-\text{CH}_3$ of the PLA backbone), $\delta \sim 3.6$ ppm of ($-\text{CH}_2$ of the PEG backbone) and $\delta \sim 5.2$ ppm ($-\text{CH}$ of the PLA backbone) (Figure 1B). Additionally, we observed the characteristic peaks of the Affibody molecule in the chemical shift region of $\delta = 7-8$ ppm that represents the amide bonds (NH-CO) within the Affibody polypeptide molecule. The NMR results suggest successful conjugation of the Affibody on the surface of PLA-PEG-Mal NPs.

We next demonstrated the efficient binding and internalization of targeted NP-Affibody bioconjugates to HER-2 positive cancer cells using three cell lines: Capan-1 (Figure 2-B1), SK-BR-3 (Figure 2-B2), and SK-OV-3 (Figure 2-B3). After incubating NBD dye encapsulated NP-Affibody bioconjugates with the cells for 2 hr at 37°C and removing the excess bioconjugates, we observed a large amount of green dots in a punctuate pattern inside the targeted cells, suggesting an efficient targeting and internalization mechanism of the ~ 80 nm NP-Affibody bioconjugates to the HER-2 positive cells. In contrast, untargeted PLA-PEG NPs were slightly taken up by the cell lines after the same duration of incubation (Figure 2 A1-A3). To minimize cell passage effect on the observed results, this experiment was repeated four times with different cell passages and all of them gave the same observations. We also verified the cellular localization of the NP-Affibody bioconjugates using a z-axis scanning fluorescent microscopy and 3D image reconstitution. The rotated cross section of the 3D reconstitution images of a SK-BR-3 cell demonstrated the internalization of targeted NP-Affibody bioconjugates to the cell (Figure 3).

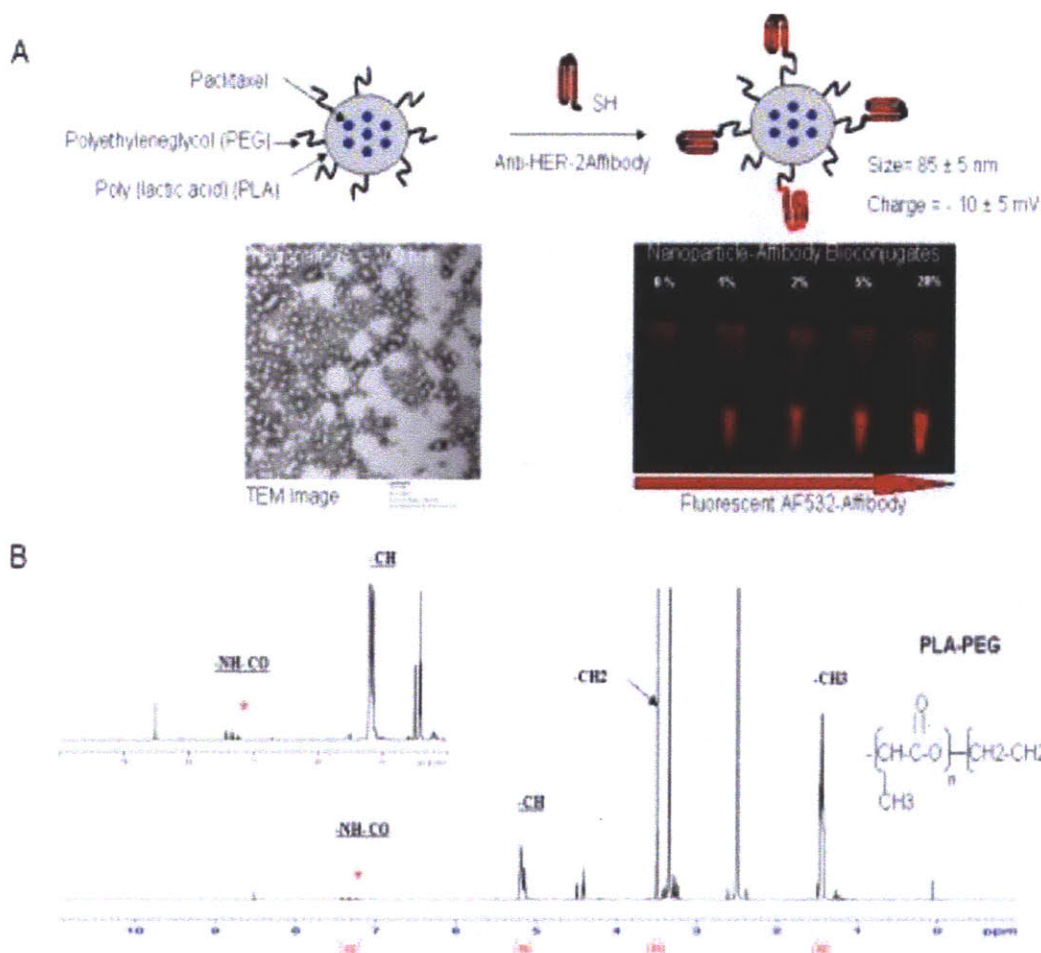


Figure A1.1. Schematic diagram of the formation of drug encapsulated PLA-PEG-Mal nanoparticle-Affibody bioconjugates. Nanoparticle's size diameter (< 100 nm) and distribution was visualized by electron microscopy. The hydrophilic polyethyleneglycol (PEG) chains on the surface reduce the protein absorption on the hydrophobic polymeric surface to form “stealth” nanoparticles. Direct visualization of Affibody conjugation on the surface of the nanoparticle was carried out using fluorescent image of fluorescent Affibody (Alexa Fluor 532; red) conjugated to nanoparticles. After washing the nanoparticle-Affibody bioconjugates, the fluorescent signal increases with an increased amount of fluorescent Affibody (0-20 % Affibody/polymer molar ratio) on the nanoparticle surface confirming the chemical conjugation efficiency. B) $^1\text{H-NMR}$ (proton nuclear magnetic resonance) spectrum represents the PLA-PEG-Affibody bioconjugates. The $^1\text{H-NMR}$ spectrum shows the protons assigned to the polymer ($\delta = 1-6$ ppm) and the presence of Affibody polypeptide ($\delta = 7-8$ ppm) confirming the chemical conjugation of the Affibody on the polymeric nanoparticles.

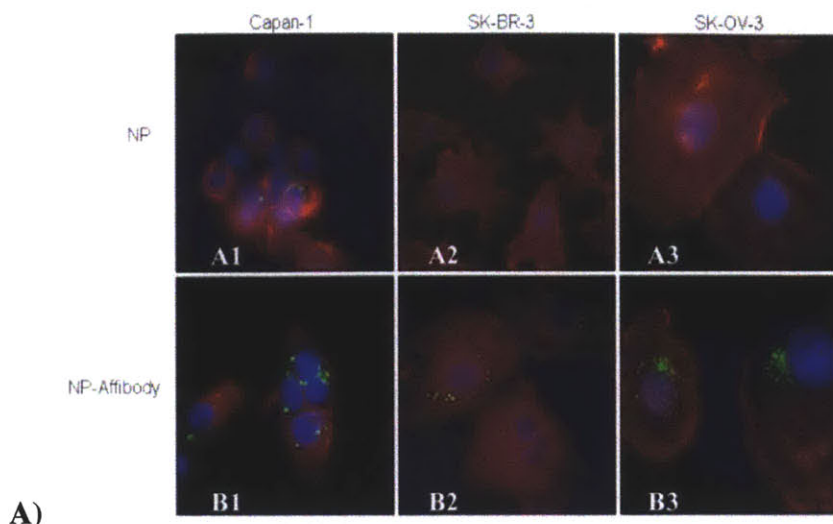


Figure A1.2 Fluorescent microscopy of nanoparticle-Affibody bioconjugates incubated with HER-2 positive cell lines. Capan-1 cells, SK-BR-3 cells and SK-OV-3 cells were grown on chamber slides and incubated in OptiMEM medium supplemented with $5 \mu\text{g}$ of NBD fluorescent dye encapsulated into nanoparticles shown in green with (upper panel) or targeted nanoparticle-Affibody bioconjugates (lower panel) for 2 hours prior imaging using fluorescent microscopy at 60X magnification. The cell nuclei and the actin cytoskeleton are stained with *blue* (4',6-diamidino-2-phenylindole) and *red* (Alexa-Flour Phalloidin-488), respectively. The deconvoluted fluorescent images represent the mid-cross section of the cells after washing (3 times), permeabilizing and staining steps.

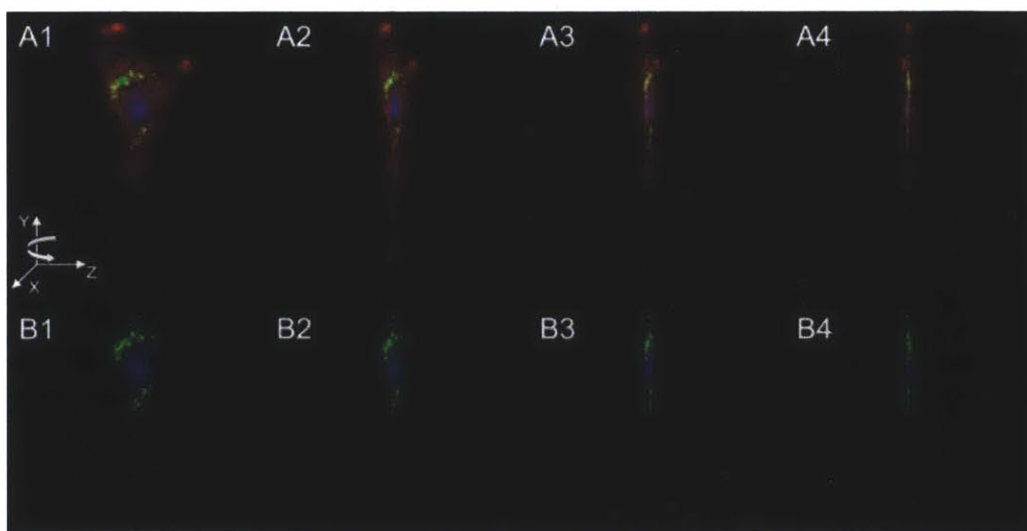


Figure A1.3 Combined fluorescent images (60X magnification) of a single SK-BR-3 cell to reconstruct a three-dimensional image of the cell. A1-A4 (upper panel) images represent the mid-cross section images of the same SK-BR-3 cell being rotated at 30-degree intervals along the y- axis. A4 represents an image of SK-BR-3 rotated to 90-degree along the y-axis demonstrating particles shown in *green* (NBD fluorescent dye encapsulated into the nanoparticles) internalized inside the cell. The

cell nuclei and the actin cytoskeleton are stained with *blue* (4',6-diamidino-2-phenylindole) and *red* (Alexa-Fluor Phalloidin-488), respectively. B1-B4 (lower panel) represents fluorescent images of the same SK-BR-3 (shown in the upper panel) cell without the actin cytoskeleton staining confirming the internalization of the nanoparticle-Affibody bioconjugates inside the cell.

Orlova et al. [18] have shown the binding ability of Anti-HER-2 Affibody within 1 hr using immunofluorescence method. Our results are consistent with their findings and suggest a receptor mediated endocytosis mechanism. Internalization through an endocytosis mechanism has been previously described for anti-HER-2 monoclonal antibodies [27, 28] and is consistent with the kinetics of our targeted NPs entering the cells within 2 hours. Similarly, targeted drug delivery using RGD peptide sequences to integrins has also shown efficient binding and internalization in multiple types of cancers. In addition to efficient binding and internalization, the anti-HER-2 approach also offers improved cancer disease specificity with high affinity to HER-2 cell membrane receptors expressed in multiple types of cancers compared to RGD [29]. We prepared drug-containing and drug free Nps and targeted nanoparticles to evaluate their differential cytotoxicity using in vitro cell viability assay (MTS assays) with breast cancer and ovarian cancer cells (SK-BR-3; SK-OV-3), which over-express the HER-2 cell membrane receptors. In this study, we incubated various NP formulations with SK-BR-3 and SK-OV-3 cancer cells for 2 hours in optimum, washed cells with PBS to remove excess of NPs, and supplemented with fresh cell growth medium. We further incubated the cells for 3 days before using the MTS assay to quantify cell viability which was normalized to that of the cells in the absence of NPs.

The results showed that drug encapsulated targeted NPs had the highest cytotoxicity to both SK-BR-3 and SK-OV-3 cell lines; cell viability was $70 \pm 5 \%$ and $59 \pm 5 \%$, respectively (Figure 4). The ANOVA test indicated that the cell viability of drug containing targeted NPs differed significantly from that of drug containing NPs ($p < 0.05$). In contrast, free drug and NPs without encapsulated drugs are not toxic to both cell lines. These results are consistent with our previous studies using targeted NP-aptamer bioconjugates to deliver drugs to prostate cancer cells [30-33]. Therefore, this NP-Affibody bioconjugate system holds potential to be used as a biocompatible and biodegradable targeted drug delivery platform for multiple types of cancer therapeutics. Further, the modularity of the delivery system allows for tuning of the various parameters of the bioconjugates, such as NP size, surface charge and Affibody packing density, in order to optimize the drug delivery pharmacokinetics and its targeting efficiency for optimum specific therapeutic applications.

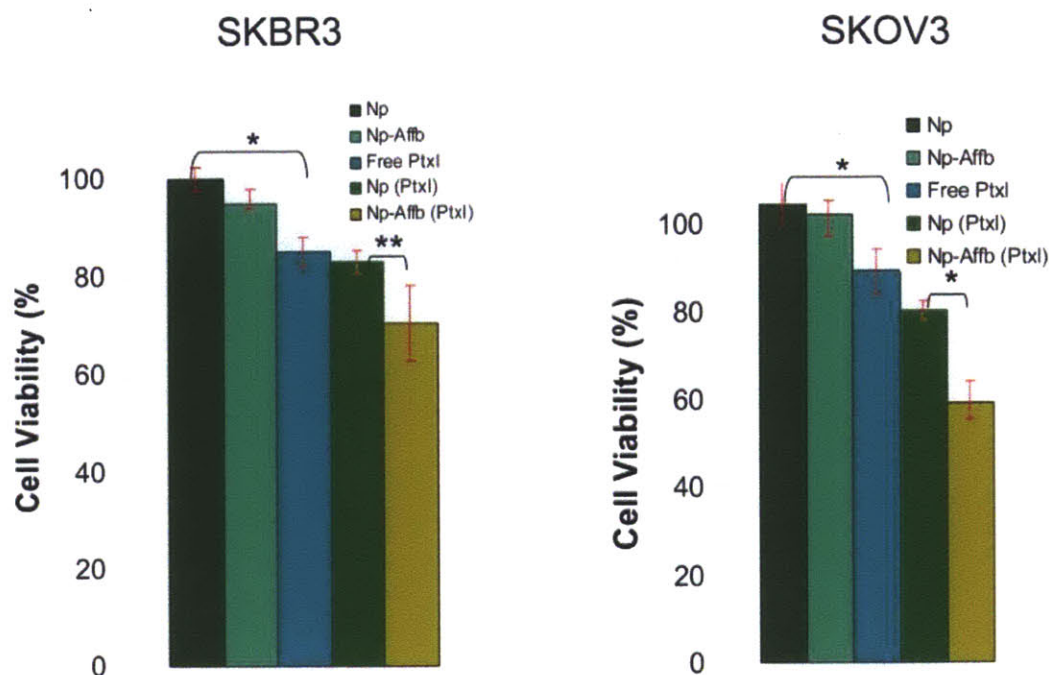


Figure A1.4. Cell viability assay (MTS assay) to evaluate the differential toxicity of targeted (Np-Affb) and untargeted nanoparticles (Np) with and without encapsulated paclitaxel (Ptxl). In this assay, the nanoparticle formulations were incubated for 2 hours, cells were subsequently washed and incubated in cell growth media to allow the effect of the drug on the cell cycles before quantifying the nanoparticle formulations toxicities against two cancer cell lines expressing HER-2 (SK-BR-3 and SK-OV-3). ANOVA test “*” p<0.01; “” p<0.05.**

In summary, herein we report to our knowledge the first example of a targeted controlled release NP-Affibody bioconjugate for drug delivery to HER-2 positive cancer cells. Using FDA (Food Drug and Administration) approved polymers to form nanoparticles, we have demonstrated that the nanoparticle-Affibody bioconjugates were specifically and efficiently internalized to HER-2 positive cancer cells such as ovarian, breast and pancreatic cancer cells, thereby providing a promising way to deliver chemotherapeutic drugs to the cancer cells in a selective manner. This HER-2 targeted drug delivery platform can be tuned to encapsulate multiple types and combinations of drugs, increase drug loading, and optimize the surface coverage of the Affibody targeting ligands for specific therapeutic applications. Additional *in vivo* biodistribution and efficacy studies are needed to further evaluate the potential of the nanoparticle-Affibody bioconjugates for each therapeutic application as a systemic or locally administered drug delivery system.

Methods:

Size (diameter) and Zeta-potential (surface charge) of NPs were evaluated by Quasi-elastic laser light scattering (QELS) using a ZetaPALS dynamic light-scattering detector (15 mW laser, incident beam = 676 nm; Brookhaven Instruments, Holtsville, NY). 200 µg of nanoparticles were dispersed in solution (~2ml) and measurements were performed in triplicate at room temperature.

Conjugation and Characterization of nanoparticle-Affibody bioconjugates

PLA-PEG-Mal polymeric NPs were incubated under stirring conditions with the Anti-HER-2 Affibody molecules (15kDa) at a molar ratio of Affibody:PLA-PEG-Mal of 5 % to form a stable bioconjugate. The NP-Affibody bioconjugates were purified to remove free Affibody molecules using Amicon Ultra centrifuge device (100 kDa molecular weight size exclusion). Subsequently, the thioether bond formation between the PLA-PEG-Mal NPs and the Affibody molecules was characterized using proton nuclear magnetic resonance (¹H-NMR, 600 MHz, Bruker Advance). Additionally, the chemical attachment of the fluorescent Affibody was confirmed using an Ultra Violet Imaging system (Kodak Electrophoresis Documentation and Analysis System 120). The Affibody molecule was fluorescently labeled with a red fluorescent probe, Alexa Fluor 532 (Invitrogen), purified and subsequently conjugated to PLA-PEG-Mal polymeric NPs at different molar ratios of Affibody:PLA-PEG-Mal ranging from 0 to 20 % (molar ratio). Then the purified NP-Affibody bioconjugate suspensions were imaged using a UV Kodak camera assisted with a red filter to show the visible effect of the fluorescent Affibody conjugated on non-fluorescent polymeric NPs.

Uptake assays of targeted and untargeted nanoparticles

The human ovarian adenocarcinoma (SK-OV-3; ATCC), human breast adenocarcinoma (SK-BR-3; ATCC), and human pancreatic adenocarcinoma (Capan-1, ATCC) were the HER-2 positive cell lines used for cytotoxicity and uptake efficacy studies of the NP-Affibody bioconjugates. HER-2 positive cell lines were grown in chamber slides (Cab-TekII, 8 wells; Nunc) within their growth medium (Modified McCoy's 5a (ATCC) supplemented with 100 units/ml aqueous penicillin G, 100 ug/ml streptomycin, and 10% FBS) to 70% confluence in 24 h (i.e., 50,000 cells/cm²) in 5 % CO₂ incubator. On the day of the experiment, cells were washed with pre-warmed PBS and incubated with pre-warmed phenol-red–reduced OptiMEM media for 30 minutes, before adding 50 µg of NPs or NP-Affibody bioconjugates loaded with same amount of green fluorescent NBD dye (4-fluoro-7-nitrobenz-2-oxa-1,3-diazole). NP formulations were incubated with cells for 2 hours at 37°C, washed with PBS three times, fixed with 4% paraformaldehyde, blocked for 30 minutes at room temperature with 1 % BSA/PBS, permeabilized with 0.01 % Triton-X for 3 minutes, counterstained with Alexa-Fluor Phalloidin-Rhodamine (cytoskeleton staining), 4',6-diamidino-2-phenylindole (DAPI, nucleus staining), mounted in fluorescence protecting imaging solution, and visualized using fluorescent microscopy (DeltaVision system; Olympus IX71). Digital images of green, red and blue fluorescence were acquired along the z-axis at 0.2 µm intervals using 60X oil immersion objective and DAPI, FITC and Rhodamine filters respectively. Images were overlaid, deconvoluted and 3D reconstruction was performed using Softwork software for acquisition and analysis.

In vitro cellular toxicity assay of paclitaxel encapsulated into targeted and untargeted NPs

SK-BR-3 and SK-OV-3 were grown in 96-well plates at concentrations leading to 70% confluence in 24 h (i.e. 50,000 cells/cm²). Defined amounts of paclitaxel were encapsulated into targeted and non-targeted nanoparticles (1 % wt/wt) and incubated with

cell lines (5 ug Paclitaxel/well) in OptiMEM for two hours. Next, cells were washed and fresh media was supplemented. The cells were then allowed to grow for 72 hours and cell viability was assessed colorimetrically with MTS reagents (Invitrogen).

A2. Single-Step Assembly of Homogenous Lipid-Polymeric and Lipid-Quantum Dot Nanoparticles Enabled by Microfluidic Rapid Mixing**

**Reproduced with permission from Valencia, P.M., et al., Single-step assembly of homogenous lipid-polymeric and lipid-quantum dot nanoparticles enabled by microfluidic rapid mixing. *ACS Nano*, 2010. 4(3): p. 1671-9. Copyright 2008. American Chemical Society. [70]

The development of smart multifunctional targeted nanoparticles (NPs) that can deliver drugs at a sustained rate to specific cells and carry nanoscale imaging agents may provide better efficacy, lower toxicity, and enhanced prognosis for treatment of multiple diseases¹⁻⁴. Two promising families of NPs that can encapsulate and deliver therapeutic agents are polymeric NPs and liposomes.^{1, 2} Biocompatibility, biodegradability, reduced toxicity, and capacity for size and surface manipulations are benefits that these NPs offer in comparison to other delivery systems. Recently, it has been shown that hybrid lipid-polymeric NPs combine the desirable characteristics of polymeric NPs and liposomes such as high drug encapsulation yield, slow drug release, and high serum stability.^{3, 4} In addition, temporal controlled release of two different therapeutic agents has been achieved with these hybrid NPs by entrapping one agent in the lipid envelope and the other one in the polymeric core.⁵

The development of novel nanosystems such as hybrid lipid-polymeric NPs for drug delivery is necessary to advance the frontiers of drug delivery, but the ability to precisely control and predict properties of these systems is critical for their success in clinical translation.⁶ Furthermore, it may be necessary to screen and select NPs with optimal properties for a certain application, which demands reproducible synthesis of NPs with distinct size, charge, and ligand density.⁷ Among some of the technologies developed to prepare polymeric and lipid NPs of well-defined properties, continuous-flow microfluidic synthesis offers better control over NP formation compared to conventional synthesis and has the potential to tune NP characteristics in a reproducible manner, which is critical for identifying optimal NP formulations for any given application.⁸⁻¹¹ Continuous-flow microfluidics has been used to synthesize polymeric nano and microparticles using controlled emulsification.¹² and droplet formation through hydrodynamic flow focusing.^{13, 14} Recently, hydrodynamic flow focusing was used for the synthesis of liposomes with sizes of less than 200 nm^{15, 16}, and PLGA-PEG NPs by nanoprecipitation (also known as solvent-displacement method).⁹

However, conventional methods for synthesizing lipid-polymeric NPs are more complex as compared to the preparation of liposomes or polymeric NPs. These methods involve mixing of polymeric NPs with liposomes to form lipid-polymer complexes, in which a lipid bilayer or lipid multilayer fuses on the surface of polymeric NPs.¹⁷⁻¹⁹

These complexes usually require a two-step formulation process: (i) development of polymeric NPs, and (ii) encapsulation of polymeric NPs within liposomes, resulting in poor control over the final NP physicochemical structure. Recently, our group developed a single step bulk hybrid lipid NP preparation in which a solution of poly-(lactic-co-glycolic) acid (PLGA) in acetonitrile was added to an aqueous solution of lecithin and 1,2-distearoyl-*sn*-glycero-3-phosphoethanolamine-N-[carboxy(polyethylene glycol)] (DSPE-PEG) resulting in the formation of hybrid lipid-polymeric NPs.^{3, 4} Although this preparation yields sub-100 nm NPs and simplifies the synthesis, intermediate steps such as heating, vortexing, and long incubation time does not make the process easily amenable to combinatorial synthesis and can introduce variability in the properties of the NPs. A single-step process for reproducible synthesis of hybrid lipid-polymer NPs would enable preparation of libraries of NPs with distinct properties and allow for identification of optimal NP properties for different applications.

In this work, we show that rapid mixing of polymer and lipid solutions using continuous-flow microfluidics results in core-shell lipid-polymeric NPs in a single-step nanoprecipitation process. These NPs are composed of PLGA, lecithin and DSPE-PEG. We investigated the conditions under which stable hybrid NPs were formed and showed that by simply changing the precursors, NPs with tunable size from 35–180 nm and tunable zeta potential from -20 to 10 mV in PBS could be synthesized. Using the same microfluidic platform, we prepared homogenous lipid-QD NPs composed of CdSe/ZnS QDs coated by a lecithin and DSPE-PEG layer for potential imaging applications. Simplicity and reproducibility make this technology suitable for the combinatorial synthesis and screening of NPs with different properties without resorting to labor-intensive processing.

Results and Discussions

Controlled nanoprecipitation of NPs can be obtained by minimizing the mixing time to ensure homogeneous environment for nucleation and growth of the NPs.²⁰ One way to decrease mixing time in microchannels is the use of micromixing structures, such as serpentine, staggered-herringbone, and zig-zag structures.²¹ Here we used an in-plane micromixing structure called Tesla mixer²² that operates at Reynolds numbers greater than 20. These micromixing structures show contributions from both diffusion and convection at high flow rates.

Figure 1a shows a schematic of the microchannel used to synthesize the hybrid lipid-polymeric NPs. An aqueous solution composed of lecithin and DSPE-PEG (lecithin:DSPE-PEG, 8.4:1.6 by mol) was mixed with an organic solution of PLGA dissolved in acetonitrile (1 mg/mL) at a volume ratio of 10:1. At the junction of the streams, the organic stream is hydrodynamically focused and enhanced mixing occurs through the Tesla structures as the focused streams flows along the channel. The hybrid NPs generated have PLGA-lecithin-PEG core-shell structure and properties as those previously synthesized using bulk synthesis methods (Figure 1b)^{3, 4}. TEM imaging allowed qualitative assessment of the product stream including its core-shell structure and monodispersity (Figure 1c). The average NP size is 40 nm and its size distribution by volume indicated that over 85% of the NPs have a size within 30–60 nm (Figure 1d). A fluorescent dye was used to observe the unfolding-folding flow pattern inside the

micromixer and used to illustrate the degree of mixing within the channel (Figure 1e). From this image, observation of complete mixing at a total flow rate of 50 $\mu\text{L}/\text{min}$ occurs within the fourth turn of the Tesla mixer on a timescale of 10 ms (see [supporting information](#) for determination of mixing timescale in microchannel). This flow rate was fast enough to ensure good mixing in the Tesla mixer, yet low enough to limit the pressure drop in the device and hence prevent device failure.

Characterization of PLGA-lipid NPs

The overall structure of the NPs synthesized was tested by multiple measures to ensure that they were hybrid particles of both lipid and polymeric nature rather than a combination of liposomes and unprotected PLGA NPs. Using different components in the input stream such as polymer alone, lipid/ lipid-PEG alone, or a combination of both illustrated differences in size of particles generated through the Tesla mixer (Figure 2a). When only polymer was present, NPs formed with a size of 40–50 nm and experienced slow aggregation within a few hours of formation, resulting in sizes ranging from 50–100 nm. When only lipid and lipid-PEG were added in the input streams, NPs obtained had a much larger size (~250 nm) and wider size distribution, which is typical for liposomes. However, particles prepared with both polymer and lipid had a size of 40 nm that did not significantly change over a long period of time (see [figure S2](#), supporting information) This difference in size suggests that when both polymer and lipid are present in the input streams, polymeric NPs formed are stabilized by a lipid coating that helps maintain a size of 40 nm. Moreover, NPs generated with varying flow ratios of aqueous to organic stream did not appear to have a significant influence on the NP size (Figure 2a).

To investigate the optimal amount of lipid needed to obtain a stable hybrid NP that do not experience aggregation over time and under biological conditions, we first determined the extent of lipid coverage through measurements of NP zeta potential. A hybrid NP completely covered by lipid and lipid-PEG-COOH had a zeta potential in PBS of approximately -20 mV while a NP without lipid and only PLGA-OCH₃ had a zeta potential of -8 mV (Figure 2b). Therefore, by decreasing the amount of lipid with respect to PLGA while keeping other conditions consistent, one may expect to see an increase in zeta potential as the NP goes from complete lipid coverage to no coverage. Variation of the amount of lipid to PLGA from 1:10 to 1:100 lead to an increase in zeta potential without a significant change in size (Figure 2b) which suggests that complete lipid surface coverage is not required to maintain NP size stability at 40 nm in water. In fact, a lipid to polymer ratio of 1:1000 was sufficient to prevent aggregation of the NPs. When lipid was absent, the size of the polymeric NP increased to that of PLGA NPs, similar to the trend observed in Figure 2a. The size increase in the case of 1:1 lipid to PLGA indicates that there is enough lipid to completely cover all PLGA NPs, and the excess lipid present results in an increase in the average NP size either by addition of layers, or by the formation of liposomes.

To confirm this hypothesis, we obtained the size distributions by volume of NPs in water as the amount of lipid introduced in the input stream was decreased. In addition, since PLGA NPs covered by lipid are stable in PBS as opposed to those without lipid coverage, we obtained the size distribution of the NPs in PBS as way to assay their

stability (Figure 2c). Our studies indicate that two populations of particles are formed at a lipid to PLGA ratio of 1:1 with sizes at 40 nm and 250 nm. The smaller particles correspond to hybrid NPs with full lipid coverage while the larger particles correspond to liposomes similar to ones observed in Figure 2a. For a lipid to PLGA ratio of 1:10, a homogenous size distribution was observed in water and PBS. It must be noted that a small shift of the average NP size peak is observed when the samples were measured in water versus PBS. This peak shift could be explained by an aggregation of 2 or 3 NPs after immersion in PBS and it can be controlled by tuning the ratio of lipid to lipid-PEG in the formulation (Figure S3, supporting information). For lipid to PLGA ratio of 1:100 and 1:1000, there is enough lipid present to keep the NP at size of 40 nm in water, yet it is not enough to avoid NPs aggregation in PBS. Our studies suggest that the optimal lipid coverage is obtained at a lipid to PLGA ratio of approximately 1:10. In fact, NPs prepared at this ratio were stable for a period of 24 hours in 10% BSA and 10% serum, which are surrogates for *in vivo* protein adsorption and biofouling (Supporting Information, Figure S2).³ Considering the thickness and hydrodynamic radius of a lecithin layer with DSPE-PEG, estimation of the amount of lecithin and DSPE-PEG needed to completely cover NP core of 40 nm lead to a calculated ratio of 1.4:10 of lipid to PLGA. Although this calculation relies on several assumptions (*e.g.* all NPs are spheres and monodisperse, constant ratio of lecithin to DSPE-PEG, full lipid coverage on surface etc), it still offers an adequate approximation of the amount of lipid necessary to form a stable hybrid lipid-polymeric NP.

At the same lipid to PLGA ratio, we found that there was no significant difference in the size of NPs prepared at aqueous to organic flow ratios of 10:1 and 5:1 (see [figure S1](#) supporting information). Larger flow ratios (*e.g.* 20:1, aqueous to organic) resulted in pulsing of the flow due to the syringe pumps, and required higher PLGA concentrations that made the device more susceptible to fouling. On the contrary, lower flow ratios (*e.g.* 1:1, aqueous to organic) would result in an inadequate environment for NP formation since for optimal nanoprecipitation a flow ratio of aqueous to acetonitrile streams at least 3:1 is desired.⁹ Therefore, all the NPs prepared in this work were obtained at a flow ratio of 10:1 or 5:1.

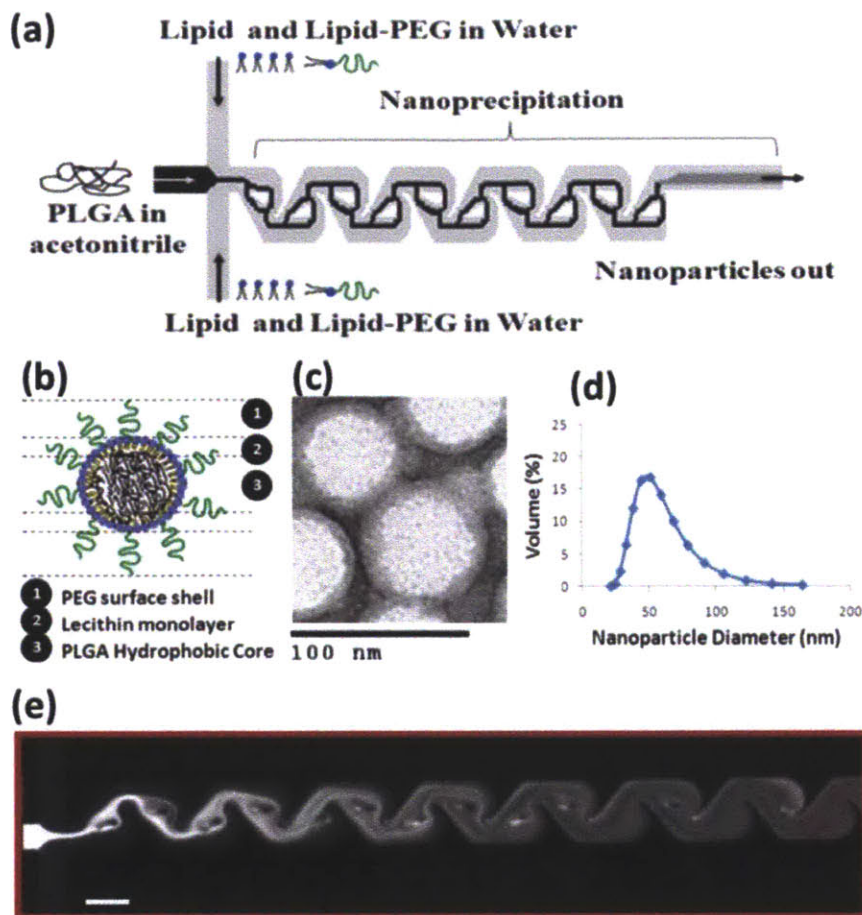


Figure A2.1 Nanoprecipitation of lipid-polymeric NPs. (a) A representative schematic of input and output streams within hybrid lipid-polymeric nanoparticle formation in microchannels with Tesla structures (b) Illustrative figure of microfluidic synthesized NP component layers (c) TEM image of uranyl acetate stained hybrid NPs after synthesis which highlights differences in density of the core versus near the surface of the NP potentially illustrating the lipid-PEG layer. Bar is labeled at 100 nm (d) Reproducible average size distribution of hybrid NPs generated through microfluidics. Average size is 40 nm. (e) Solvent mixing in the Tesla micromixing structures using fluorescent dye and water at 5 $\mu\text{L}/\text{min}$ and 50 $\mu\text{L}/\text{min}$, respectively, shows complete mixing at the fourth turn in the channel (scale bar: 100 μm).

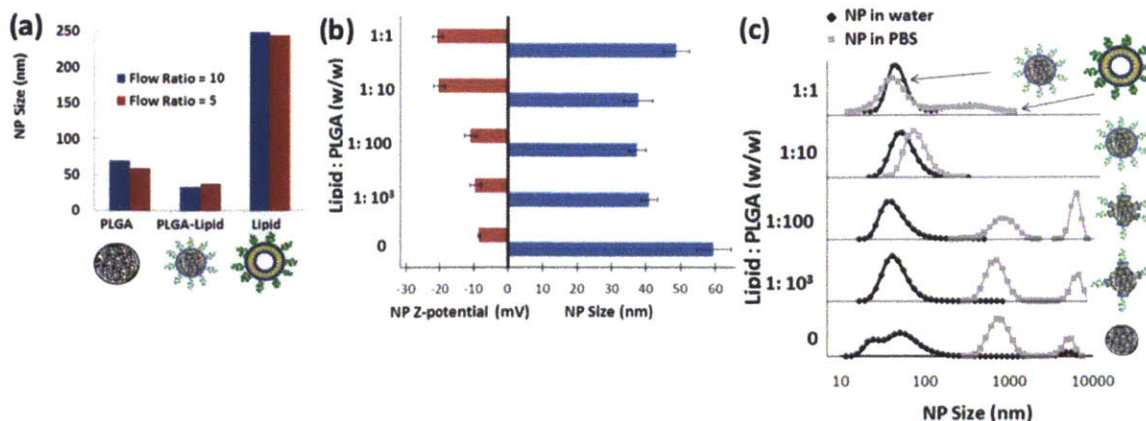


Figure A2.2. Characterization of Lipid-PLGA structure (a) Comparison of average NP size from the product stream with aqueous : organic flow ratios of 10:1 and 5:1 respectively where the input organic stream is either PLGA, PLGA and lipid, or lipid alone. (b) Determination of lipid coverage of polymeric NPs. Zeta potential and size of NPs as the ratio of lipid to PLGA (w/w) is decreased. (c) Size distributions in water and PBS of NPs as the ratio of lipid to PLGA is changed. Complete lipid coverage of polymeric cores is observed at a ratio of lipid to PLGA ratio of 1:10. Above this ratio, the remaining lipid forms other nanostructures such as liposomes and below this ratio, NPs are not stable in PBS due to inadequate lipid coverage.

Control of NP physicochemical properties: Size and surface charge

After confirming the core-shell structure of the lipid-PLGA NPs, and knowing their range of optimal lipid coverage, we investigated the possibility of controlling the NP's physicochemical properties, mainly size and surface charge. Figure 3a illustrates a change in zeta potential of the lipid-polymeric NPs when different end-functional groups of DSPE-PEG were introduced in the input streams. The zeta potential of the NPs could be controlled from positive to neutral to negative charge by utilizing -COOH, -CH₃ and -NH₂ respectively, while the size remained essentially unchanged. Specific values for zeta potentials of different modified end groups agree with those previously published.²³ These results not only show that the surface charge of the NP can be finely tuned but they also confirm that lipid-PEG is on the surface of the polymeric core. Finally, NP size was controlled by varying the inherent viscosity of the polymer and the PLGA concentration while keeping other conditions such as organic and aqueous flow rates and flow ratio the same. Decrease in inherent viscosity and increase in initial polymer concentration lead to the generation of larger NPs as reported similarly in bulk synthesis of these particles (Figure 3b)⁴. This illustrates that hybrid NPs made from microfluidics are similar in nature to those made in bulk and their physicochemical properties such as size and charge can be controlled.

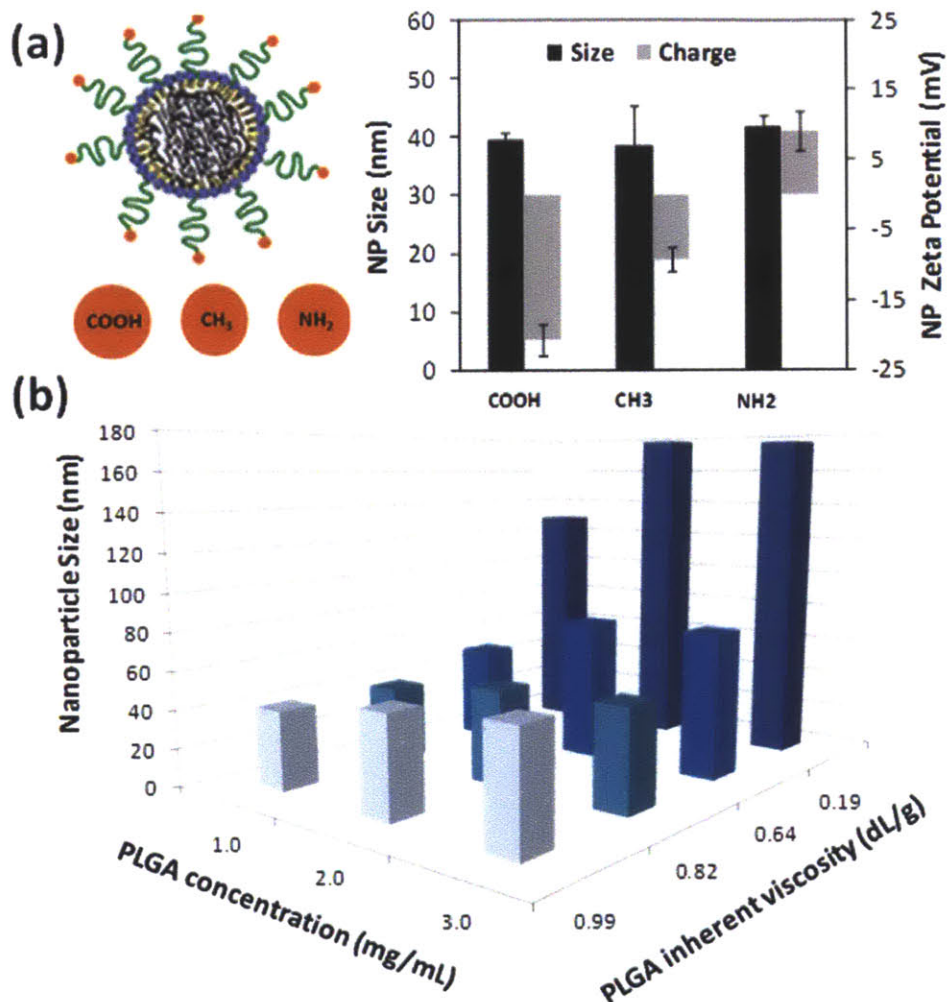


Figure A2.3 Control of NP's physicochemical properties. (a) Control of surface charge and lipid coverage of the hybrid NPs is elucidated by changes in zeta potential of the NPs in PBS using DSPE-PEG with modified functional groups of carboxyl, methyl, and amine (b) Control of NP size by varying PLGA viscosity and concentration in the organic stream. Flow ratios of aqueous to organic streams and rate were kept constant at 10 : 1 at a total flow rate of 55 μ L/min.

Investigating the role of rapid mixing and mechanism of self-assembly of the hybrid NPs

To gain more insight into the role of rapid mixing in self-assembly of the NPs, we compared the formation of NPs under rapid mixing conditions versus slow mixing conditions obtained by pipetting the same volume of polymer solution used in the microfluidic device into a lipid solution without sonication or heating. Figure 4 shows the size distributions in water and in PBS of NPs prepared under rapid mixing with the microfluidic chip and slow mixing conditions. Under slow mixing conditions at a 1:1 ratio of lipid to PLGA, the formation of liposomes is noted by the peak around 400 nm. A peak around 10 μ m in PBS, characteristic of aggregates of polymeric NPs, indicates the formation of polymeric NPs. Finally some hybrid lipid-polymeric NPs are formed since

there is a stable peak around 100 nm in water and PBS. The hybrid NPs formed under slow mixing are not homogenous, noted from the irregularity in the peak around 100 nm. This observation suggests uneven distribution of lipid-PEG among the polymeric NPs since lipid-PEG confers stability to the hybrid NPs through formation of the PEG corona (Figure S3, supporting information). Formation of polymeric NPs, lipid-polymeric NPs and liposomes, was also observed for a lipid to a PLGA ratio of 1:10. However, the larger peaks in water and PBS around 100–1000 nm are not as prominent as for the 1:1 case since the percentage by volume of polymeric NPs formed is much higher than that of liposomes. Under rapid mixing within the microfluidic channel, homogenous and stable hybrid NPs and liposomes are obtained at a lipid to polymer ratio of 1:1 and only stable homogenous hybrid NPs are obtained at a lipid to polymer ratio of 1:10, as inferred by the absence of larger aggregates upon addition of PBS. A size distribution by intensity is shown in the [supporting information](#) where the formation of distinct populations of NPs is clearly evident in the case of slow mixing of lipid and PLGA solutions, but only a single population is seen in the case of rapid mixing of lipid and PLGA solutions (Figure S4, supporting information).

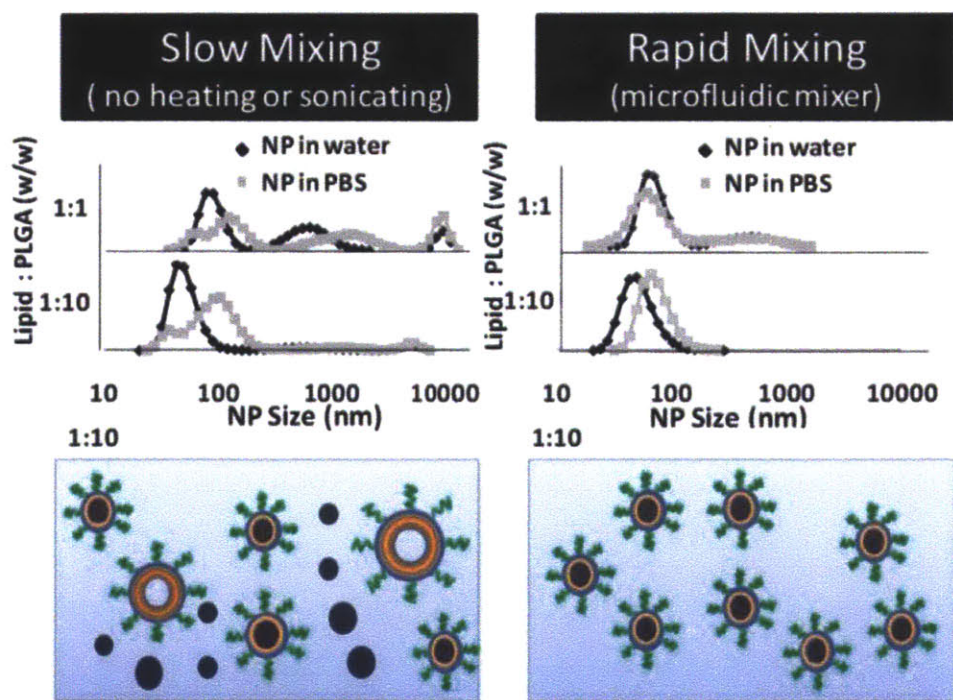


Figure A2.4. Slow versus rapid mixing. Comparison of NP size distribution in water and PBS for rapid and slow mixing of lipid and PLGA solutions with lipid : PLGA ratios of 1:1 and 1:10. Under slow mixing conditions without the input of any form of energy, aggregation upon addition of PBS indicates the presence of heterogeneous NPs (*i.e.* polymeric, lipid, and lipid-polymeric). Under rapid mixing conditions, absence of aggregation upon addition of PBS indicates that only homogenous hybrid lipid-polymeric NPs are formed, except for the 1:1 ratio that results in homogeneous hybrid NPs and liposomes.

These results give some insight into the role of rapid mixing in the self-assembly of

hybrid lipid NPs. Under rapid mixing, there is uniform lipid and lipid-PEG coverage around polymeric cores resulting in the formation of homogenous hybrid lipid-polymeric NPs. In contrast, under slow mixing, some lipid and lipid-PEG is deposited onto polymeric NPs while the rest forms lipid structures leaving polymeric NPs with uneven or no coverage. The result is the formation of a combination of liposomes, polymeric NPs, and hybrid-lipid NPs (Figure S4, supporting information). An input of energy to the system in the form of sonication and/or raise in the temperature as provided in the bulk methods of synthesis may assist in the disassembly of lipid structures and their reassembly around the polymeric cores forming homogenous lipid-polymeric NPs. Integration of rapid mixing using microfluidics bypasses the intermediate steps needed in slow mixing conditions in the preparation of homogenous lipid-polymeric NPs.

While the above experiment suggests that rapid mixing plays an important role in ensuring uniform lipid coverage on the NPs, it does not explain the invariance of NP size with lipid concentration. Interestingly, even a 1:1000 lipid : PLGA ratio was sufficient to maintain the hybrid NP at a size of 40 nm as opposed to NPs made with only PLGA, which increased in size over a period of few hours. In addition, subsequent increase of the lipid : PLGA ratio by three orders of magnitude did not affect the hybrid NP size (although some liposomes were formed in the 1:1 case). To investigate the role of lipid in self-assembly of the NPs, we designed experiments to elucidate to what extent the self-assembly of PLGA was affected by the presence of the lipid component.

In these experiments, we prepared lipid-PLGA NPs using a 'two-stage' manner, where a PLGA polymeric core of a specific size was formed first followed by deposition of the lipid onto PLGA core by flowing the solutions through the microfluidic device for a second time. We then compared the size and size distributions of these NPs with those prepared using the conventional one-step method. First, a PLGA solution in acetonitrile and water were injected into the device. These unprotected PLGA NPs (NP1) were washed and suspended in water at a concentration of 1 mg/mL. Next, NP1 particles in water were immediately reintroduced into the center inlet of the channel and the lipid solutions were introduced through the side channels. The size and size distribution of the lipid-covered NPs (NP2) obtained at the outlet were measured. NP2 particles were placed in PBS to test their stability in comparison to those NPs synthesized through conventional one-step microfluidic method (*i.e.* mixing PLGA solution with the lipid solution) (Figure 5). NP2 particles prepared using the two-stage manner had similar size distribution and stability properties to the hybrid NPs prepared in the conventional one-step microfluidic method. In other words, NPs made from a one-step method and NP2 particles had a uniform distribution with an average size of 40 nm and remained stable when placed in PBS.

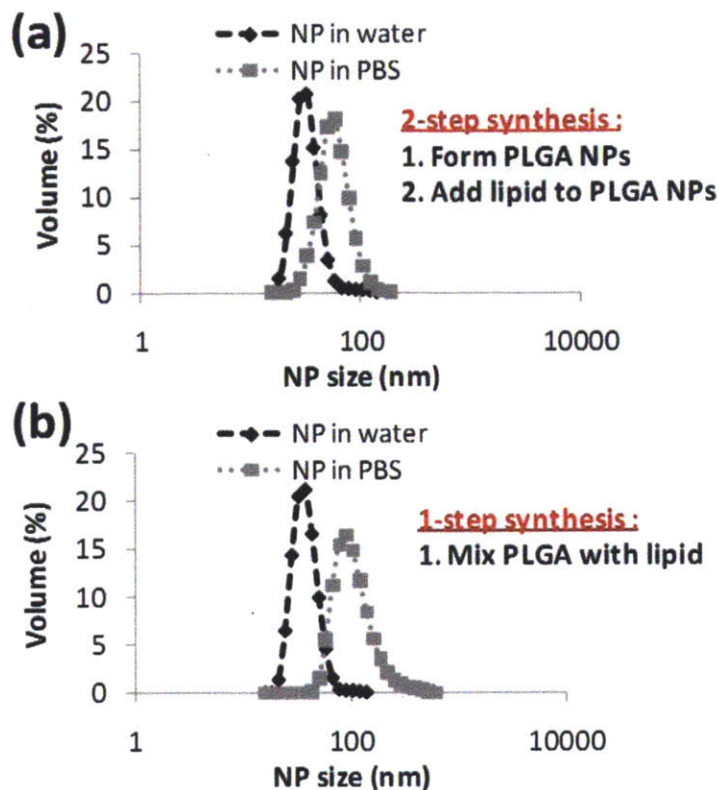


Figure A2.5 NP formation to elucidate stepwise formation of hybrid lipid-polymer NPs within microchannel (a) NP size distribution in water and PBS of particles formed in two-stage manner. PLGA NPs were prepared in the microfluidic mixer, then washed and placed as an input along with lipid aqueous stream resulting in the generation of hybrid lipid-PLGA NPs. (b) NP size distribution in water and PBS formed through the current one-step microfluidic method.

These results suggest that self-assembly of the polymeric core of lipid-PLGA NPs in the device was unaffected by the presence of the lipid component. It can be then rationalized that the one-step method indeed involves the above two distinct stages in a very small timescale. The Péclet number ($Pe = V \cdot w / D$) in this case is over 1000, which indicates that convective transport can enhance mixing of particles as long as the streams move laterally.^{24, 25} The Tesla structures in our mixing channel enforce such lateral movement of particles at their junctions. PLGA core formation, the first assembly stage, requires that PLGA chains in the focused acetonitrile stream encounter the anti-solvent, (*i.e.* water molecules), which results in conditions under which PLGA can precipitate⁹. Our microfluidic mixer ensures that complete solvent displacement of acetonitrile by water (0.2–2 ms, see [supporting information](#)) occurs on a timescale that is shorter than that of formation of PLGA cores. Furthermore, solvent displacement is almost complete before a substantial amount of lipid approaches the PLGA cores. Lipid shell formation, the second stage, then follows as soon as the lipid molecules are transported to the vicinity of already-formed PLGA cores. Although the diffusion of lipid molecules is slower than that of water molecules at least by an order of magnitude, embedded Tesla structures considerably enhance particle mixing due to their convective effects. Such laterally-

dispersive transport (combination of diffusion and convection) occurs on a mixing timescale of ~ 10 ms (see [supporting information](#)). It is worth noting that the minimal lipid coverage required to stabilize the NPs in water occurs at a lipid : PLGA ratio of 1:1000 and is obtained on a sub-millisecond timescale after sufficient amount of lipid has been transported near the core. In other words, sufficient lipid coverage to prevent long-term aggregation is achieved on a sub-millisecond timescale after complete mixing of solvent and anti-solvent. Thus, the formation of the lipid shell is a transport-limited process since the timescale of coverage is limited by the timescale of mixing. In cases of ratios of lipid : PLGA higher than 1:1000, partial mixing of lipid molecules with acetonitrile would be sufficient for minimum lipid coverage of the PLGA cores. The lipid shell forms on the timescale of 1 ms in the case of 1:1 ratio of lipid : PLGA. Therefore, the timescales for self-assembly of the PLGA cores is on the same order of magnitude as the timescale for minimum lipid coverage, at least for high lipid : PLGA ratios (see [supporting information](#)). In contrast to this minimum coverage, complete coverage of the NP with lipid requires complete mixing, which occurs on the timescales of >10 ms. The fact that hybrid NPs could be prepared in two steps (*i.e.* by first forming PLGA NPs followed by mixing with lipid) indicates that the size of the NPs formed in the device is independent of the presence of the lipid component on short timescales, and the differences in size of PLGA versus hybrid lipid-PLGA NPs shown in Figure 2a occur over a longer timescale before measurement of the NP size. Therefore, these results, along with the invariance of NP size with lipid ratio, show that the lipid component does not play a significant role in the self-assembly of the polymeric NPs but rather it stabilizes the NPs and prevents their aggregation on longer timescales. These results are further supported by measuring the size and size distribution of PLGA NPs immediately upon synthesis, which are in a similar range to hybrid NPs ([Figure S2 and S4](#), [supporting information](#)).

Preparation of lipid-QD NPs

To demonstrate the versatility of our platform design, we examined the ability of rapid mixing to synthesize hybrid quantum dot (QD) lipid NPs for imaging applications. QDs are semiconducting nanocrystals that possess excellent optical properties that make them suitable to be used as imaging probes.²⁶ However, the hydrophobicity and poor colloidal stability at physiological conditions frequently renders them inappropriate for clinical use.²⁷ In the same fashion as for hybrid lipid-polymeric NPs, it has been proposed and shown that lipid-coated QD provide enhanced NP hydrophilicity, stability in plasma, and an overall improvement of in their biocompatibility.^{28, 29} Others have encapsulated other type of particles such as magnetic NPs³⁰ and gold NPs³¹ inside a lipid and polymeric envelope, respectively.

As a proof of concept to show that a similar microfluidic platform can be used to prepare other NPs, we prepared hybrid NPs composed of QDs encapsulated by lecithin and DSPE-PEG layer (Figure 6a). Lipophilic QDs were dissolved in THF (0.5 mg/mL) and introduced in the middle input stream in place of the polymeric stream from the prior study. The lipid-QD NPs in the product stream showed a homogenous size distribution with an average size of 60 nm and did not need further processing for *in vitro* and/or *in vivo* experiments except for the removal of a small fraction of THF through filtration or

evaporation (Figure 6b). At an initial concentration of 0.5 mg/mL, TEM images show an average of four quantum dots encapsulated per NP (Figure 6c). The number of QDs could be controlled by varying the lipid to QD ratio. To ensure that the images obtained from TEM are QDs encapsulated on lipid NPs and not QDs adhered to the surface of a lipid matrix, images were taken of the operating channels to study their formation. It was observed that before encapsulation of QDs, some aggregation of QDs was visible inside the channel and after encapsulation, the channel remained free of QD aggregates (Figure S6, supporting information). These results clearly show that one can use the same microfluidic platform to synthesize distinct types of hybrid NPs. The results suggest that by using this continuous-flow microfluidic technology one can entrap other imaging agents such as gold NPs and/or magnetic NPs inside a lipid or polymeric envelope to form multifunctional particles for use of various imaging modalities. Through selection of appropriate solvents and concentration, therapeutic and imaging agents can be introduced into the input stream to form a theranostic system.

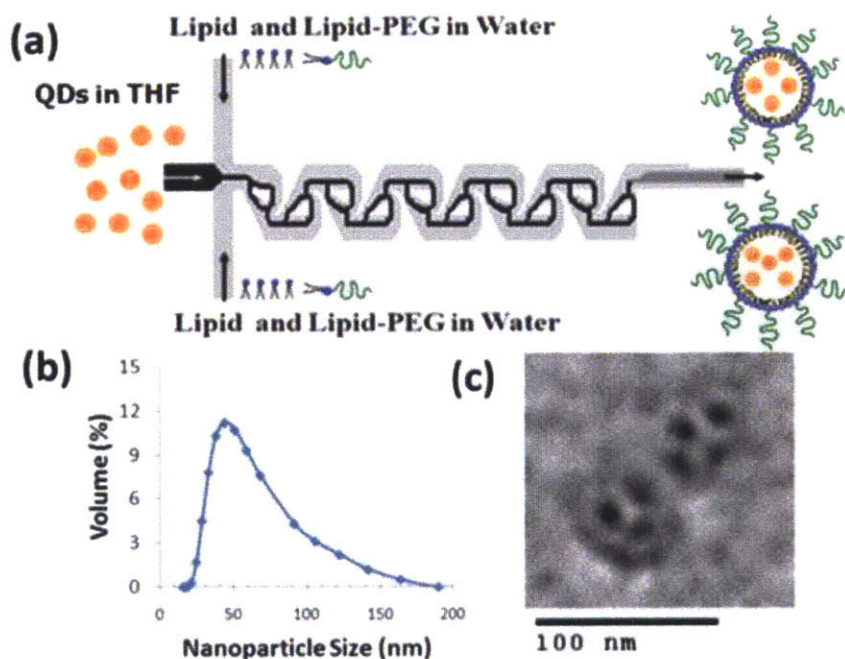


Figure A2.6. Preparation of hybrid lipid-QD NPs. (a) Schematic of liposome formation in the Tesla mixer with quantum dots encapsulated within the core (b) NP distribution of quantum dot encapsulated liposomes formed through the Tesla mixer (c) TEM image of hybrid lipid-QD NPs stained with 1% phosphotungstic acid aqueous solution showing monodisperse particles with a Z-average size of 60nm. Bar is labeled at 100 nm.

In conclusion, we demonstrated that hybrid lipid-PLGA NPs can be prepared by rapid mixing of a polymeric solution with a lipid solution in a microfluidic device. We identified an optimal ratio of lipid : PLGA that resulted in stable and homogeneous NPs. The size and charge of the NPs could be controlled by using PLGA of different viscosities (molecular weights) and by using lipid molecules with different end groups, respectively. The experiments suggest that the self-assembly of PLGA core occurs

independent of the lipid component, but the lipid component provides stability to the NP against aggregation over time and in the presence of high salt concentrations. Furthermore, rapid mixing ensures formation of homogeneous NPs; in contrast, slow mixing results in different populations of NPs that are not uniform in composition and size. We also demonstrated that hybrid lipid-QD NPs could be formed in the same system. Reproducible manufacture of monodisperse, stable NPs with the ability to control properties by varying concentrations of different precursors in a simple mixing step could greatly facilitate combinatorial synthesis and prove to be useful in the emerging field of nanomedicine.

Experimental Methods

Device fabrication and experimental setup

Microfluidic devices were fabricated with poly(dimethylsiloxane) (PDMS) using a standard micromolding process. PDMS (Sylgard 184, Dow Corning) monomer and curing agent were mixed in a ratio of 10:1 by weight, pored over the silicon wafer mold, and degassed. After curing, PDMS was peeled off and inlet/outlet holes were drilled using a 300 μm diameter drill bit. The PDMS component was then bonded to a 1" \times 2" glass slide using air plasma. The resulting device had one inlet each for water and solvent streams, and one outlet. The water stream was split into two in order to achieve two water streams at the flow focusing junction. The mixing channel was 50 μm wide, 60 μm high and 2.5 mm long. One 500 μL syringe was mounted on a syringe pump (SP230IW, World Precision Instruments) while the other syringe was mounted on another syringe pump (PHD 22/2000, Harvard Apparatus) to control flow through the device. Water flow rate was maintained at 50 $\mu\text{L}/\text{min}$, while the solvent flow rate was varied from 5 $\mu\text{L}/\text{min}$ to 10 $\mu\text{L}/\text{min}$.

Preparation of PLGA-lecithin-PEG NPs

A solution of PLGA (intrinsic viscosity 0.82 dL/g; Lactel, Pelham, AL) was dissolved in acetonitrile (1 mg/mL) and lipid solution composed of 4% ethanol aqueous solution of lecithin (soybean, refined, molecular weight: \sim 330 Da; Alfa Aesar, Ward Hill, MA) and DSPE-PEG (molecular weight: \sim 2850 Da; Avanti Polar Lipids, Alabaster, AL) (lecithin/DPSE PEG, 8.4/1.6) were prepared independently for separate inlets and mixed within the chip at fixed flow rates using syringe pumps. Lipid solution flow rate was fixed at 50 $\mu\text{L}/\text{min}$ while polymer solution flow rate was set at 10 $\mu\text{L}/\text{min}$ for some experiments and 5 $\mu\text{L}/\text{min}$ for others. Lipid concentration was varied from 102 to 0.1 $\mu\text{g}/\text{mL}$ at a constant flow rate of 50 $\mu\text{L}/\text{min}$. To prepare NPs at slow mixing conditions, 100 μL of the lipid solution described in the previous paragraph was mixed with 10 μL of PLGA solution in acetonitrile using pipette tips. For the NP stability studies, 20 μL of 10x PBS were added to 60 μL of the NP solution. Size and zeta potential of NPs were immediately measured upon addition of PBS. For hybrid lipid-PLGA NPs prepared with the microchannel, up to four consecutive additions of 20 μL of 10x PBS were pipetted to 60 μL of the sample and its size was monitored for each addition. No change in size was observed after the first addition of the buffer.

Preparation of QD-lecithin-PEG NPs

A solution of lipophilic quantum dots (TOP-coated CdSe/ZnS QDs, Invitrogen, CA, USA) was dissolved in tetrahydrofuran (THF) (0.5 mg/mL) and a lipid solution of 4% ethanol aqueous solution of lecithin and DSPE-PEG (lecithin/DPSE PEG, 8.4/1.6) at a concentration of 0.02 mg/mL were prepared independently for separate inlets and mixed within the chip. Lipid solution flow rate was set at 50 $\mu\text{L}/\text{min}$ while QD solution flow rate was set at 5 $\mu\text{L}/\text{min}$. Both flow rates were controlled with syringe pumps.

Particle sizing and zeta potential measurements

Particle sizing was performed using dynamic light scattering with Zetasizer Nano ZS (Malvern Instruments Ltd., U.K.). For each measurement, 100 μL or more volume of the sample was loaded in a disposable low-volume cuvette. Three measurements were performed on each sample. We observed that the presence of acetonitrile changed the NP size by less than 3 % when water-acetonitrile mixtures containing up to 5 % acetonitrile were further diluted in water. All measurements were performed at acetonitrile concentrations of less than 10 % acetonitrile to ensure that any observed variation in particle size was not due to the solvent. The NP surface zeta potential was measured by using ZetaPALS (Brookhaven Instrument., U.S.A). For each measurement, particles were washed with water three times and reconstituted in 1mL of PBS (0.5mg/mL). The zeta potential was recorded as the average of three measurements.

Transmission electron microscopy (TEM)

Lipid-polymeric NPs

TEM experiments were carried out on a JEOL JEM-200CX instrument at an acceleration voltage of 200 kV. The TEM sample was prepared by depositing 10 μL of the NP suspension (1.0 mg/mL) onto a 200-mesh carbon-coated copper grid. Samples were blotted away after 30 min incubation and grids were negatively stained for 20 min at room temperature with freshly prepared and sterile-filtered 2% (w/v) uranyl acetate aqueous solution. The grids were then washed twice with distilled water and air dried prior to imaging.

Lipid-QD NPs

TEM experiments were carried out on a JEOL JEM-2011 instrument at an acceleration voltage of 200 kV. The TEM sample was prepared by depositing 10 μL of the NP suspension (1.0 mg/mL) onto a 300-mesh formvar-coated copper grid. Samples were blotted away after 30 min incubation and grids were negatively stained for 20 min at room temperature with sterile-filtered 1% (w/v) phosphotungstic acid aqueous solution. The grids were then washed twice with distilled water and air dried prior to imaging.